ATOM PROBE TOMOGRAPHY FOR MODELLING EIGENSTATES IN A QUANTUM DOT ENSEMBLE

ATOM PROBE TOMOGRAPHY FOR MODELLING EIGENSTATES IN A QUANTUM DOT ENSEMBLE

BY

CHRISTOPHER NATALE

B.A.Sc. in Engineering Science

A Thesis Submitted to the Department of Engineering Physics and

School of Graduate Studies in Partial Fulfillment of the Requirements

for the Degree Master of Applied Science

Master of Applied Science (2023)

McMaster University

Department of Engineering Physics

Hamilton, Ontario, Canada

TITLE:	ATOM PROBE TOMOGRAPHY FOR MODELLING EIGENSTATES IN A QUANTUM DOT ENSEMBLE
AUTHOR:	Christopher Natale B.A.Sc. in Engineering Science (University of Toronto)
SUPERVISOR:	Dr. Ryan Lewis
NUMBER OF PAGES:	x, 149

Abstract

Epitaxially grown quantum dots (QDs) make up a significant portion of nanoscale semiconductor research, yet precise solutions for their eigenstates in complex geometries are often unknown. Eigenstates are extremely relevant as they impact the emission wavelength, performance, and stability of many optoelectronic devices. In this thesis, atomic force microscopy, transmission electron microscopy, and atom probe tomography (APT) are used to assess and compare QD size and core concentration. APT by means of isosurface reconstruction provides the most accurate ensemble averaged quantum dot size and core concentration. High-angle annular dark-field imaging quantifies core concentration very well, but fails in comparison to precisely quantify QD size. Ensemble averaging is discarded in favour of using the raw APT data to devise a model that can solve the Schrödinger equation in 3-dimensional space and can be expanded upon to include non-trivial quantum dot geometries of any kind. The electron and hole eigenstates for an entire quantum dot ensemble are solved using this model. Hybridized eigenstates between neighbouring quantum dots are realized and found to experience both bonding and anti-bonding of the charge carriers. The existence of a degenerate state is also discovered. The simulated eigenenergies are compared to the photoluminescence emission spectrum and found to accurately represent the exciton recombination energy. This makes it possible to obtain very realistic 3-D eigenstate representations for a variety of complex structures. The modelling technique outlined in this thesis is not constrained to just QDs, but can also be applied to an array of many other nanoscale structures.

Acknowledgements

I'd like to begin by acknowledging my supervisor, Dr. Ryan Lewis, as he always encourages me to put my best work forward. I am very grateful to have had the opportunity to work with him during my time at McMaster. With his encouragement and guidance, I have truly enjoyed performing incredible research in his group. My fellow group members have also been monumental toward making research and school very enjoyable, and I am happy that I have had the opportunity to work alongside them.

I'd also like to thank my interim supervisor, Dr. Ray LaPierre, as he provided me with very helpful counsel as I was planning the growth used in this thesis, and Dr. Kitai for his course in nanoscale semiconductor devices, as it was the first class I took at McMaster several years ago, and one that I have very fond memories of. Finally, I'd like to thank all the members of the committee for their time to read through this thesis.

Contents

List of Figures

Chapter 1 Introduction

1.1 Laser Diode Overview

Within the resonant cavity of a laser, photons can interact with electrons in the conduction band or valence band of the material that composes the gain medium. Electrons in the valence band that absorb a photon will be excited to a state in the conduction band. As the electron vibrationally relaxes, it will exist in a state given by the Fermi-Dirac distribution. The excited electron could form a superposition state with the valence band hole, generating an oscillating dipole that creates an electromagnetic wave in the form of a photon. The direction and phase of the photon is random. This is known as spontaneous emission, though it takes a finite amount of time for this radiative process to occur. During this time, the excited electron could also interact with an incident photon. As the electron returns to the valence band, it releases a photon that is of the same direction and phase as the incident photon. This process is known as stimulated emission and allows for coherent waves to constructively interfere with one another. Many non-radiative processes can also occur while the electron is in the conduction band, such as phonon generation and Auger recombination.

In an inverted system, the rate of stimulated emission exceeds the rate of absorption. This indicates the point at which it is more likely that a photon interacts with an electron in the conduction band than one in the valence band. An input of energy is

pumped into the system so that population inversion of the carriers can be maintained while the laser is operating. The magnitude of the electric current to achieve population inversion is termed the threshold current. This dictates the performance efficiency of the laser as lower threshold currents require less input power to the system.

Semiconductor laser diodes were first developed in 1962.[1] The original design consisted of simple GaAs p-n homojunctions which required very low temperatures and high pump currents to reach population inversion.[1] The advent of the double heterostructure greatly reduced the threshold current density by sandwiching the active region with a smaller bandgap between a larger bandgap material.[1,2] This constrains the charge carriers to the active region by providing a barrier so that excitons cannot dissociate. This technique is still commonly in use today through the insertion of cladding layers which encapsulate the active region of the device.

Group III/V compounds are commonly used for the active region due to their direct bandgap properties. The local energy minimum of the conduction band and local energy maximum of the valence band are located at the centre of the Brillouin zone in the momentum space basis. In an indirect bandgap material, some energy must be transferred to the crystal lattice to generate phonons which would assist in providing momentum to the carriers. The momentum transfer allows for carrier transition between bands, but the necessity of phonons reduces the rate of radiative recombination. Direct bandgap materials are not affected by this limitation, making them the more ideal choice for laser diodes.

1.2 Quantum Dot Lasers

Carrier confinement through the use of quantum wells, and later quantum dots, aided in reducing the threshold current density much further. By the year 2000, the threshold current density for a quantum dot laser was down to $j_{th} \approx 19\ A/cm^2$ from $j_{th} \approx 10^5\ A/cm^2$ since the first inception of the semiconductor laser diode in 1962.[2] Quantum confinement occurs when the carriers are restricted to a region that is smaller than their de Broglie wavelength.[1,3] Confinement in all three spatial dimensions results in a density of states that is a Dirac delta function with peaks existing at distinct finite energy levels. Optical transitions occur between discrete states that have been Lorentzian broadened by polarization effects.[1,4] The large separation between energetic states reduces the thermal distribution of charge carriers, leading to more temperature insensitive characteristics than in bulk or quantum well structures.[5] Energetic states are spaced closer together toward the band edges and become spaced further apart for higher energies.[6]

Quantum dot lasers have become popular in the telecommunications industry due to their use alongside silica optical fibre. A wavelength of 1.3 μm is the lowest signal dispersion in silica fibre,[1] whereas the 1.55 μm regime will have the lowest signal attenuation.[7] The output signal must propagate through the optical fibres, thereby making these wavelengths a desirable choice for lasing. Quantum dots are highly tuneable in this regard as their emission wavelengths are based on their size and material composition. The discovery of the Stranski-Krastanow (SK) growth mode allowed for the high density formation of self-similar quantum dots that could contribute to the lasing regime.[1] Though

they are similar, there exists some degree of inhomogeneity between their sizes, shapes, and compositions which lead to broadening of their emission wavelength.[8] This necessitates the use of frequency combs to create a distribution of equally spaced channels with peak gain centred around the wavelength of interest.[9,10]

Quantum dot lasers have low threshold currents that are insensitive to operating temperature, allowing them to provide large data rates even in ambient conditions.[11] They experience less amplified spontaneous emission, thereby reducing timing jitters due to less random fluctuations in photon density.[11] Less heat is dissipated by phonons from their improved quantum efficiencies,[11] leading to drastically longer device lifetimes than other semiconductor laser diodes.[1] Quantum dot lasers also have a very small linewidth enhancement factor and relative intensity noise, providing them with a strong tolerance for optical feedback.[5] In a coherent feedback setup, spectral analysis is used to monitor the polarization of the incident and reflected waves, improving coherence by matching the polarization of the light before it reenters the laser cavity.[12]

1.3 Dynamic Stability and Auger Recombination

Optical feedback is a form of external perturbation. The laser's capability of resuming steady state operation is dictated by the dynamic stability of the system. Increasing pump power results in nonlinear intensity oscillations (relaxation oscillations) that are dampened until equilibrium is achieved.[1] Lasers can be subdivided into classes based on how strongly they dampen these oscillations. This determines how well they will respond to forms of external perturbations such as optical feedback or injection.[1] Strong dampening is desired such that any external perturbation to the system would be immediately suppressed to reach equilibrium.

Quantum well lasers experience weak dampening toward relaxation oscillations, whereas quantum dot lasers are able to achieve greater dynamic stability.[1] The stability is dictated by the comparison between carrier and photon lifetimes within the system.[1] Quantum well lasers experience photon lifetimes that are on a much shorter timescale than carrier lifetimes.[1] Quantum dot lasers are unique in this regard as the carrier lifetimes are tuneable depending on the band structure of the active region.

Photon lifetimes are related to the geometry of the laser device.[13] A decrease in the cavity length results in a reduction of the photon lifetime,[13] whereas highly refractive mirrors prolong the photon lifetime.[1] Most traditional semiconductor lasers have a photon lifetime of ~1 ps and carrier lifetime of ~1 ns.[13] To create a dynamically stable device that experiences strong dampening of oscillations, these two lifetimes should be reversed such that the carrier lifetime is shorter than the photon lifetime.

During SK growth, an intermediate wetting layer is formed during the 2-dimensional growth regime prior to island nucleation. This surrounding matrix which encapsulates the QDs can be thought of as a well which serves as a carrier reservoir. Carriers are contained within the well due to the higher energy barriers of the cladding. The carriers are fed into the dot energy levels to replenish those that have been depleted through emission. Nonlocal Auger recombination is the dominant carrier exchange process between the well reservoir and the quantum dots.[1] Carriers are scattered into discrete energy states of the quantum dots, but could also escape to the surrounding reservoir. The Auger in-and-out scattering rates are highly important for determining the carrier lifetimes as they are inversely proportional to one another.[1] Shorter carrier lifetimes would correspond to a greater exchange between the reservoir and dots.

The carrier density in the reservoir can be controlled by manipulating the pump current.[1] Higher carrier density would be achieved by increasing the current as more carriers are injected into the reservoir. This would increase the scatter rates between the reservoir and dots, thereby decreasing carrier lifetimes. The scatter ratio for electrons and holes can be expressed as[1]

$$\frac{S_e^{out}(w_e, w_h)}{S_e^{in}(w_e, w_h)} = \frac{e^{-\frac{\Delta E_e}{kT}}}{e^{\frac{w_e \pi \hbar^2}{m_e^* kT}} - 1} \tag{1.1}$$

$$\frac{S_h^{out}(w_e, w_h)}{S_h^{in}(w_e, w_h)} = \frac{e^{-\frac{\Delta E_h}{kT}}}{e^{\frac{w_h \pi \hbar^2}{m_h^* kT}} - 1} \tag{1.2}$$

These are derived based on a system of five non-linear, coupled, differential rate equations for the number of photons within the laser cavity, the carrier occupational probabilities, and the reservoir carrier density.[1] The Auger in-and-out scatter rates for the carriers are $S_{e/h}^{in}$ and $S_{e/h}^{out}$ respectively. $S_{e/h}^{out}$ represents the rate at which carriers are escaping to the reservoir and $S_{e/h}^{in}$ corresponds to the rate at which carriers are being scattered into discrete energy states within the quantum dots. The carrier density per unit area in the reservoir is represented by $w_{e/h}$, and $\Delta E_{e/h}$ is the energy difference between the reservoir band edges and the carrier eigenstates within the quantum dot.

The damping strength is dominated by the slower carrier (longer lifetime).[1] Generally, $\tau_e > \tau_h$ due to electrons having deeper eigenstates than holes with respect to the reservoir band edges.[1] The carrier lifetimes are[1]

$$\tau_e = \left(S_e^{in} + S_e^{out}\right)^{-1} \tag{1.3}$$

$$\tau_h = \left(S_h^{in} + S_h^{out}\right)^{-1} \tag{1.4}$$

The ratio $\frac{S_{e/h}^{out}}{S_{e/h}^{in}} \to 0$ if $\Delta E_{e/h} \gg kT$ due to the exponential nature of the numerator.

Carriers are trapped inside the dot if the eigenstates are too deep and there is not enough thermal energy to help them escape to the reservoir. This would prolong the carrier lifetime as the reservoir-dot exchange becomes one sided. $S_{e/h}^{out}$ would approach zero, but $S_{e/h}^{in}$ would not increase at a proportional rate due to relaxation and recombination time, thereby causing $\tau_{e/h}$ to increase.

1.4 Significance of Energy Eigenstates

Quantum dot eigenstates are highly important as they determine both the emission wavelength and the performance of the device. Carrier dynamics introduces complexity that could be advantageously used if the correct principles are applied. Tunnelling injection quantum dot lasers are an example of this, showing either superior or inferior data rates and temperature sensitivity compared to traditional quantum dot lasers.[14] There exists a discrepancy that can be fully understood by assessing the carrier dynamics of the band structure.

In traditional quantum dot lasers, there exists nonlinearity in gain as carriers are scattered into the higher energy states of the quantum dots from the surrounding reservoir. These energy states do not contribute to lasing, and the carriers would have to vibrationally relax to the lowest energy eigenstate by Kasha's rule, provided they do not have enough thermal energy to escape the quantum dot. This would take a finite amount of time, with deeper states taking longer to reach. As the pump current is increased, the carrier density in the reservoir increases, but scatter into the quantum dot is bottlenecked by the relaxation time.

Tunnelling injection is achieved by placing a quantum well that serves as a carrier reservoir in close proximity to the quantum dot active region.[14] Separated by an energy barrier, carriers can tunnel between the well and dots forming hybridized states. The well potential is an intermediate between the surrounding barrier potential and the dot potential. Additionally, the scattering cross section of the well region is greater than the

dot region due to more spatial overlap of the wave functions between the well and barrier states.[14] This would lead to greater carrier exchange between the well and the surrounding barrier than in the case of the isolated dot. If the hybridized state is of greater energy than the isolated dot states, this would contribute to loss as there would be less confinement and the carriers would still have to vibrationally relax. Tunnelling injection can only outperform traditional quantum dot lasers if the lowest dot energy state is properly fed by the hybridized state without having to vibrationally relax.[14]

1.5 Molecular Beam Epitaxy

Molecular Beam Epitaxy (MBE) is a widely used growth technique for developing and researching semiconductor structures. Ultra-high vacuum conditions ($< 10^{-7}\ Pa$) are required for an MBE system. However, much lower pressures ($< 10^{-9}\ Pa$) are often necessary to achieve purity in the grown material.[15] This is because the number of residual gas molecules in the chamber (O_2 and N_2) may exceed $10^5\ cm^{-3}$ even at these pressures and can be incorporated into the structure.[15] The growth and loading chambers are quickly evacuated with high speed pumps to ensure residual gas concentrations are kept as low as possible. The substrate chosen for the growth is radiatively heated by placement on a holder that is electrically driven with large currents to obtain a desired temperature. The substrate temperature is monitored using a pyrometer to assess infrared light intensities emitted from the substrate. The substrate is often at a

different temperature than the holder since there are no gaseous molecules flowing over it to efficiently conduct heat as in other growth systems such as Metalorganic Vapour-Phase Epitaxy (MOVPE).[15]

Effusion cells containing solid or gas sources are also heated in a crucible so that a molecular flux of the source material is directed at the substrate. The intensity of the molecular beam can be controlled by altering the source temperature, or flow rate for gas sources, thereby affecting the rate of growth. Shutters are placed to block effusion cells and can be rapidly opened or closed to induce fine control of the growth with single atomic layer accuracy.[15] The MBE system utilized in this thesis (SVTA-MBE35) contains a gas source for the group V elements, namely As_2 and P_2 dimers.

1.6 Research Incentive

The motivation for this thesis is to create a method for which any quantum dot eigenstate can be accurately resolved for both its energy and wave function. If this process is deemed to be successful, then any complex arrangement of dot structures can be solved at will regardless of their shape, concentration, or surrounding potential. It would have the possibility to be extended to include other forms of energy that would affect the Hamiltonian, as well as other nanostructures that may not even be quantum dots. All of these aspects together make it to be highly rewarding work, as it may become very useful for future research endeavours.

Chapter 2 Growth and Characterization

2.1 Growth Procedure

The sample studied in this thesis was grown by MBE using a GaAs (001) oriented substrate. It was first thermally annealed at 650°C under As_2 flux to desorb native oxides prior to growth. The temperature was then lowered to 500°C and a V/III precursor ratio of 2 was used for the remainder of the growth. On top of the substrate, a 100 nm GaAs buffer layer was grown followed by 25 nm of InGaP cladding and another 100 nm of GaAs. Three InAs layers were then grown with 25 nm of GaAs spacing between each of them. During the growth of the InAs quantum dot layers, the Ga source was closed and a double shutter sequence (open-close-open) was used for the In source. Shutter sequencing for InAs/GaAs QDs has been demonstrated to redshift the emission wavelength by 120 nm and reduce the FWHM by ~30% through QD size modulation.[16] A total of 1.7 ML [monolayer ≈ 3.0 (3.3) Å unstrained (strained) InAs][17,18] of InAs was deposited for each of these three layers, with an equal amount of time for each open shutter period. This structure was capped with 100 nm of GaAs, 25 nm of InGaP cladding, and 100 nm of GaAs. To assess QD morphology, 1.7 ML of InAs was deposited on the surface using the same growth technique as the buried layers. The growth was terminated by closing the precursors and the sample was cooled to room temperature. All GaAs and InGaP regions were grown at 0.2 nm/s, whereas all InAs regions were grown at 0.06 nm/s.

2.2 Surface Morphology

Photonic applications of quantum dots require the nucleated clusters to be homogeneous in size such that each exciton will experience a similar degree of quantum confinement. This contributes to the sharpness of the photoluminescence (PL) spectra, as a variation in quantum dot sizes will cause broadening of the PL emission peak. Atomic force microscopy (AFM) is a valuable tool to initially quantify these size differences and assess the uniformity and density of the clusters. The clusters on the surface share many similar characteristics to those that were buried within the active region as they were grown using the same parameters. However, the capping procedure for the buried layers would induce more In-Ga intermixing than the surface QDs as they were left uncapped. The QD sizes by AFM will be contrasted to other forms of microscopy (TEM and APT) to verify if features of the surface can be extrapolated to the buried quantum dot layers.

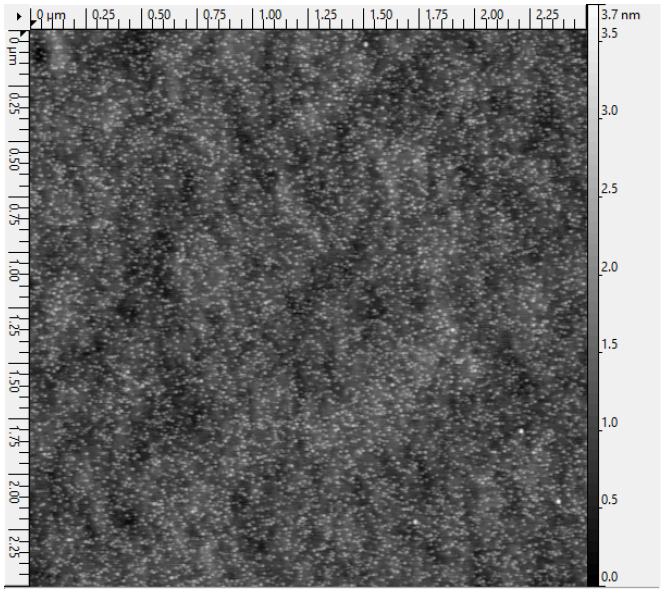

Figure 2.1 - 2.3 x 2.3 μm AFM scan

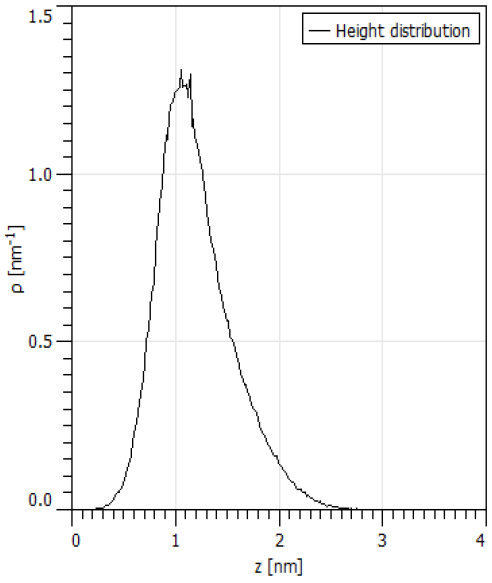

Figure 2.2 - 2.3 x 2.3 μm height density

2.3 Atomic Force Microscopy

The AFM was operated in tapping mode using a tip with a 10 nm radius. Post-processing was performed in Gwyddion software. A 2.3 x 2.3 μm scan of the surface by AFM is shown in fig. 2.1; fig 2.2 is a height density distribution for this region calculated using the corresponding pixel intensity. Fig 2.2 uses density units nm^{-1} because the statistical calculation is performed using a line scan across each pixel along the microscope's fast scanning direction. The distribution is positively skewed due to island nucleation occurring on a corrugated surface. The surface is not planar, leading to a height distribution on top of which QD nucleation may occur. Figure 2.3 demonstrates an example of a height line scan across a surface by excluding the quantum dots. The QDs have been excluded by capping the maximum evaluable greyscale intensity under the red masked region, such that the height line scan across it will be throttled by this threshold. Line scans have been taken across 50 different regions using this method, documenting the height of the upper surface.

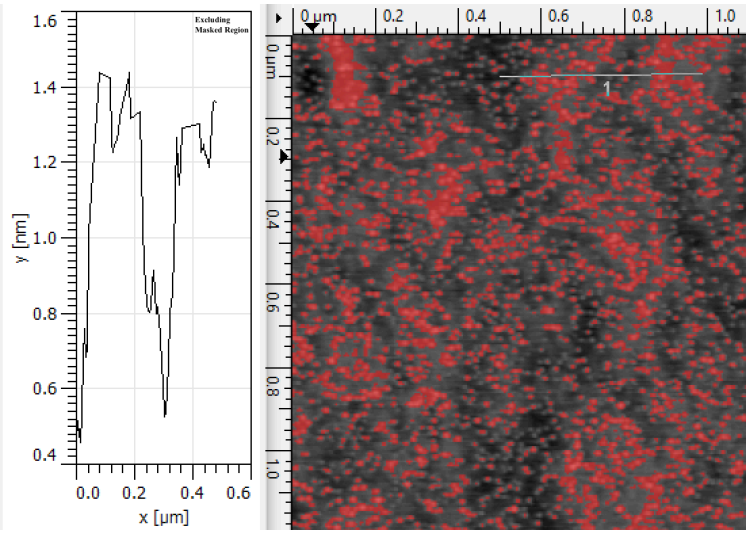

Figure 2.3 - Height line scan taken across surface (QDs excluded)

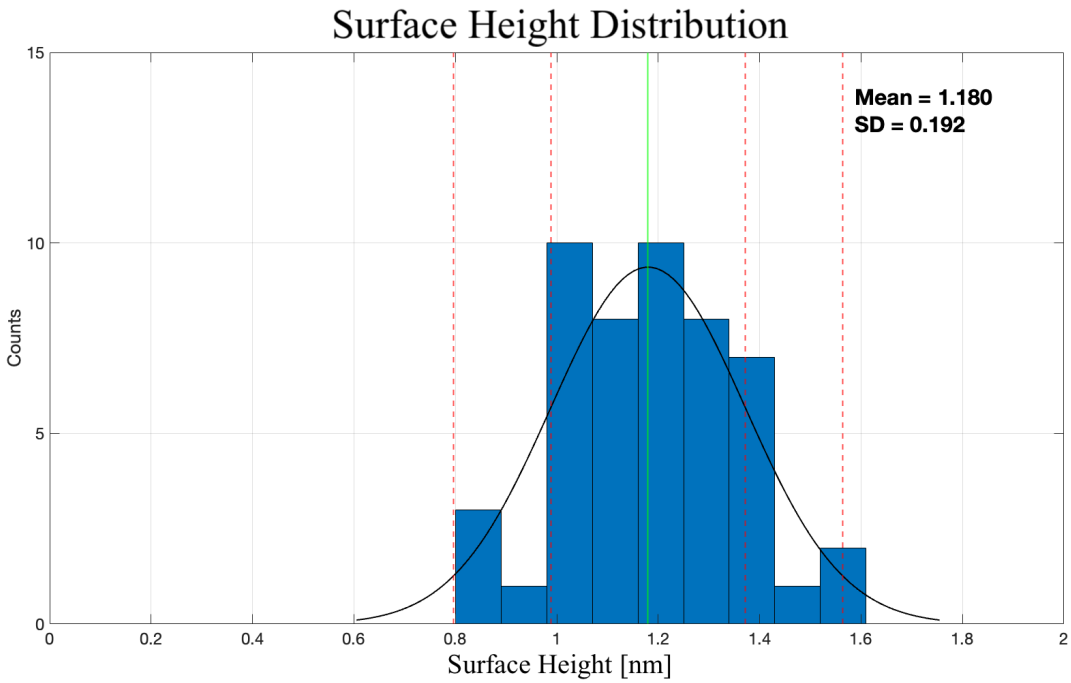

Figure 2.4 - Gaussian extracted from surface height

Fig. 2.4 shows the resulting Gaussian distribution created as a result. The surface height is with respect to the lowest point of the scan (marked zero height), and not the difference in surface height between two separate regions. Through this method, the average upper surface height excluding the quantum dots was determined.

$$h_{surface} \approx 1.2 \pm 0.4\ nm$$

As a result of surface corrugation, the height distribution depicted in fig. 2.2 cannot be used to assess the true height of the quantum dots. To accommodate for this shortcoming, a line scan taken across a single quantum dot to assess its height and width is demonstrated in fig. 2.6. The boundaries on the width are defined as the point at which the height begins to increase relative to the background, indicating that it is the edge of the quantum dot core. To assess the height, the maximum of the quantum dot is used for

the upper bound. Whereas the lower bound can experience a height offset on either side of the QD, and in this case an average is used between the two lower bound heights. Figures 2.5 and 2.6 show the process of extracting these bounds using a line scan across a QD.

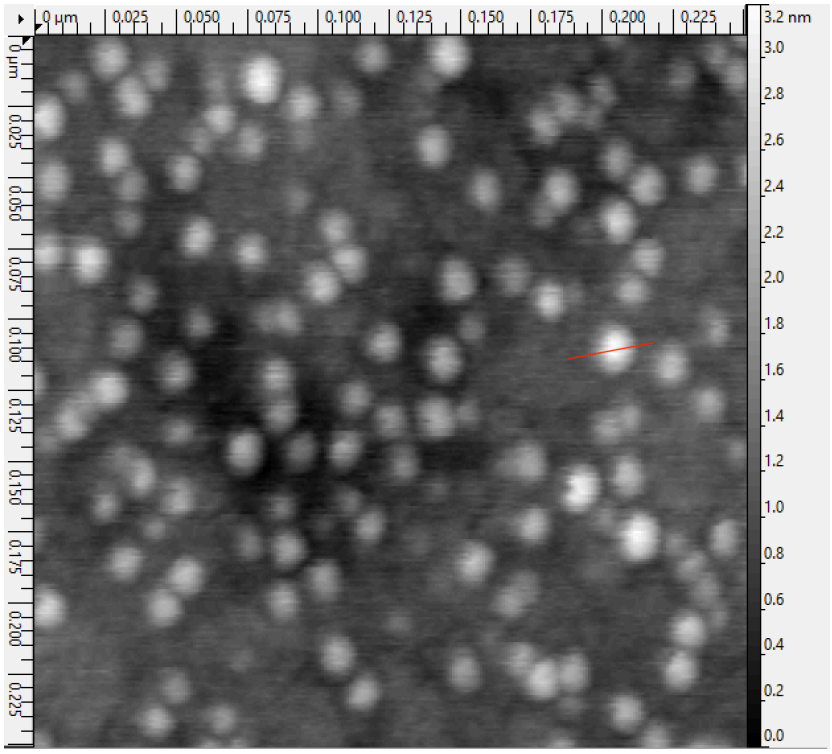

Figure 2.5 - 0.25 x 0.25 μm AFM scan

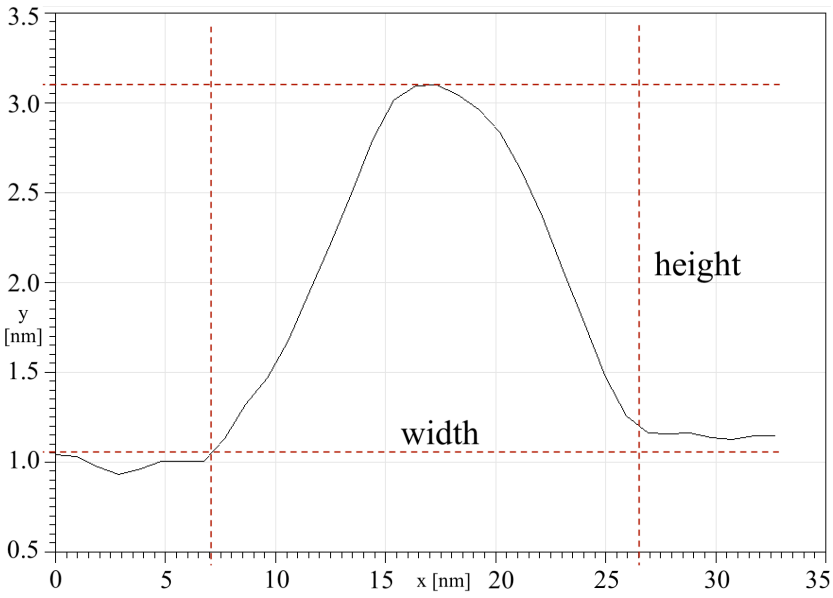

Figure 2.6 - Line scan across quantum dot shown in figure 2.5

The lateral and vertical dimensions of quantum dot ensembles are often modelled using Gaussians.[19-21] Bimodal and multimodal distributions formed by sub-ensembles have also been demonstrated in literature.[22,23] Using the method shown in fig. 2.6, line scans have been taken across 100 different quantum dots displayed in fig. 2.5. The existence of elongation along a particular axis for the lateral width has been neglected.

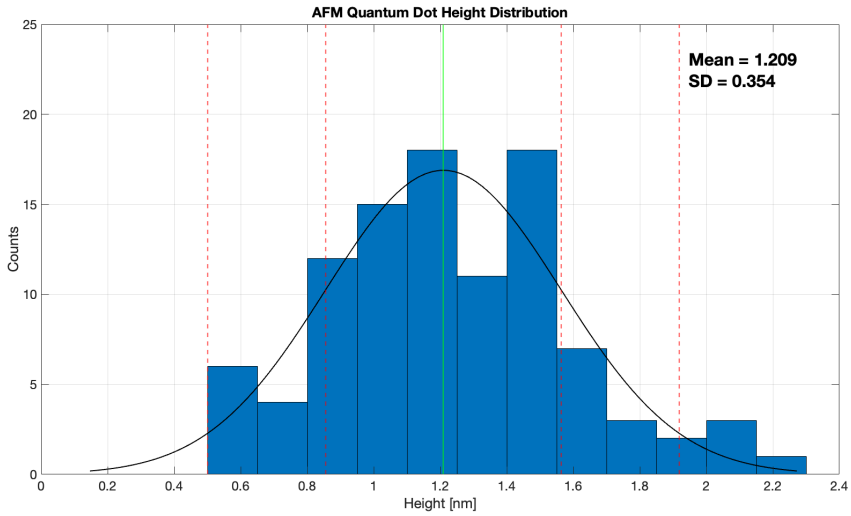

Figure 2.7 - AFM QD height distribution

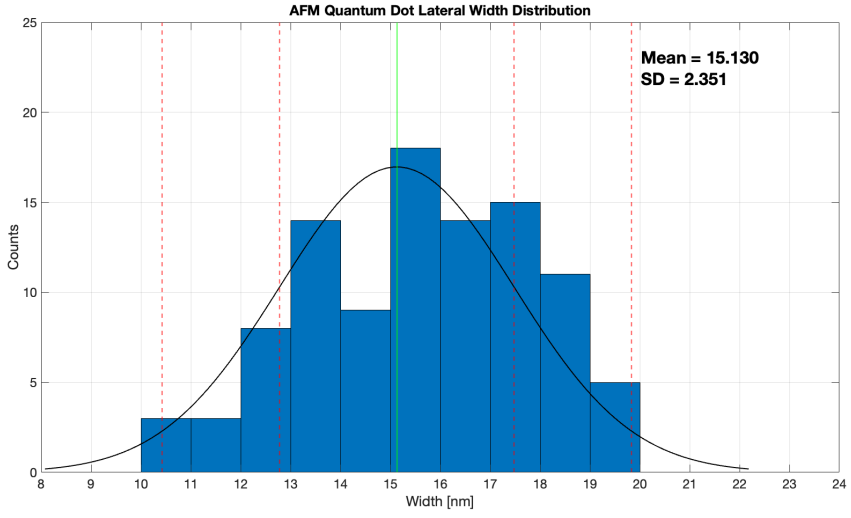

Figure 2.8 - AFM QD lateral width distribution

The corresponding height and width obtained through AFM of the QD ensemble.

$$height = 1.2 \pm 0.7\ nm$$

$$width = 15.1 \pm 4.7\ nm$$

There are ~115 quantum dots in the scan shown in fig. 2.5. Using the area of the scan, the quantum dot density has been calculated. Only the largest quantum dots may be observed through AFM, therefore this would correspond to a lower bound on the dot density.

$$density = \frac{number\ of\ QDs}{scan\ area} \approx \frac{115}{\left(2.5 \times 10^{-5}\right)^2} \approx 1.84 \times 10^{11}\ \ \frac{dots}{cm^2}$$

The island density saturates at a certain InAs coverage above the critical thickness for nucleation.[15] Additional deposition results in larger islands and eventually dislocations.[15] Quantum dot density must be high to ensure large optical gain. Increases to dot density are limited by spatial restrictions.[15] If the dots were assumed to have a width of 20 nm and are closely packed together, their density would be limited to $3 \times 10^{11}\ cm^{-2}$.[15] Therefore, based on the calculated lateral width, the density obtained through AFM is very high. In literature, larger quantum dots with approximately 20 nm lateral width, 4 nm height, and $5 \times 10^{10}\ cm^{-2}$ density have been demonstrated to have an emission wavelength of 1218 nm with FWHM of 120 nm during room temperature photoluminescence spectroscopy.[23] Therefore, it would be expected that the quantum dots obtained during this growth will emit at shorter wavelengths, as they are smaller (less InAs coverage to chance dislocating) and more dense.

2.4 Transmission Electron Microscopy

The HAADF (high-angle annular dark field) image in fig. 2.9. is used to visualize the entirety of the structure and all of the grown layers. The sample has been milled using a plasma focused ion beam (PFIB). This is a process that involves using an inert gas to form a focused beam on the sample to etch away material. Since the gas is inert it does not interact with the material to change its chemical composition. This step is crucial for TEM, as the cross section of the sample must be thin enough (~ less than 50 nm)[24] to be electron transparent. If it is too thick, multiple diffraction events reduce the imaging spatial resolution. Additionally, electron beam channelling between atomic columns will lead to inaccurate EELS (electron energy loss spectroscopy) spectra. Sample preparation is a highly important aspect for TEM. For this experiment, the Thermo Scientific Talos 200X was used with 0.1 nm spatial resolution and 0.65 eV energy resolution for EELS.

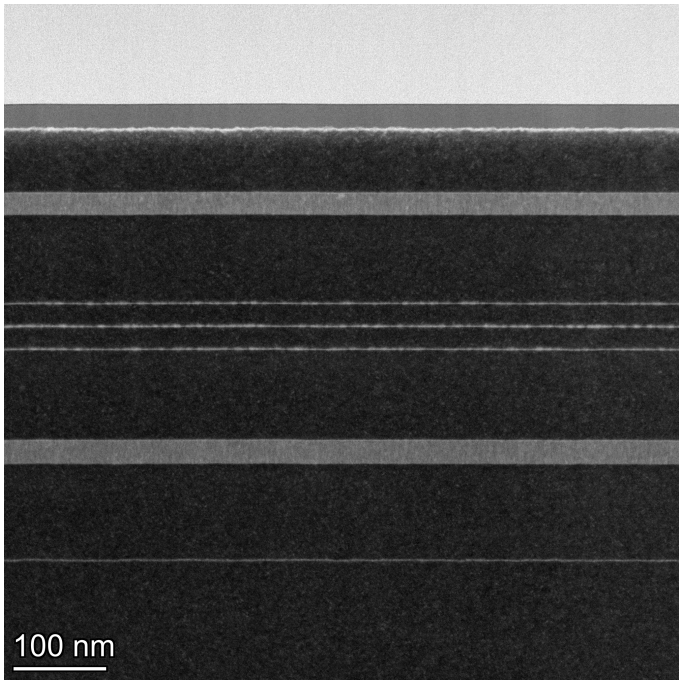

Figure 2.9 - HAADF image of complete sample. [110] beam direction

HAADF imaging is a technique that captures the electrons that are scattered at high angles. Electrons which pass through the sample and are scattered at small angles are not collected by the detector. This is because they are blocked by the aperture, which is variable in size. Since indium is a heavier element than gallium, areas of higher concentration of indium will induce more scattering. The Rutherford scattering cross section, σ_R, describes elastic scattering of electrons with the nucleus of atoms.[24] $\sigma_R \propto Z^2$ where Z is the atomic number. However, it ignores interactions with the electron cloud, but is a good approximation for high scattering angles.[24] At lower scattering angles, inelastic scattering and electron cloud interactions dominate such that the scattering cross section becomes $\sigma \propto Z^{4/3}$.[24] The screening parameter, θ_0, governs the approximate transition between low-to-high-angle scatter.[24]

$$\theta_0 = \frac{\lambda Z^{1/3}}{2\pi a_0} \tag{2.1}$$

a_0 is the Bohr radius and λ is the wavelength of the incident electron beam. The three indium rich layers will have a greater scattering cross section than the GaAs.

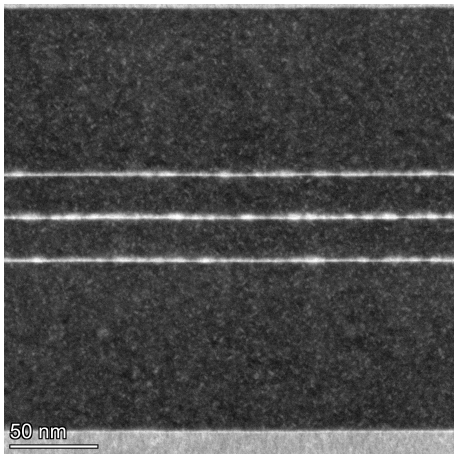

Figure 2.10 - HAADF image of indium rich layers

Since SK growth involves 2-dimensional planar growth followed by 3-dimensional island nucleation, it is possible to witness both these aspects in the HAADF image. All three quantum dot layers are composed of a wetting layer with thick clusters of indium throughout. Quantitative results for the sizes of these clusters is possible using HAADF images with single atom spatial resolution. The atomic columns of indium and gallium are visible by the projection of the zinblende unit cell on the family of {110} planes since the beam is oriented along the <110> zone axis.

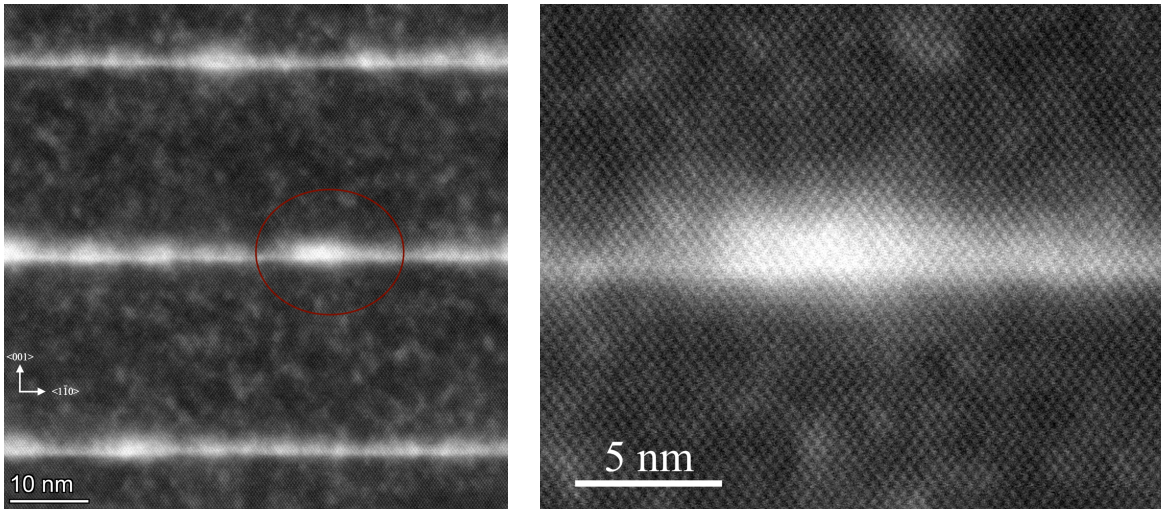

Figure 2.11 - HAADF image of QD core with atomic resolution

The image was converted to an 8-bit greyscale map, where each pixel has a value ranging from 0 (black) to 255 (white). The pixels were averaged along both crystallographic directions to obtain a Gaussian distribution for the pixel intensity, normalized to the 8-bit maximum. The pixels were then converted to their real space value to asses the dimensionality of the cluster displayed in fig. 2.11. The cluster has a radial height of $7.2 \pm 2.1\ nm$ along the growth axis and a radial width of $8.5 \pm 6.0\ nm$.

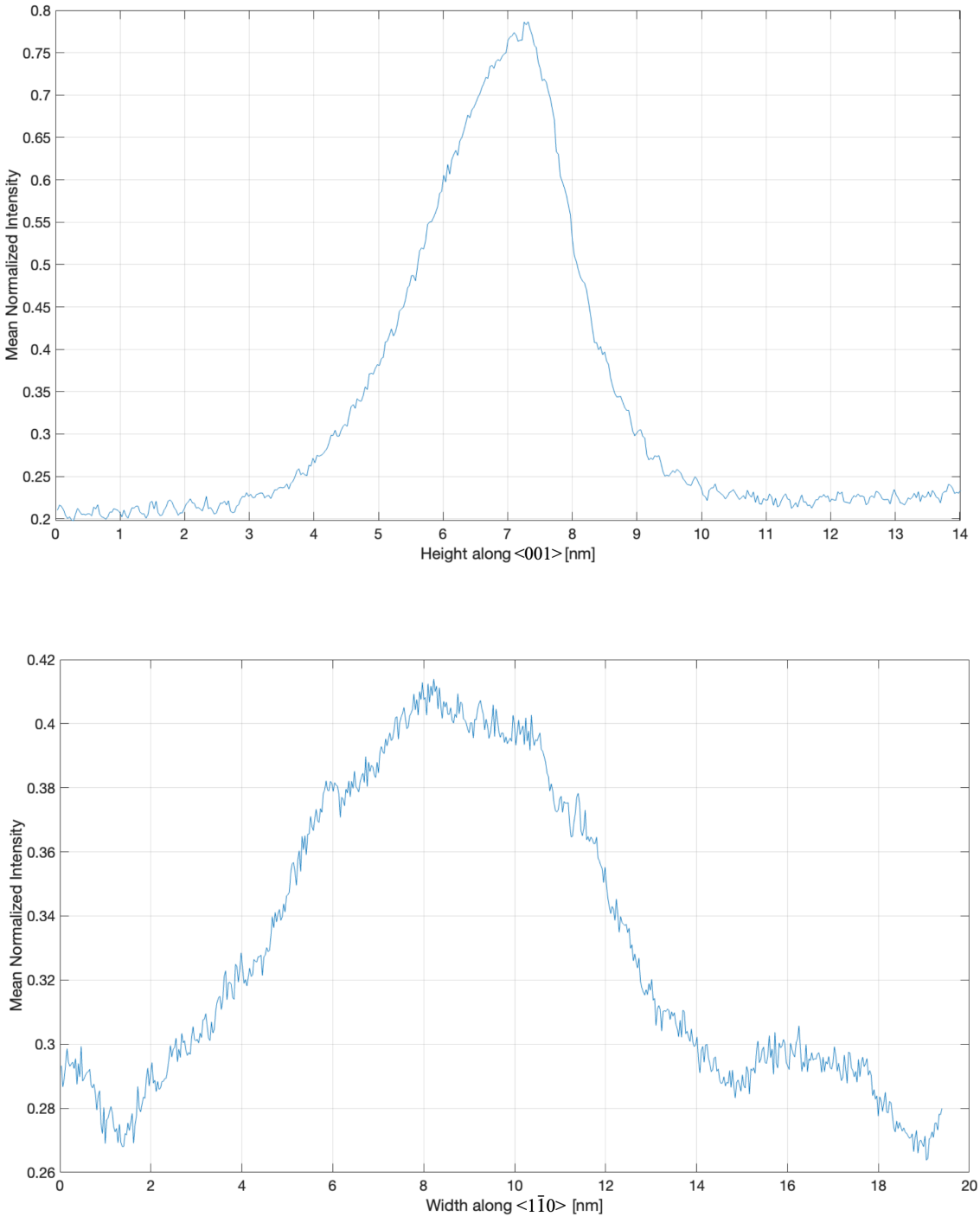

Figure 2.12 - Greyscale intensity distribution for QD height (top) and width (bottom)

The error in measurement for the height and width are due to the intensity FWHM of the distributions shown in figure 2.12. The double standard deviation has been calculated by assuming the distribution is Gaussian (example shown later in chapter 4.1). It should be emphasized that the values listed for the height and width are radial, meaning that they assess the distance to the QD core, not the entire cross sectional height/width. In contrast to AFM, the entire height of the quantum dot is visible. AFM only allows the height to be realized with respect to the surrounding wetting layer, whereas TEM is able to depict how deep the indium penetrates into the GaAs matrix. The radial height is approximately 6 times larger than the height observed through AFM. Similarly to AFM, the lateral resolution of the cluster is not ideal as the exact edges become blurred with the surrounding wetting layer, creating a large standard deviation for the cluster width. This particular cluster, assessed through TEM, has a radial width that is close to the ensemble radial width observed through the AFM lateral measurements ($7.6 \pm 2.3\ nm$), and both agree within the large bounds of confidence of one another.

Even with atomic resolution, the contrast between indium and gallium atomic columns is not large enough to precisely determine the bounds of the quantum dot with small uncertainty. The uncertainties on both the height and width would have drastic implications on the confinement energy. As will be derived in section 3.1 for the energy eigenstates of the infinite spherical well of radius a,

$$E \propto \frac{1}{a^2} \tag{2.2}$$

a is now translated to include 95% confidence uncertainty (double standard deviation).

$$a' = a \pm 2\sigma = (1 \pm \frac{2\sigma}{a})a \tag{2.3}$$

$$E' \propto \frac{1}{a'^2} = \frac{1}{a^2}\left[1 \pm \frac{2\sigma}{a}\right]^{-2} \tag{2.4}$$

Using the smaller uncertainty above for the height of the cluster, $2\sigma \approx \frac{a}{3}$.

$$E' \propto \left[1 \pm \frac{1}{3}\right]^{-2} E \tag{2.5}$$

Therefore, if the well radius is on the upper bound of the uncertainty ($+2\sigma$), the confinement energy would decrease by almost half compared to the mean value. Whereas, if the well radius was on the lower bound of the uncertainty (-2σ) it would be increased by over double. The lower bound results in a larger change since

$$\frac{dE}{da} \propto \frac{1}{a^3} \tag{2.6}$$

As a gets smaller, the change in confinement energy becomes larger since $\frac{dE}{da}$ diverges to $+\infty$ as $a \to 0$. This effect is important since it breaks down infinite spherical models as the size of the QD is decreased below a certain threshold. Experimental observations for transition energies in the strong confinement limit ($a < 2\ nm$) do not match these models.[25] Finite barrier potentials and interfacial polarization effects from the connected dielectric media must be incorporated to correct this divergence.[25]

As demonstrated in chapter 1, fine changes in energy to the eigenstates have major implications on many aspects of the device performance by altering the carrier dynamics. Any uncertainty on the size of the well will cause large changes to the confinement energy. Since the well radius can be anywhere within a range of $a \pm 2\sigma$, this creates a very broad region for which the true eigenenergy can reside. Additionally, this section encompassed a singular quantum dot. As more quantum dots are added to the ensemble, the distribution for the well radius would broaden due to cluster size inhomogeneity.

2.5 Stacking Fault Dislocation

The TEM data was able to capture one defect throughout the region of the FIB cut. This was the only dislocation that could be observed, however it is possible other dislocations exist that glide along the interfaces and do not thread throughout the structure. Low dislocation density provides the benefit of inhibiting charge carrier traps that would hinder exciton recombination and thereby decrease the intensity of the photoluminescence spectra. The dislocation did not penetrate completely into the uppermost buried quantum dot layer. The reason for this occurrence is apparent when the boundary of the dislocation is observed. A stacking fault forms at this location and growth continues on top of it. This dislocation type is typical for InAs quantum dots grown on GaAs (001) due to stacking faults along the {111} family of planes.[26] This creates a plane of structural weakness that is easily dislocated. When the surface quantum dots are grown, strain relaxation mechanisms allow this fault line to be dislocated.

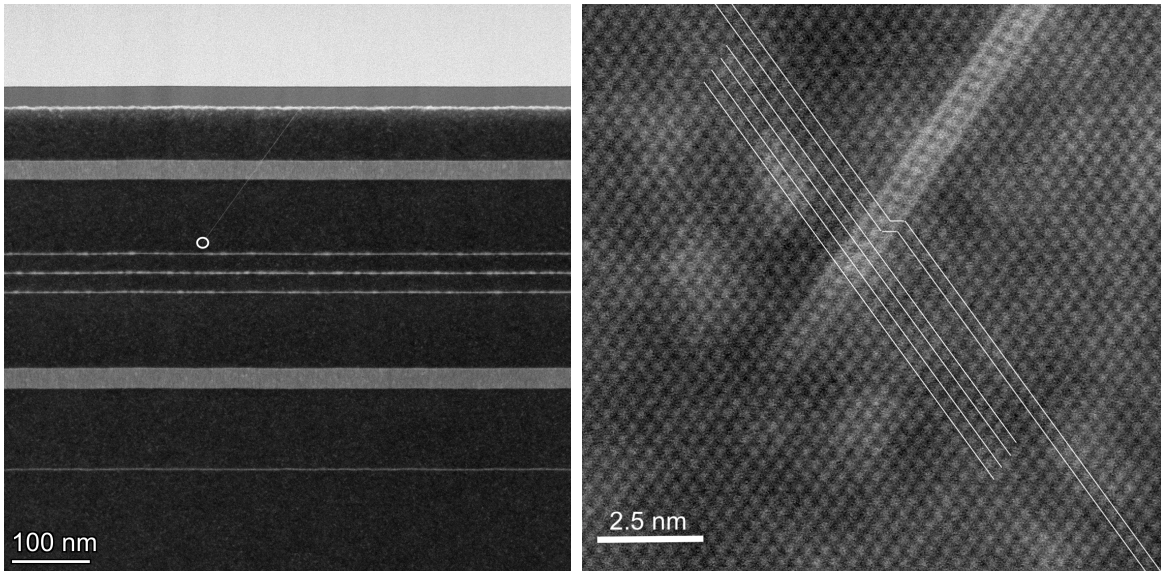

Figure 2.13 - Stacking Fault Dislocation

Stacking faults create defects in the lattice such that threading could occur from misfit dislocations as strain accumulates during indium deposition. To achieve S-K growth, the coherent two dimensional growth regime is necessary before 3-dimensional island formation. This is because sufficient strain energy is needed to accomplish nucleation. However, as 2-dimensional growth occurs there is enough strain in the lattice to cause misfit dislocations.[27] Interatomic potentials and surface energy calculations have been used in literature to demonstrate that the onset for misfit dislocations in the GaAs (001) system appears at 0.6 ML of deposited InAs.[27] By using a double shutter sequence, half of the target number of monolayers (0.85 ML) were deposited before the shutter was closed and reopened following the short growth interruption. Though this enhances migration of indium adatoms to create larger islands,[16,28] it would also cause sufficient strain energy in the lattice for misfit dislocations.[27]

2.6 Z-Contrast

The core of the quantum dot in fig. 2.11 appears bright and indicates a richness of indium. The plots in 2.12 were generated using greyscale pixel intensity maps. Refining the bounds such that the selection goes along the growth axis and exclusively through the centre of the core results in a maximum greyscale intensity of $I_{max} \approx 0.97$. This is different than the intensity observed in figure 2.12, since the analysis used a broader selection which included the surrounding non-core region. I_{max} has been normalized to the 8-bit greyscale maximum value of 255 (pure white). As there is presumably no indium in the surrounding GaAs matrix at this stage of the analysis (see section 3.9 if interested), the background intensity is $I_{background} \approx 0.2$. Subtracting the background intensity from the core, $I_{core} \approx 0.77$. Since the intensities have already been normalized, I_{core} represents a percentage change from the background. Therefore, the contrast is[24]

$$C = I_{core} \tag{2.7}$$

The contrast can be directly related to the concentration, c_{In}, of the alloying element[24]

$$C = \left(\frac{\sigma_{Ga}}{\sigma_{In}} - F_{In}\right) c_{In} \tag{2.8}$$

where F_{In} represents the fraction of the alloying element that substitutes for matrix atoms. Assuming In replaces Ga at a 1:1 ratio in the alloy (for every 1 gallium atom lost, 1 indium atom is gained at the lattice site), then $F_{In} = 1$. The scattering cross sections for gallium and indium is denoted by σ_{Ga} and σ_{In} respectively.[24]

$$\sigma = \frac{Z^{\frac{4}{3}}\lambda^2\left[1+\frac{E_0}{m_0c^2}\right]^2}{\pi\left[1+\left(\frac{\beta}{\theta_0}\right)^2\right]} \tag{2.9}$$

E_0 is the incident energy, λ is the incident wavelength, m_0 is the electron rest mass, β is the angle of collection of the objective aperture (> 50 mrad for HAADF)[24], and θ_0 is the characteristic screening angle defined in equation (2.1). Using a $V = 200\ kV$ incident beam, the relativistically corrected electron wavelength is

$$\lambda = \sqrt{\frac{1.5}{V + 10^{-6}V^2}} = 2.5 \times 10^{-12}\ m \tag{2.10}$$

Using the bulk Bohr radius of $a_{0,InAs} = 34\ nm$[29] and $a_{0,GaAs} = 11.6\ nm$.[30]

$$\theta_{0,GaAs} = \frac{\lambda Z^{1/3}}{2\pi a_{0,GaAs}} = \frac{(2.5\times10^{-12})(31)^{1/3}}{2\pi(1.16\times10^{-8})} \approx 1.08\times10^{-4}\ rad \tag{2.11}$$

$$\theta_{0,InAs} = \frac{\lambda Z^{1/3}}{2\pi a_{0,InAs}} = \frac{(2.5\times10^{-12})(49)^{1/3}}{2\pi(3.4\times10^{-8})} \approx 4.28\times10^{-5}\ rad \tag{2.12}$$

Solving for the relativistic energy and scattering cross sections

$$E_0^2 = (pc)^2 + (m_0c^2)^2 \tag{2.13}$$

$$E_0 = \sqrt{\left(\frac{\hbar 2\pi c}{\lambda}\right)^2 + (m_0c^2)^2} \tag{2.14}$$

$$\therefore \frac{E_0}{m_0c^2} = \sqrt{\left(\frac{\hbar 2\pi}{\lambda m_0 c}\right)^2 + 1} \approx 1.39 \tag{2.15}$$

$$\sigma_{Ga} = \frac{Z_{Ga}^{\frac{4}{3}}\lambda^2\left[1+\frac{E_0}{m_0c^2}\right]^2}{\pi\left[1+\left(\frac{\beta}{\theta_{0,GaAs}}\right)^2\right]} = \frac{(31)^{\frac{4}{3}}(2.5\times10^{-12})^2\left[1+1.39\right]^2}{\pi\left[1+\left(\frac{50\times10^{-3}}{1.08\times10^{-4}}\right)^2\right]} \approx 5.16314\times10^{-27}\ m^2$$

$$\sigma_{In} = \frac{Z_{In}^{\frac{4}{3}}\lambda^2\left[1+\frac{E_0}{m_0c^2}\right]^2}{\pi\left[1+\left(\frac{\beta}{\theta_{0,InAs}}\right)^2\right]} = \frac{(49)^{\frac{4}{3}}(2.5\times10^{-12})^2\left[1+1.39\right]^2}{\pi\left[1+\left(\frac{50\times10^{-3}}{4.28\times10^{-5}}\right)^2\right]} \approx 1.49303\times10^{-27}\ m^2$$

$$\therefore \frac{\sigma_{Ga}}{\sigma_{In}} \approx 3.458$$

Rearranging equation (2.8)

$$c_{In} = \frac{C}{\frac{\sigma_{Ga}}{\sigma_{In}} - F_{In}} = \frac{0.77}{3.458-1} \approx 0.31$$

Therefore, by Z-contrast HAADF, the core of the QD cluster depicted in figure 2.11 is made of $In_{0.31}Ga_{0.69}As$. It will be shown in the subsequent chapters by atom probe tomography that this is a very accurate measurement of the indium concentration in the quantum dot core. Other techniques such as Energy-Dispersive X-Ray Spectroscopy (EDS) and Electron Energy Loss Spectroscopy (EELS) have been employed to assess the remainder of the structure using TEM.

2.7 EDS and EELS

Energy-Dispersive X-Ray Spectroscopy (EDS) allows for the chemical composition to be assessed within the TEM. The process consists of exciting electrons from various shells which would then emit an X-ray as they return to the unexcited state. The energy of the X-ray is characterized by the electron shell that was ionized, with each chemical species having their own ionization energies for their various electron shells. This allows the X-ray spectra to be collected and the intensity determines the chemical composition based on the known transition energies.

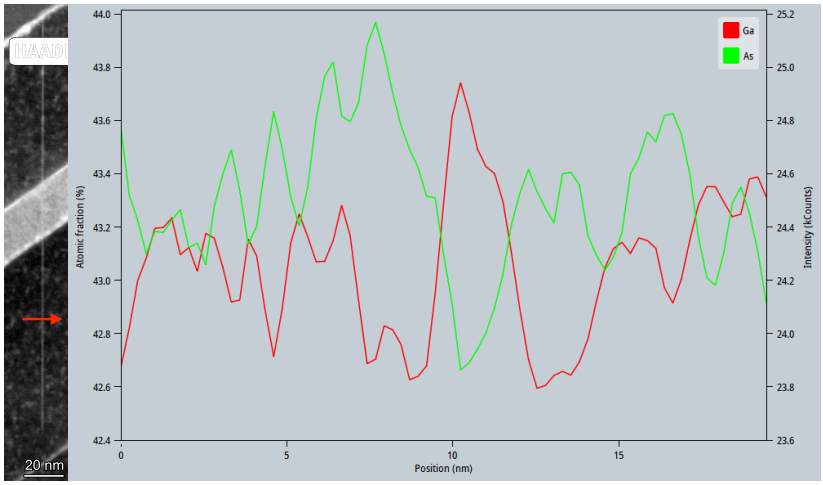

Figure 2.14 - EDS of Stacking Fault Dislocation

Figure 2.14 shows an EDS line scan taken across a stacking fault. There exists a higher density of gallium along the fault plane. Fig. 2.15 demonstrates an EDS line scan across the entire structure to assess the chemical composition throughout all grown layers. There may exist biasing due to certain electron shells being ionized more readily than others or lack of counts from too short a measurement time.

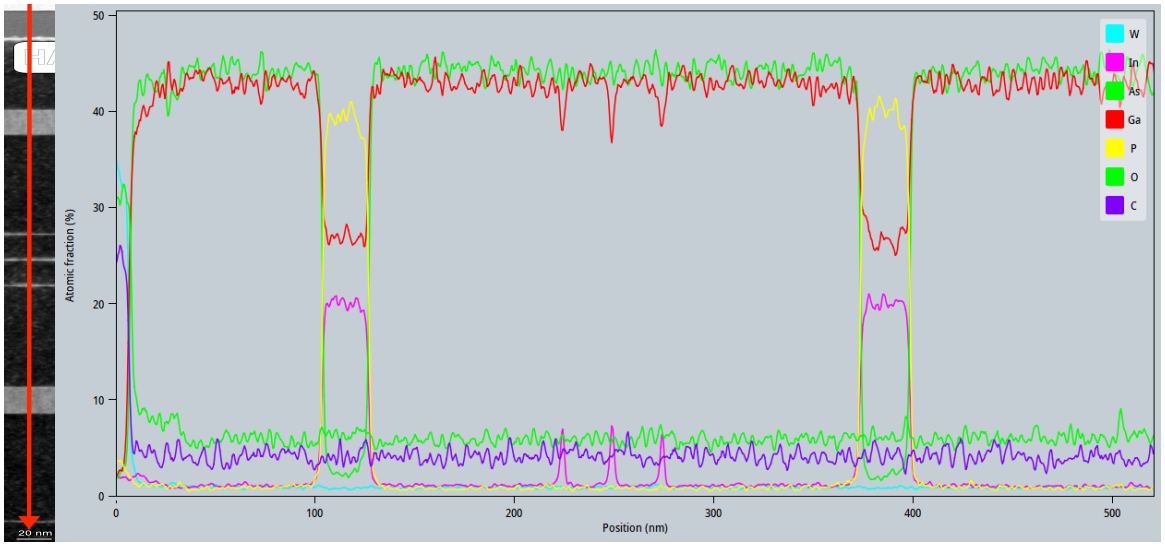

Figure 2.15 - EDS Line Scan of Entire Structure

Electron Energy Loss Spectroscopy (EELS) is a useful tool to infer the chemical composition throughout the structure in conjunction with EDS. Inelastically scattered electrons are collected as they pass through the sample and the amount of energy loss determines the spectra. The intensity of the spectra is used to asses the chemical composition. The only disparity in the data that existed between EDS and EELS was the presence of an indium signal in the pure GaAs region. The EDS line scan in Fig. 2.15 shows that these regions should contain less than 2% indium; likely as a result from statistical noise which is within the 2-4% precision indicated by Thermo Fisher.[31] The presence of indium in the GaAs regions using EELS is either due to an imperfect background subtraction of the spectra or it may be present in low quantities (chapter 3.9).

The TEM has reached scientific feats that are remarkable for microscopy, providing the ability to produce images that are accurate down to the atomic scale. The one downfall of the TEM is that it is only capable of extracting quantifiable data along a particular plane. Regardless of which plane is utilized as a cross section, only a recreation of a 2-dimensional projection of the atomic columns is possible. Any aspect of 3-dimensional morphology becomes constrained to just two dimensions. As many nanostructures are inherently 3-dimensional objects, this becomes a large detriment toward both the visualization and physical simulation for any such structure. Atomic concentration becomes a planar representation of physical reality. This creates a need for an established technique which allows for the visualization of chemical composition in all 3-dimensions with a spatial resolution that is on par with the transmission electron microscope. Any plane could be cut and visualized at will, whereas hours would be required for sample preparation on a TEM. However, transmission electron microscopes are still critical tools for determining crystal orientation as well as any defects, dislocations, or interfaces that cannot be resolved otherwise.

2.8 Atom Probe Tomography

Atom probe tomography (APT) was used to assess the true size distribution and chemical composition of quantum dot cores buried deep within the structure such that they could be compared to AFM and TEM. Atoms were ionized using a laser pulse rate of 250 kHz and laser pulse energy of 0.3 pJ at a temperature of 40K. APT experiments use a constant detection rate and the voltage of the applied electric field is altered to achieve this target.[32] The detection rate was held constant at 0.5%, indicating that on average 5 out of every 1000 laser pulses induces a detection event, which could be a single or multiple hit.[33] The GaAs matrix requires low laser pulse energy for uniform field evaporation from the sample tip (figure 2.16), allowing for lower electric field voltages which ensure the tip is not destroyed. The system that was used is the Local Electrode Atom Probe (LEAP) 5000 XS from CAMECA Instruments Inc. The LEAP 5000 XS is a straight-flight-path APT with path length 100 mm and detection efficiency of ~80% of the total atoms.[33] The spatial resolution is 0.1-0.3 nm in depth along the growth axis and 0.3-0.5 nm laterally.[34] A total of 24 million ions were collected for the experiment.

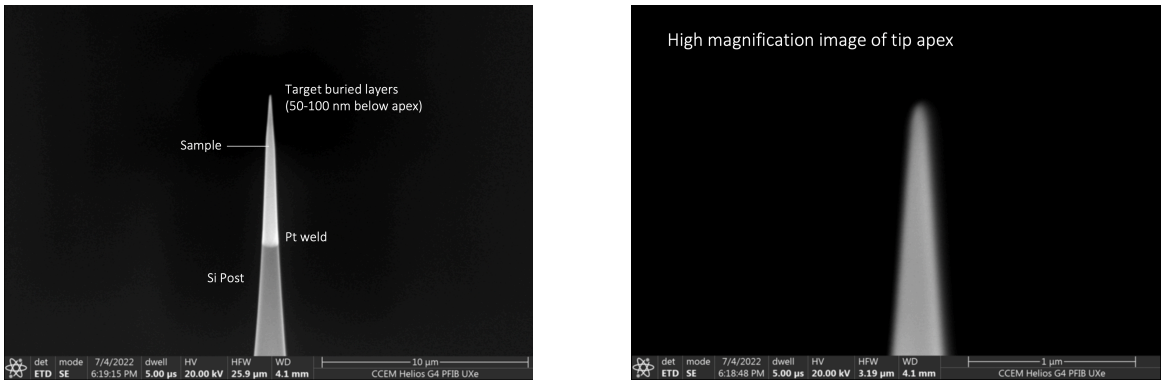

Figure 2.16 - SEM of sample tip

2.9 Evaporation Fields

A surface electric field is generated by ionizing many complexes at the tip. The electric field strongly impacts the specimen's evaporation and changes locally depending on different crystallographic structures, atoms, or phases. Some ionized complexes are more straight forward than others, having fewer stable isotopes and charged states.

Each complex will have its own evaporation field associated with it, which determines the amount of biasing by making certain complexes more likely to induce a detection event. For example, As^{2+} has an evaporation field of 42 V/nm while As^{+} and As^{3+} have larger evaporation fields of 46 V/nm and 54 V/nm respectively.[35] The spectra will also be determined by the laser pulse energy as this will dictate which complexes are detected.[36] In the InGaAs material system As^{+} and As^{3+} are favoured when using a laser pulse energy of 5 pJ while As^{2+} is the dominant complex when using a lower laser pulse energy of 0.005 pJ.[37] This has been hypothesized to be due to thermal irradiation by the laser as the surface temperature of the atoms substantially increase and the lower vapour pressure elements (arsenic and phosphorus) undergo sublimation.[36] Surface migration can occur more easily for group V atoms due to their lower activation energy for diffusion in conjunction with laser heating effects and local field gradients.[38] This causes group V atoms to migrate to the tip surface during field evaporation, forming clusters of neutral molecular ions that are undetected by the mass spectrometer.[38] The impact of the field intensity may also drive this occurrence,[38] leading to an overestimation or an underestimation of these group V complexes depending on the field strength.

More importantly, the detection ratio between In^+ and Ga^+ ions was not observed to change under different laser pulse energies.[36] This is likely due to their similar evaporation fields of 12 V/nm and 15 V/nm for In^+ and Ga^+ respectively.[35] This is important for the purpose of this report since these will be the primary ions of interest used later to derive potential wells based on band theory. The evaporation fields for the double charged ions of In^{2+} and Ga^{2+} are 31 V/nm and 39 V/nm.[35] These complexes were also observed in the collected atom probe data.

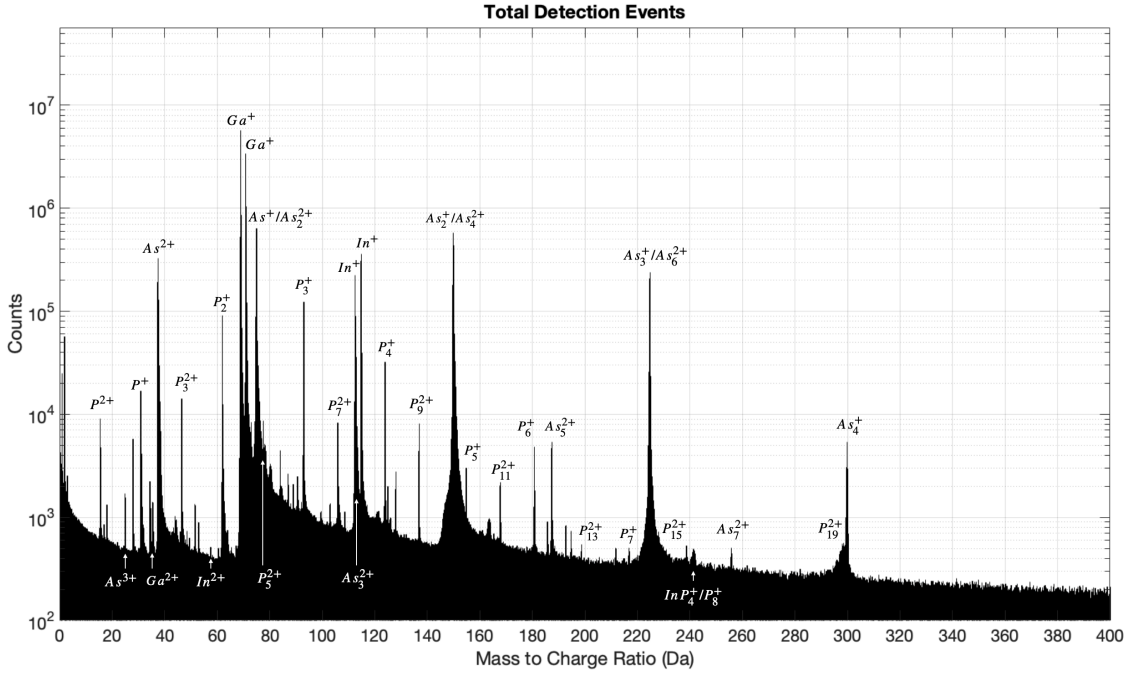

Figure 2.17 - Spectra of total detection events from APT experiment

The evaporation fields for phosphorus complexes are unknown in literature[36] An overall field of 15.2 V/nm was calculated using an InP system (0.25% detection rate, 3 nJ laser energy, 100 kHz pulse rate, and 50K temperature) acquiring only the In^+ complex and many phosphorus complexes, namely P_k^+ and P_k^{2+} for $k \geq 1$.[38] Typically, the species undergoes dissociation reactions for higher charged states to create more stable configurations conserving both mass and charge.[38] P_{2k}^{2+} complexes are also hidden in the spectra as they are superimposed with P_k^+.[38] Many of the phosphorus complex peaks are near other elemental peaks within the spectra. This is especially true with arsenic since they both form many different complexes. Peaks in the spectra that overlap or form thermal tails into other peaks contribute to broadening as the ions are distributed throughout the entire sample volume. APT mapping in figure 2.18 shows phosphorus incorporation in the GaAs, whereas EDS mapping showed none of statistical significance.

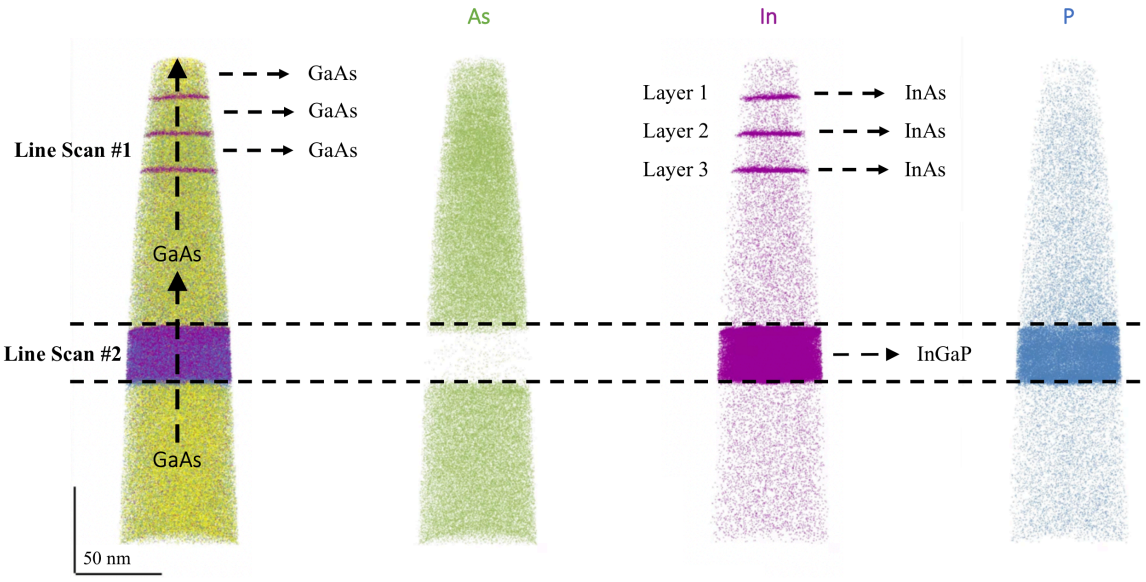

Figure 2.18 - APT chemical map

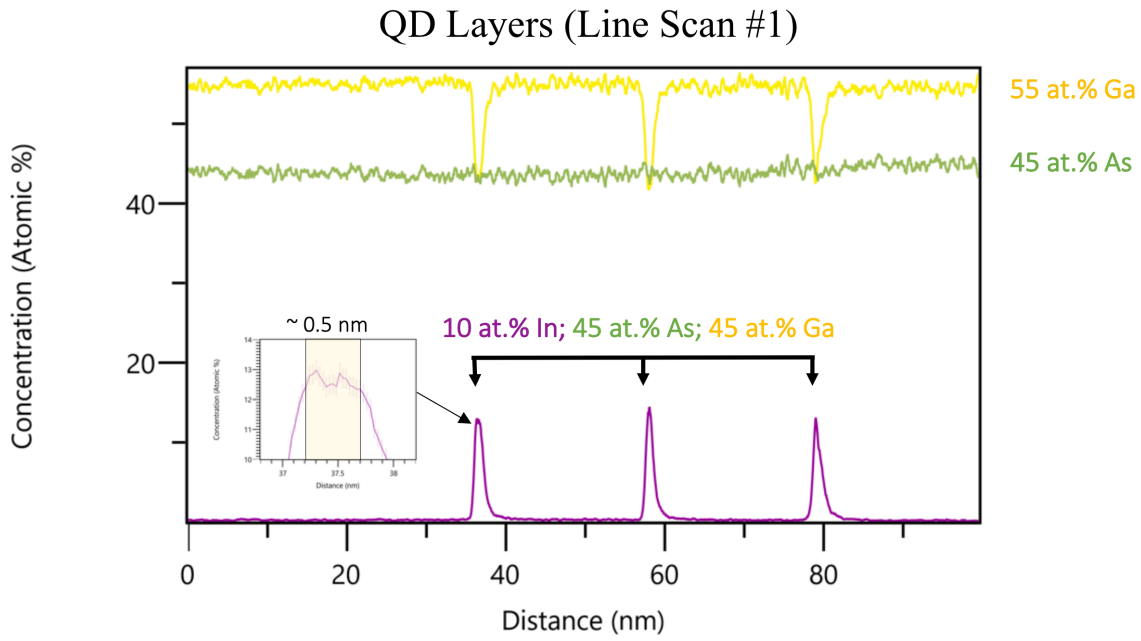

Figure 2.19 - Line scan of QD layers in figure 2.18 (rectangular volume)

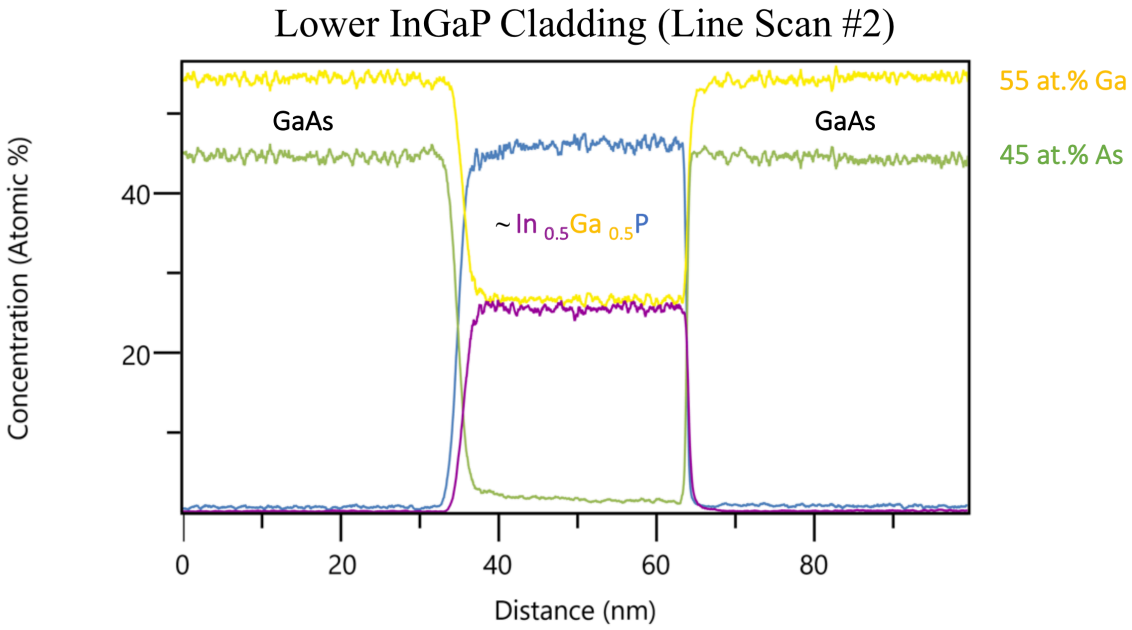

Figure 2.20 - Line scan of lower InGaP layer in figure 2.18 (rectangular volume)

2.10 Spectra Overlap

One potential source of error for the analysis presented in this paper is due to the mass-to-charge ratio overlap between the In^+-113 isotope and the As_3^{2+} complex (~112.4 Da). This would have consequences in the analysis since it becomes difficult to distinguish between them, whereas Ga^+ and Ga^{2+} have separation between any nearby arsenic complexes. This introduces either an under representation of indium if the isotope was neglected, or an over representation if the isotope is included. Fortunately, this problem can be set aside for several reasons. The utilized laser pulse energy and detection rate mitigates this issue as the group III elements are selectively biased over the group V elements due to the magnitude of the electric field. This can be seen in the line scans above which show a stoichiometry that is not 1:1 in the GaAs regions. Furthermore, the total detection event histogram represents the entire structure, which would overall contain more total arsenic atoms than indium atoms. Since there are more arsenic complexes that can be formed than indium complexes, it would become less probable that an event in the QD layers is due to that specific arsenic complex instead of the indium isotope. The arsenic complex, As_3^{2+}, also does not have any degeneracy associated with it which would increase the intensity of the peak, such as with the As^+/As_2^{2+} peak. Similarly to the higher charged state phosphorus complexes, this is because As_6^{4+} would dissociate into more stable configurations. For these reasons, the In^+-113 isotope was included in the proceeding analysis with a limit at 112.75 Da to avoid As_3^{2+}.

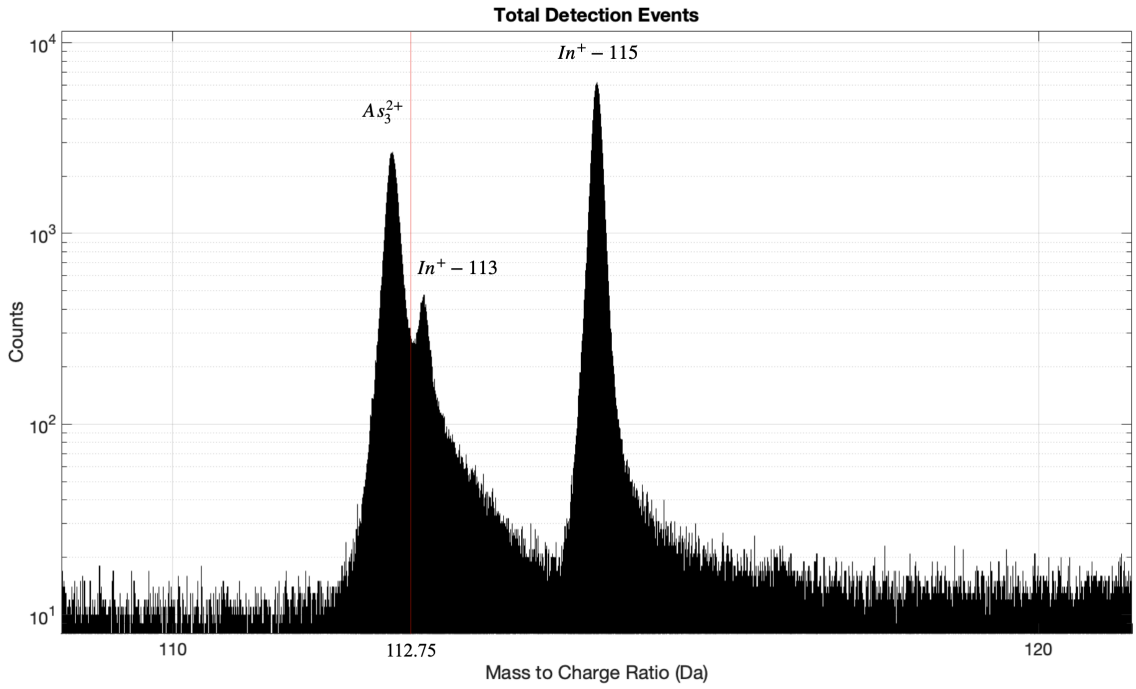

Figure 2.21 - Peak overlap between In^+-113 and As_3^{2+}

2.11 Interfacial Disparity

One noticeable difference between the atom probe chemical mapping versus EELS and EDS is that the interface between regions appears to be more rounded. This is an artefact that is due to the transition between material systems and the altering of the electric field.[39] The effective radius of the hemispherical tip deviates and leads to distortion in the field of view since the depth coordinate is determined by the time-of-flight from the apex.[39]

The interface is compressed when evaporating from a material with a higher evaporation field into one with a lower evaporation field, and it is broadened when the

opposite takes place (lower-to-higher evaporation field).[39,40] This is dependent on the sequence of evaporation which assumes a uniform layer-by-layer approach across the surface of the tip. Evaporation occurs parallel to the growth axis, beginning at the top, and penetrating lower into the structure. As an example, using the surrounding region of the lower InGaP cladding for analysis, first the upper GaAs is evaporated, then the InGaP, followed by the lower GaAs. Referencing the line scan, it can be seen that the bottom interface of the InGaP is broadened and the top interface is compressed. The depletion/ accumulation of ions spans more than double the width for the broadened (bottom) interface than the compressed (top) interface. This indicates that the evaporation field for InGaP is lower than GaAs, leading to preferential evaporation of phosphorus and retention of arsenic when transitioning between the heterogeneous materials.[41]

This effect is not noticeable in the quantum dot layers. $In_xGa_{1-x}As$ would have an overall lower evaporation field than GaAs based on the fields for indium and gallium complexes. Similar to the InGaP region, it would then be expected that the top interface is compressed while the bottom interface is broadened based on the evaporation sequence. However, the lower interface of the indium peaks appear sharper than the upper interface. This could be because there is not a significant composition of indium to drastically change the evaporation field. The geometry would also have an impact as the bottom interface should be more abrupt due to wetting layer accumulation. Surface nucleation would cause varying heights of the clusters so the indium content should taper more slowly toward the top interface.

The broadening at the upper interface could also be an artifact of how the rectangular volume region of interest was positioned. If it is not perfectly perpendicular to the interface, then the profile will be artificially broadened. This is also more likely to occur at the upper interface due to the rounding of the nucleation clusters. A more detailed view of the InGaP interface is located in Appendix 1. This biasing has been removed by using isosurfaces and proximity histograms as described in sections 2.14 and 2.15.

2.12 Quantifying Group III Preferential Evaporation by XRD

As the sample is evaporated, biasing can occur as a result of preferential evaporation between complexes. Different evaporation fields between atoms leads to certain ions being detected more readily. In the AlGaN system, biasing and correction techniques have been documented in literature to accommodate for this shortcoming.[42] Al^{+} and Al^{2+} have an evaporation field of 19 and 35 V/nm respectively.[35] This is similar to the evaporation fields for Ga^{+} and Ga^{2+} (15 and 39 V/nm).[35] Therefore, even if In^{+} and In^{2+} have similar evaporation fields compared to the gallium complexes, the effect of biasing must still be explored. The existence of biasing would be detrimental toward the optical simulation of the device as the inherent atom probe data would not be an accurate representation of the real structure. The biasing between group III and V elements was previously mentioned, however this would not change the results as the stoichiometry is assumed to be 1:1. Therefore, the primary interest was to explore if there exists any biasing between the group III elements in the atom probe data.

X-Ray Diffraction (XRD) was used to assess the InGaP cladding layers. Since the upper InGaP layer is closest to the surface, it will impact the X-Ray spectra more intensely than the lower layer. The atom probe data does not encompass the upper InGaP cladding layer, however they were both grown under the same conditions and can be used for a comparison. The line scan (fig. 2.20) of the layer shows that the indium and gallium concentrations are roughly split equally with a slight bias toward the gallium. The X-Ray spectra contains many small signal oscillations due to the complexity of the many layered structure. However, the InGaP layer can be successfully simulated based on matching to the GaAs substrate peak. It has been demonstrated in literature that $In_{1-x}Ga_xP$ is lattice matched to GaAs when $x \approx 0.51 - 0.516$.[43-45] Deviations above or below this value would lead to tensile or compressive strain in the layer due to lattice mismatch. Variations of x around the concentration of interest are presented in the specimen's XRD spectra (Appendix 2).

Elongated quantum dots that deviate away from a perfect spherical symmetry experience local lattice constant variations between planes[46], and smaller objects will introduce broad features into the XRD spectra. This produces a complicated spectra, but the $In_{1-x}Ga_xAs$ quantum dot layers could be neglected when trying to match the $In_{1-x}Ga_xP$ region to the large GaAs substrate peak (see Appendix 2).

The $In_{1-x}Ga_xP$ was targeted to be lattice matched to GaAs such that cladding layers could be incorporated into the structure without inducing any strain field. This means that the peak would be absorbed into the substrate peak of the GaAs. Based on the

surroundings of the major substrate peak (located at $\omega \approx 33.05°$), it is likely that the gallium concentration for the $In_{1-x}Ga_xP$ cladding layers is between 50-55%. If the gallium content is altered to be more or less than within this range, the intensity spectrum surrounding the GaAs peak becomes shifted to angles that would not correspond to the experimentally observed spectrum near the substrate peak. This is also within the standard uncertainty (2-4%) provided by EDS which demonstrated that the gallium content for this region was ~55%. Both of these measurements agree with the atom probe data that this region is on average more gallium rich by 1-2%. One caveat is that $In_{1-x}Ga_xP$ will not have an identical evaporation field to $In_{1-x}Ga_xAs$ and could potentially alter evaporation dynamics of indium and gallium. However, the atom probe line scan in fig. 2.19 for the $In_{1-x}Ga_xAs$ layers show $x \approx 0.78$ which is also within the uncertainty provided by EDS ($x \approx 0.82 \pm 0.04$). For the purpose of this thesis, any correctional techniques for atom probe biasing have not been employed and the APT data has been left in its raw state.

2.13 Preliminary Indium Mapping

The bottom QD layer shown in the line scan of fig. 2.19 contains a broad indium peak of ~0.5 nm width and slight bimodal nature. This aspect could exemplify that indium was deposited at slightly different heights along the growth axis due to surface corrugation and terraces. There could also exist alloying within the quantum dot layers as it was shown through Z-Contrast HAADF that the cores themselves consist of alloys. This would induce local fluctuations of indium, broadening the line scan.

According to the line scan in fig. 2.19, there exists significant gallium incorporation in the quantum dot layers (~ 78%, mentioned at the end of 2.12). This is very close to the amount obtained through Z-contrast HAADF of the quantum dot core, a value of ~69%. The spatial distribution of indium/gallium atoms is highly important throughout these layers, as it will indicate the degree of locality that the carrier wave functions will exhibit depending on the spatial distribution of ions within the layer. The following chapters will further delve into the quantum dot core concentrations and their size distribution. Figures 2.23-2.25 depict indium ion and concentration maps for each of the 3 QD layers. The view is aligned down the growth axis demonstrated in figure 2.22.

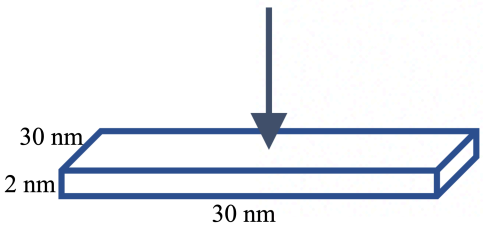

Figure 2.22 - Section used for mapping

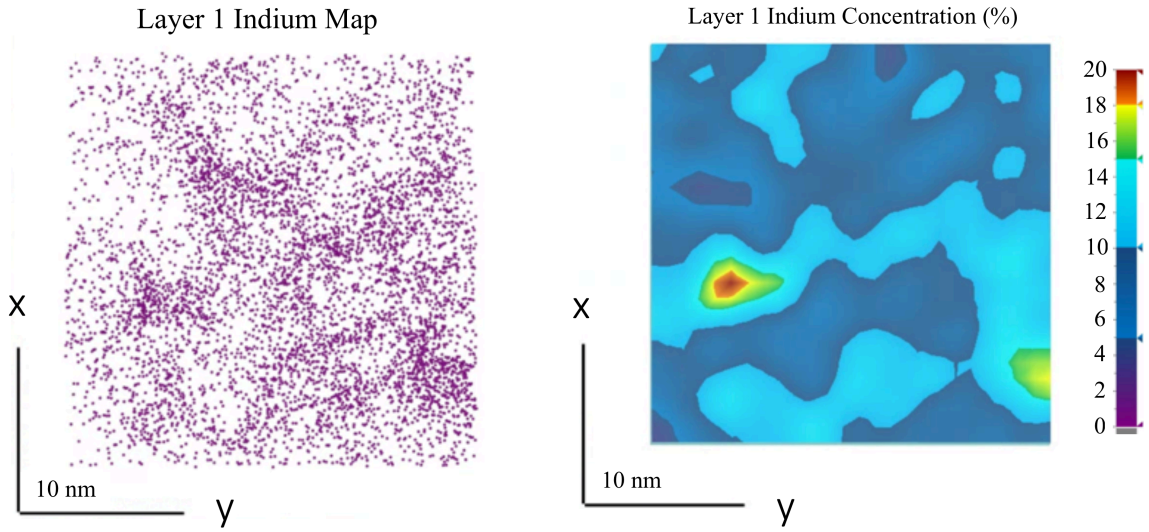

Figure 2.23 - Layer 1 Indium Maps

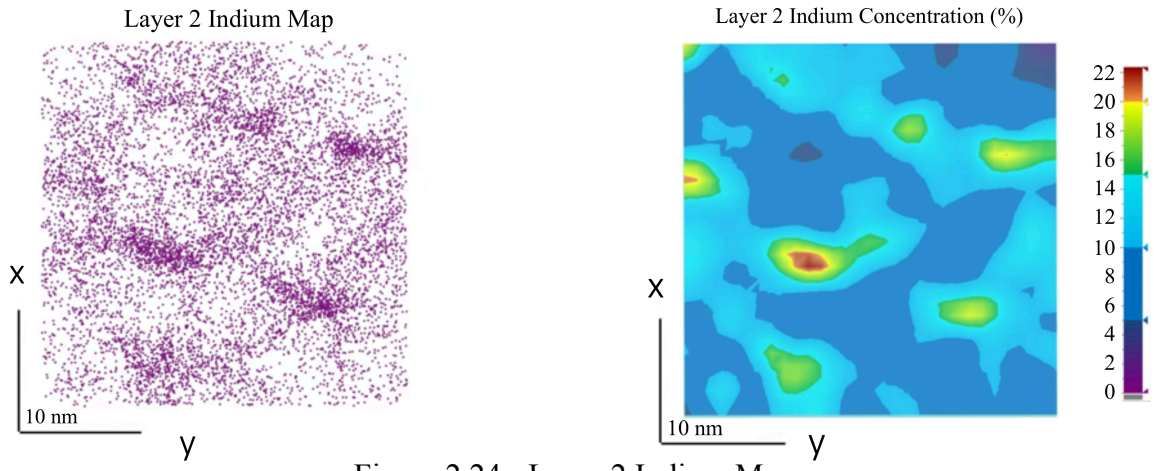

Figure 2.24 - Layer 2 Indium Maps

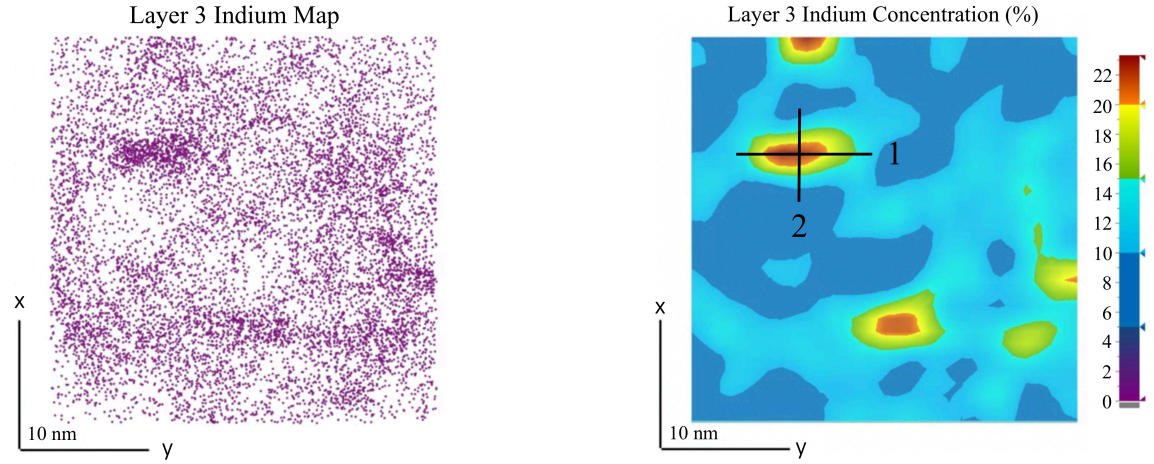

Figure 2.25 - Layer 3 Indium Maps

The crystallographic directions are unknown as the atom probe scatter data exists in an $\hat{x}, \hat{y}, \hat{z}$ basis set. This ensures that the $\hat{z}$ axis is fixed to the growth axis, yet the $\hat{x}$ and $\hat{y}$ axes can be rotated. Transmission Kikuchi Diffraction (TKD) may be useful to provide crystal orientation at the end of specimen preparation,[47] but this process induces structural damage as hydrogen and carbon surface species become implanted from the energetic electron beam.[48] Without TKD, the original crystallographic directions become lost as the sample is milled into a fine tipped needle and evaporated. The crystal orientation becomes difficult to recover even by means of sophisticated reconstruction algorithms.

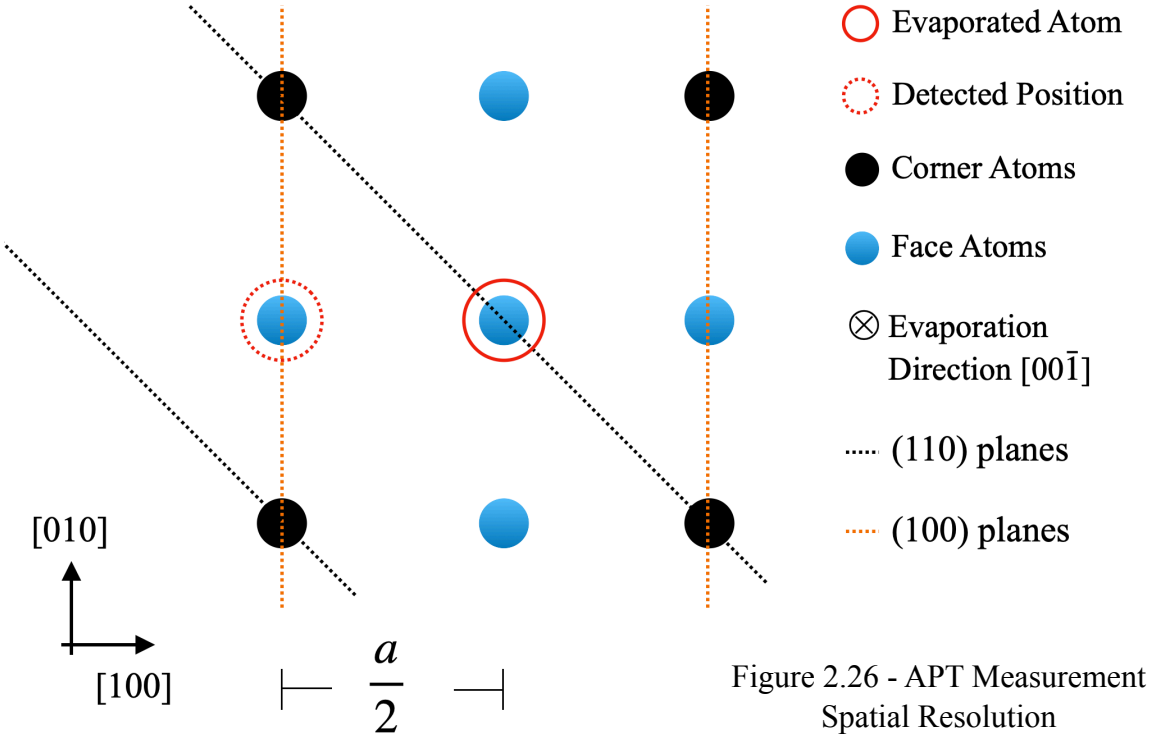

Figure 2.26 - APT Measurement Spatial Resolution

The difference between the evaporated atom position and its detected location are shown in fig. 2.26. Utilizing the lattice parameter of GaAs, $a \approx 5.65$ Å.[49] The spatial resolution orthogonal to the evaporation direction is 3-5 Å; parallel to the evaporation direction it is 1-3 Å. Trajectory aberrations cause a deterioration in the spatial resolution as the specimen is evaporated.[47] This means that even though an atom was evaporated from a particular plane, it could be detected on a different plane to which it does not belong. Since both the orthogonal and parallel spatial resolutions are significant compared to the size of the unit cell, a reconstruction of the planar arrangement of atoms is not possible. For this, TEM is needed during the experiment such that the $\hat{x}, \hat{y}, \hat{z}$ basis set can be related back to the crystallographic directions. The $\hat{x}, \hat{y}, \hat{z}$ basis set has been used for this thesis.

To assess the indium diffusion along the growth axis, $\hat{z}$, two 2 nm thick cross sections have been taken for the indium cluster displayed in layer 3, fig. 2.25. These are representative of the $\hat{x}$-$\hat{z}$ and $\hat{y}$-$\hat{z}$ planes, showing much more localization of indium than within the $\hat{x}$-$\hat{y}$ plane. This cluster shows more elongation along the $\hat{y}$ axis than along the $\hat{x}$ axis, indicating an ellipsoidal geometry with semi-major and semi-minor axes.

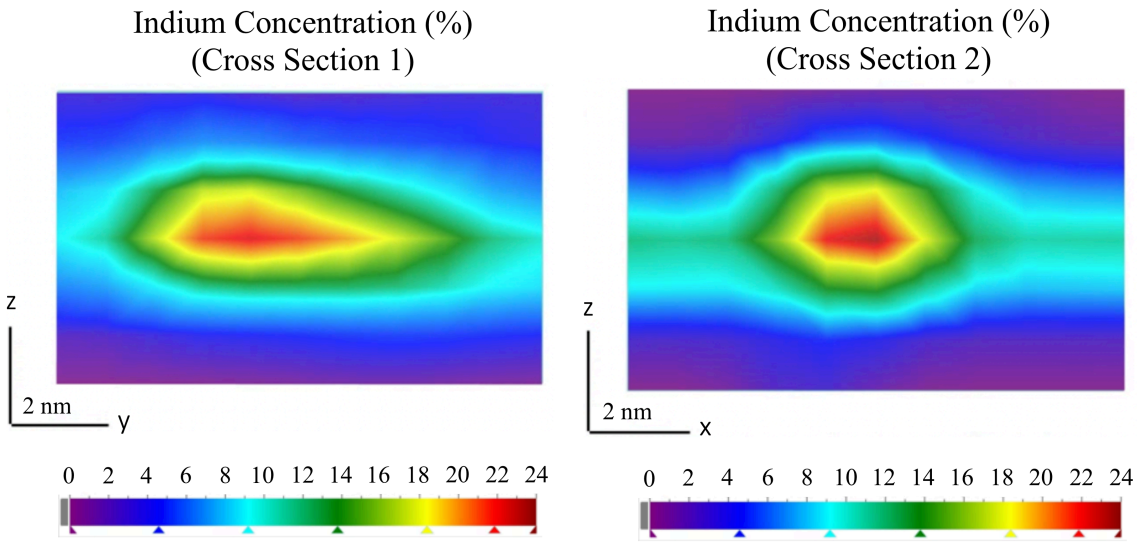

Figure 2.27 - Indium concentration of a single QD core by APT

2.14 Indium Isosurface Reconstruction

Isosurfaces are created by decomposing 3-dimensional space into a discrete grid such that all adjacent blocks containing a specified indium concentration are connected and highlighted.[50] The concentration is arbitrary and can be altered to any threshold. Additionally, a volumetric criteria must be established and realized for any isosurface to be included. The scatter plot in figure 2.28 depicts the point-cloud created by all detected ions encapsulated within the adjacent grid blocks composing 12% indium with volume > 20 nm^3 throughout all 3 quantum dot layers. The thresholds have been chosen to examine the 16 largest and most indium dense QDs, thereby avoiding any insignificant volumes.

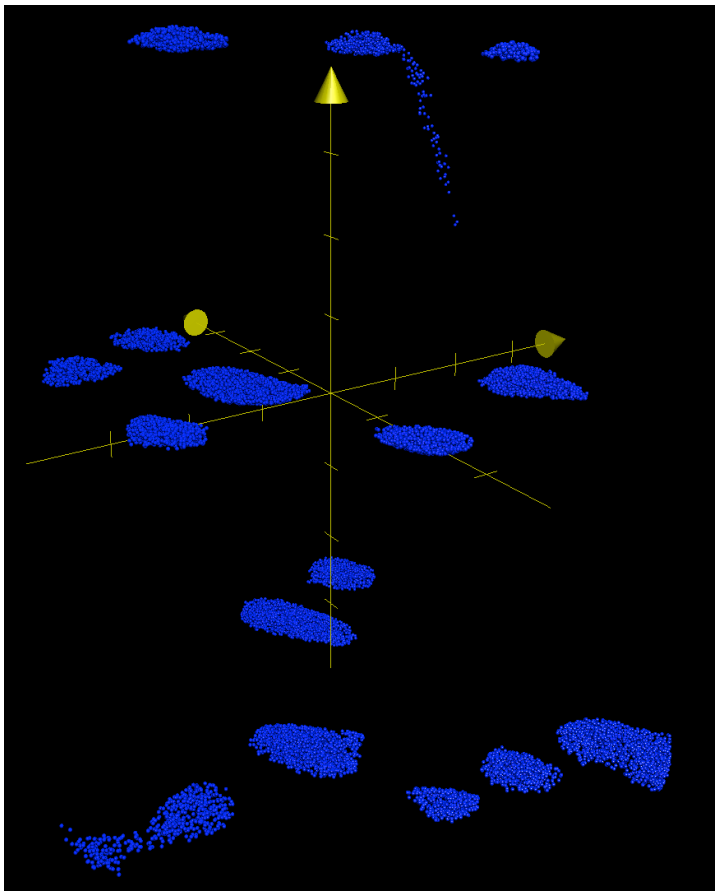

Figure 2.28 - 12% indium isosurfaces recreated using all detected ion positions (5 nm tick markings)

2.15 Proximity Histogram

A proximity histogram (proxigram) is useful to determine the indium versus gallium concentration as a function of distance from the isosurfaces displayed in fig. 2.28. The histogram has been generated based on the fraction of collected counts from the point cloud scatter data containing all isosurfaces simultaneously. A positive distance corresponds to going into the indium core from the isosurface, while a negative distance represents going outward into the surrounding GaAs matrix. The proxigram can be thought of as a series of equidistant concentric shells that encapsulates the region surrounding each isosurface. There is no assumed geometry, and the shells are used to generate a histogram based on their concentrations and positions. The zero point does not correspond exactly to 12% as there are slight deviations in histogram binning between isosurfaces. However, the binned 12% surface falls within the spatial resolution provided by the atom probe (~ 0.3-0.5 nm).

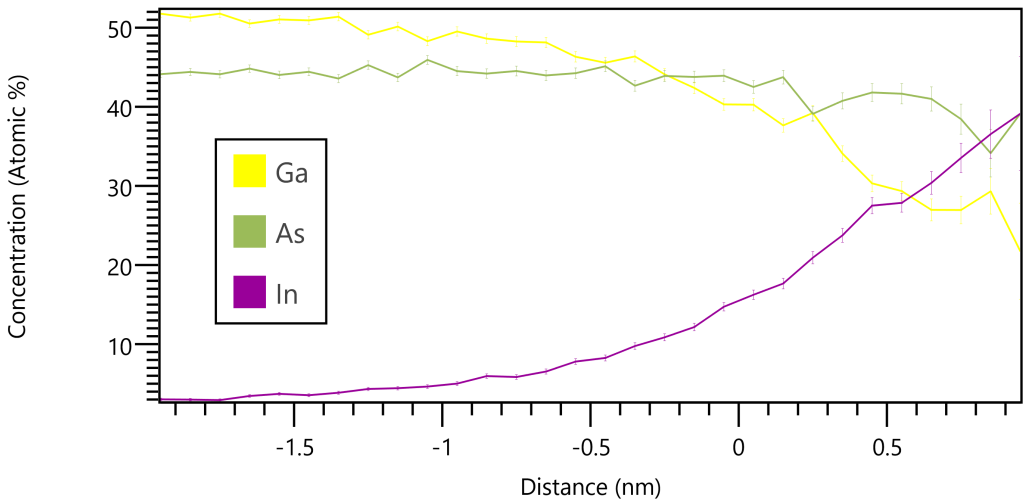

Figure 2.29 - Concentration as a function of distance from the 12% indium isosurfaces

Proxigrams are valuable tools to build quantum dot models and simulate the exciton transition energies as demonstrated in literature.[51] To simulate an exciton in a 3-dimensional well requires knowing how the potential energy varies throughout space. For the $In_xGa_{1-x}As$ system, the potential energy is a function of the indium concentration. This method drastically simplifies the process for building a potential well by creating an average shape and concentration function that fits the proximity histogram.

2.16 Ensemble Averaging Dot Dimensionality and Concentration

In this subchapter, the 12% isosurfaces in fig. 2.28 are projected onto the $\hat{x}$-$\hat{y}$, $\hat{x}$-$\hat{z}$, and $\hat{y}$-$\hat{z}$ planes. The cross sectional height for each isosurface is measured using the $\hat{x}$-$\hat{z}$ and $\hat{y}$-$\hat{z}$ projections. In the $\hat{x}$-$\hat{y}$ projection, the longest and shortest axes of each isosurface is measured to determine the semi-major and semi-minor cross sectional widths orthogonal to the growth axis. This is the point at which a physical representation of the ensemble begins to diverge from the true isosurfaces shown in fig. 2.28. This is because the isosurfaces themselves cannot be geometrically represented using traditional volumetric reconstructions. Albeit, it is a useful technique to compare to AFM and TEM.

For the purpose of this study, the tail on the upper layer quantum dot in fig. 2.28 has been excluded. The histograms in figures 2.30-2.32 demonstrate the cross-sectional height, semi-minor width, and semi-major width for all 12% indium isosurfaces after projection onto the $\hat{x}$-$\hat{z}$, $\hat{y}$-$\hat{z}$, and $\hat{x}$-$\hat{y}$ planes. To obtain the complete cross-section with respect to the pure GaAs matrix, the negative distance shown in the proxigram (fig. 2.29) must be incorporated to accommodate for shells that are < 12% indium. Each shell that is added on top of the 12% indium isosurface will add twice the shell thickness to the cross section. The shells are of $thickness = 0.1\ nm$. There is ~1.5 nm between the binned 12% indium surface and the pure GaAs matrix based on the proxigram (fig. 2.29). Therefore, there must be an additional 3 nm added to the 12% isosurface cross-sectional distributions to obtain the entire QD core from the GaAs matrix. This value is added to the mean of each distribution, while the standard deviation remains unchanged.

$$cross\text{-}sectional\ \ height \approx 4.4 \pm 0.8\ \ nm$$

$$cross\text{-}sectional\ \ semi\text{-}minor \approx 6.8 \pm 1.7\ \ nm$$

$$cross\text{-}sectional\ \ semi\text{-}major \approx 9.0 \pm 3.4\ \ nm$$

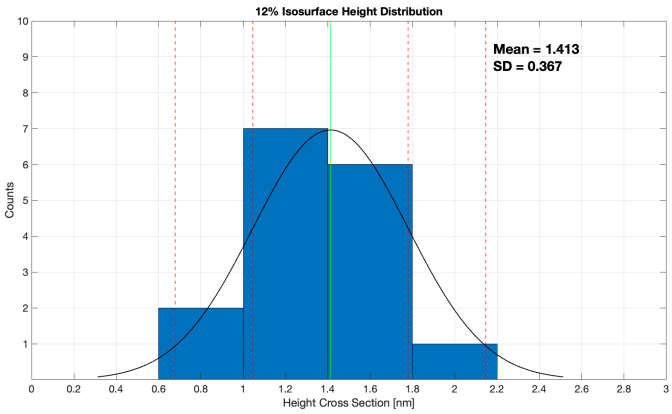

Figure 2.30 - Histogram of isosurfaces height projection

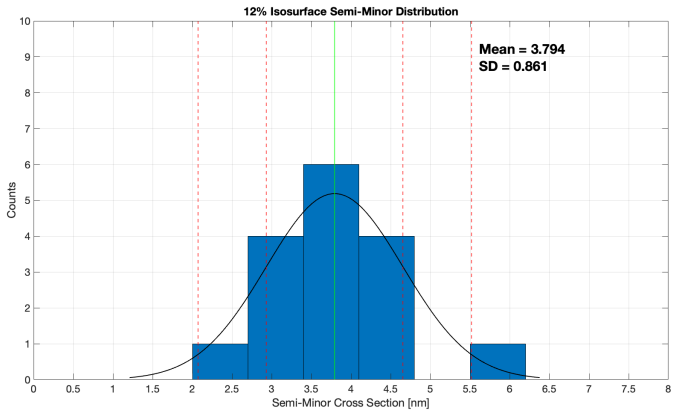

Figure 2.31 - Histogram of isosurfaces semi-minor projection

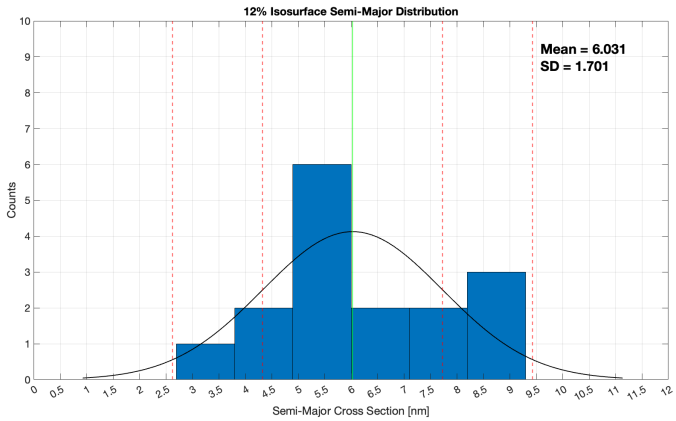

Figure 2.32 - Histogram of isosurfaces semi-major projection

Comparing to TEM ($7.2 \pm 2.1\ nm$ radial height and $8.5 \pm 6.0\ nm$ radial width), the cross-sections obtained through APT isosurface reconstruction are generally smaller with less uncertainty. Though the entire height is visible along the growth axis for both APT and TEM, only one lateral cross section is obtainable with TEM. The reason for the smaller cross-sections and uncertainty with APT is that the exact edges of the quantum dot cores can be realized in all three spatial dimensions. This allows the boundaries to be firmly established with respect to the surrounding GaAs matrix. Even though an entire ensemble of 16 quantum dots has been used for the reconstruction, it provides a double

standard deviation that is smaller than the measurement uncertainty obtained through TEM of a singular dot. The signal originating from the surrounding wetting layer in the TEM is no longer an issue for the lateral APT isosurface reconstruction. Atomic resolution HAADF was unable to determine the exact bounds of the QD height near the apex due to a lack of fineness in contrast between the atomic columns of indium and gallium. At the cluster edge, there are less indium atoms in the columns perpendicular to the growth axis when compared to the cluster core. This decreases the overall signal intensity near the bounds of the cluster. Since the TEM slice is typically much thicker than a quantum dot, there could exist multiple quantum dots in a small neighbourhood that cause distortion of the signal intensity. All of these aspects together make atom probe tomography the superior choice for assessing quantum dot size.

Comparing to AFM ($1.2 \pm 0.7\ nm$ height and $15.1 \pm 4.7\ nm$ lateral width), the cross-sectional height is larger (by $\sim 3.5\times$) since the entire height along the growth axis is realized instead of being compared to the surrounding wetting layer. Additionally, as the surface quantum dots do not have a GaAs cap above, it would be expected that they are smaller in height compared to the buried QDs. The isosurface reconstruction provides a more similar measurement than the TEM when comparing to the AFM height. Though elongation was neglected for the AFM lateral width, the semi-major cross section falls within its bounds of uncertainty while the semi-minor cross section does not. Atom probe tomography through isosurface reconstruction is a valuable tool that is an agreement with the other forms of microscopy and may be used to accurately assess QD ensemble size.

Figure 2.33 represents the isosurface reconstruction using the mean cross sectional projections. The shells correspond to 0.1 nm thickness and have been assigned concentrations based on the means of the proximity histogram. The indium concentration could instead be fitted to obtain a more smoothly varying function from the core to the outer shell, but has not been further explored as other modelling methods have been employed in the subsequent chapter. Though HAADF struggled to quantify the size of clusters, it was able to very accurately assess the core concentration.

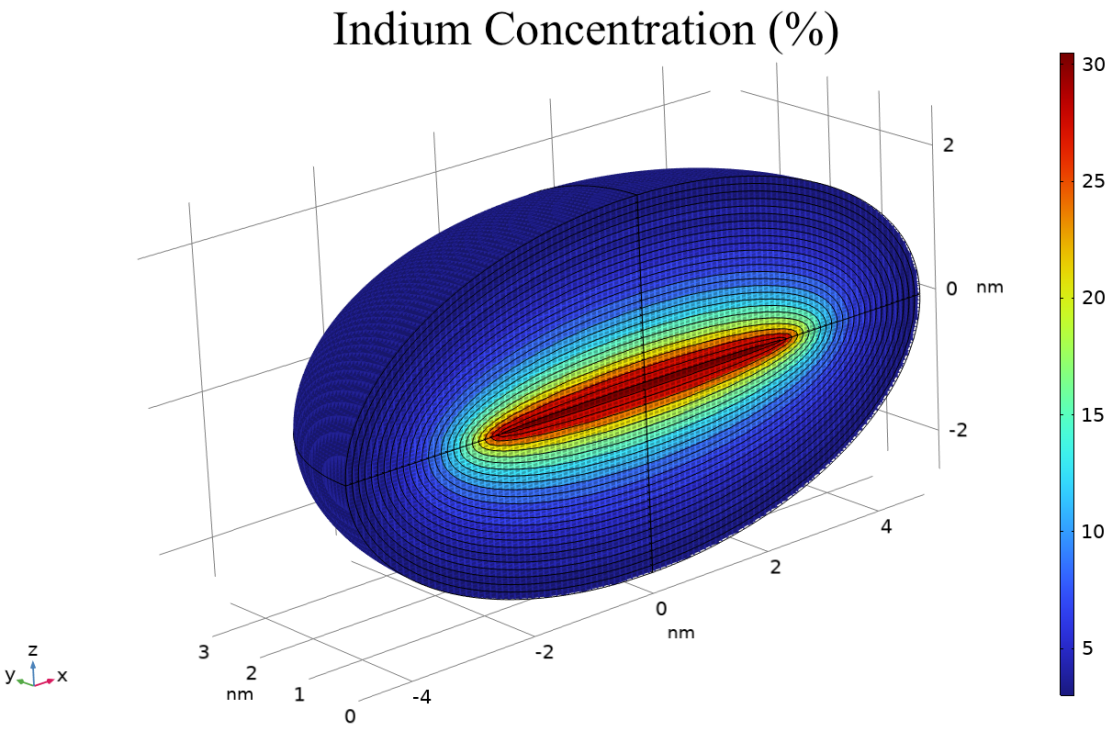

Figure 2.33 - Mean isosurface reconstruction

The exact shape and depth of the potential well, in combination with its surroundings, have profound implications on the transition energy of the exciton. This means that every aspect of a reconstruction must be precise for shape, size, concentration, and neighbouring potential landscape. Though the quantum dots have appeared highly homogeneous through means of AFM and TEM, the isosurface point cloud data shows that the clustering of indium atoms takes on a variety of shapes, some of which cannot be resolved using a simple geometric reconstruction. Furthermore, any dots that do not meet the isosurface criteria of volume and concentration are neglected, thereby limiting dot interactions with its surroundings. The beautiful 3-dimensional atom probe data opens the door to a realistic reconstruction that can accurately accomplish all of these aspects simultaneously.

Chapter 3 Model Creation

3.1 Modelling the Finite Spherical Well

In this subchapter, the bound energy eigenstates of a finite spherical well are calculated both analytically and using COMSOL software. This allows the validity of any eigenstate modelling to be established before transitioning to real-world quantum dot structures as measured with atom probe tomography. It is crucial to begin with a model that has a known analytical solution which can be referenced against using the results of the simulation to verify the accuracy of the built model. The same general principles can then be applied to the software as the transition to more complex systems takes place.

The finite spherical well is an excellent starting point. Traditional models which utilize an infinite spherical well to calculate the quantum confinement energy of the exciton are often not ideal. This is because the well is finite with variable potential barriers depending on the compositions of the quantum dot and the surrounding matrix. Any geometric shape for the finite potential well may be chosen for this step, however the choice is not imperative for the outcome of this subchapter. The only two critical aspects are (i) the existence of an exact analytical solution; and (ii) the ability to utilize principles which can be applied to larger, more complex systems.

Beginning with the derivation of the spherical finite well in Townsend[52] and Griffiths,[53] defining a particle with effective mass μ in a potential well of radius *a.*

$$V = V(r) = \begin{cases} -V_0 & r < a \\ 0 & r > a \end{cases} \tag{3.1}$$

Since the potential is only dependent on *r* and there is no time-dependence, the time-independent Schrödinger equation in spherical coordinates is

$$\left[-\frac{\hbar^2}{2\mu}\nabla^2 + V(r) \right] \Psi(r,\theta,\phi) = E\,\Psi(r,\theta,\phi) \tag{3.2}$$

where ∇^2 represents the spherical Laplacian, Ψ is the wave function, and E is the energy eigenvalue. Separation of variables is used by assuming that the solution is of the form

$$\Psi(r,\theta,\phi) = R(r)Y(\theta,\phi) \tag{3.3}$$

The function $R(r)$ is the radial component of the wave function and $Y(\theta,\phi)$ is the spherical harmonic where θ and ϕ represent the polar and azimuthal angles respectively. Substituting equation (3.3) into (3.2)[53]

$$-\frac{\hbar^2}{2\mu}\left[\frac{Y}{r^2}\frac{d}{dr}\left(r^2\frac{dR}{dr} \right) + \frac{R}{r^2 sin\theta}\frac{\partial}{\partial\theta}\left(sin\theta\frac{\partial Y}{\partial\theta} \right) + \frac{R}{r^2 sin^2\theta}\frac{\partial^2 Y}{\partial\phi^2} \right] + VRY = ERY \tag{3.4}$$

Dividing equation (3.4) by YR and multiplying by $-2\mu r^2/\hbar^2$

$$\left\{ \frac{1}{R}\frac{d}{dr}\left(r^2\frac{dR}{dr} \right) - \frac{2\mu r^2}{\hbar^2}\left[V(r) - E \right] \right\} + \frac{1}{Y}\left\{ \frac{1}{sin\theta}\frac{\partial}{\partial\theta}\left(sin\theta\frac{\partial Y}{\partial\theta} \right) + \frac{1}{sin^2\theta}\frac{\partial^2 Y}{\partial\phi^2} \right\} = 0 \tag{3.5}$$

Since the first set of curly braces only has r dependence and the second only has θ and ϕ dependence, each must be equal to a constant.[53] A separation constant can be chosen of the form $l(l+1)$, where no loss of generality occurs as l can be any complex number.[53]

$$\frac{1}{R}\frac{d}{dr}\left(r^2\frac{dR}{dr}\right) - \frac{2\mu r^2}{\hbar^2}\left[V(r) - E\right] = l(l+1) \tag{3.6}$$

$$\frac{1}{Y}\left\{\frac{1}{sin\theta}\frac{\partial}{\partial\theta}\left(sin\theta\frac{\partial Y}{\partial\theta}\right) + \frac{1}{sin^2\theta}\frac{\partial^2 Y}{\partial\phi^2}\right\} = -\,l(l+1) \tag{3.7}$$

Another separation of variables is used to solve (3.7).

$$Y(\theta,\phi) = \Theta(\theta)\Phi(\phi) \tag{3.8}$$

Multiplying both sides of equation (3.7) by $Ysin^2\theta$, plugging (3.8) into (3.7), and dividing by $\Theta\Phi$ leads to

$$\left\{\frac{1}{\Theta}\left[sin\theta\frac{d}{d\theta}\left(sin\theta\frac{d\Theta}{d\theta}\right)\right] + l(l+1)sin^2\theta\right\} + \left\{\frac{1}{\Phi}\frac{d^2\Phi}{d\phi^2}\right\} = 0 \tag{3.9}$$

As before, the first set of curly braces is dependent on only θ and the second only has ϕ dependence. Similarly, a separation constant of m^2 can be introduced.

$$\frac{1}{\Theta}\left[sin\theta\frac{d}{d\theta}\left(sin\theta\frac{d\Theta}{d\theta}\right)\right] + l(l+1)sin^2\theta = m^2 \tag{3.10}$$

$$\frac{1}{\Phi}\frac{d^2\Phi}{d\phi^2} = -\,m^2 \tag{3.11}$$

Equation (3.11) has two solutions of the form $e^{im\phi}$ and $e^{-im\phi}$, however only one exponential is necessary by allowing m to be negative and any coefficient out front can be absorbed into Θ because of equation (3.8).

$$\Phi(\phi) = e^{im\phi} \tag{3.12}$$

Since ϕ is the azimuthal angle, any 2π rotation is the same spatial position.

$$\Phi(\phi + 2\pi n) = \Phi(\phi) \tag{3.13}$$

$$e^{im\phi} = e^{im(\phi+2\pi n)} \tag{3.14}$$

This means that m must be an integer ($m \in \mathbb{Z}$), commonly known as the magnetic quantum number. Equation (3.10) has the solution

$$\Theta(\theta) = A P_l^m(cos\theta) \tag{3.15}$$

where P_l^m are the Legendre functions defined by

$$P_l^m(x) \equiv (1 - x^2)^{|m|/2}\left(\frac{d}{dx}\right)^{|m|}\frac{1}{2^l l!}\left(\frac{d}{dx}\right)^{l}(x^2 - 1)^l \tag{3.16}$$

From equation (3.16) it follows that $l \in \mathbb{Z}_{\geq_0}$ and $|m| \leq l$. For any value of l there exists $2l + 1$ possible values of m. The angular component of the wave function, $Y(\theta, \phi)$, is the same for all spherically symmetric potentials. Furthermore, the shape of the potential, $V(r)$, affects only the the radial part of the wave function, $R(r)$.[53] Using the substitution defined in (3.17) with equation (3.6) and carrying through with the differentiation leads to the radial equation.

$$R(r) = \frac{u(r)}{r} \tag{3.17}$$

$$-\frac{\hbar^2}{2\mu}\frac{d^2u}{dr^2}+\left[V(r)+\frac{\hbar^2}{2\mu}\frac{l(l+1)}{r^2}\right]u=Eu \tag{3.18}$$

This is identical to the one-dimensional time-independent Schrödinger equation with an effective potential

$$V_{eff}=V(r)+\frac{\hbar^2}{2\mu}\frac{l(l+1)}{r^2} \tag{3.19}$$

Solving equation (3.18) with $l=0$ and substituting the potential defined in equation (3.1)

$$-\frac{\hbar^2}{2\mu}\frac{d^2u}{dr^2}-V_0u=Eu \quad r<a \tag{3.20}$$

$$-\frac{\hbar^2}{2\mu}\frac{d^2u}{dr^2}=Eu \quad r>a \tag{3.21}$$

which can be rearranged to

$$\frac{d^2u}{dr^2}=-\frac{2\mu}{\hbar^2}(V_0+E)u=-k_0^2u \quad r<a \tag{3.22}$$

$$\frac{d^2u}{dr^2}=-\frac{2\mu E}{\hbar^2}u=q^2u \quad r>a \tag{3.23}$$

where

$$k_0=\sqrt{\frac{2\mu}{\hbar^2}(V_0+E)} \tag{3.24}$$

$$q=\sqrt{-\frac{2\mu E}{\hbar^2}} \tag{3.25}$$

for which q and k_0 are both real in the energy range $-V_0 < E < 0$. Following through with the solutions to these differential equations and imposing the boundary constraints on the wave function such that *u* and the first derivative are continuous, leads to the transcendental equation.[52]

$$\tan(k_0 a) = -\frac{k_0}{q} \tag{3.26}$$

Introducing another change of variables

$$k_0 a = \zeta \tag{3.27}$$

$$qa = \eta \tag{3.28}$$

Substituting (3.27) and (3.28) into the transcendental equation (3.26) leads to

$$\zeta \cot(\zeta) = -\eta \tag{3.29}$$

Squaring both sides of equation (3.27) and (3.28), then adding them together

$$(k_0^2 + q^2)a^2 = \zeta^2 + \eta^2 \tag{3.30}$$

Substituting equations (3.24) and (3.25) into (3.30)

$$\zeta^2 + \eta^2 = \frac{2\mu V_0 a^2}{\hbar^2} \equiv r_0^2 \tag{3.31}$$

r_0^2 is independent of the energy eigenvalue and is only dependent on the parameters of the problem such as the well radius, potential barrier, and the effective mass. Rearranging equations (3.31) and (3.29) leads to a solvable analytic expression for ζ given by

$$\zeta \cot(\zeta) + \sqrt{r_0^2 - \zeta^2} = 0 \tag{3.32}$$

Using equation (3.29), η can be solved for as well. Substituting equation (3.28) into (3.25) leads to the energy eigenvalue.

$$E = -\frac{\eta^2 \hbar^2}{2\mu a^2} \tag{3.33}$$

The energy eigenvalue is negative since it is with respect to the zero energy surface, which is the outside of the well. The problem is now shifted upward such that the inside of the well is the zero energy surface and the outside is a positive finite potential, the energy eigenstate becomes

$$E' = E + V_0 \tag{3.34}$$

To approximate higher order eigenstates for $l \neq 0$, the case of the potential well with barrier height $V_0 \to \infty$ is useful for comparing the energy levels to the $l = 0$ state.

$$V = V(r) = \begin{cases} 0 & r < a \\ \infty & r > a \end{cases} \tag{3.35}$$

Using equation (3.6) for the radial component of the wave function,

$$\frac{d^2R}{dr^2} + \frac{2}{r}\frac{dR}{dr} + \left[k_0^2 - \frac{l(l+1)}{r^2}\right]R = 0 \tag{3.36}$$

where k_0 is given in equation (3.24) with $V_0 = 0$. Using the substitution $\rho = k_0 r$,

$$\frac{d^2R}{d\rho^2} + \frac{2}{\rho}\frac{dR}{d\rho} + \left[1 - \frac{l(l+1)}{\rho^2}\right]R = 0 \tag{3.37}$$

(3.37) is known as the spherical Bessel equation. Solutions that do not diverge to infinity at the origin are the spherical Bessel functions.[52]

$$j_l(\rho) = (-\rho)^l \left(\frac{1}{\rho}\frac{d}{dp}\right)^l \left(\frac{\sin\rho}{\rho}\right) \tag{3.38}$$

The first four spherical Bessel functions are

$$j_0(\rho) = \frac{\sin\rho}{\rho} \tag{3.39}$$

$$j_1(\rho) = \frac{\sin\rho}{\rho^2} - \frac{\cos\rho}{\rho} \tag{3.40}$$

$$j_2(\rho) = \left(\frac{3}{\rho^3} - \frac{1}{\rho}\right)\sin\rho - \frac{3\cos\rho}{\rho^2} \tag{3.41}$$

$$j_3(\rho) = \left(\frac{15}{\rho^3} - \frac{6}{\rho}\right)\frac{\sin\rho}{\rho} - \left(\frac{15}{\rho^2} - 1\right)\frac{\cos\rho}{\rho} \tag{3.42}$$

The zeroth order Bessel function, $j_0(\rho)$, corresponds to the $l = 0$ eigenstate and has its first zero located at $\rho = \pi$. The $l = 1$ eigenstate, given by the first order Bessel function, $j_1(\rho)$, has its first zero located at $\rho \approx 4.493$. Eigenstates can be found by utilizing the square of the ratio between the zeros of the spherical Bessel functions. For example, the $n, l = 1$ eigenstate can be approximated by $\left(\frac{4.493}{\pi}\right)^2 E'$. More generally, for any principal and azimuthal quantum number, $n \in \mathbb{Z}_+$ and $l \in \mathbb{Z}_{\geq 0}$, the energy eigenvalue can be expressed as $\left(\frac{\rho \,|\, j_l(\rho) = 0}{\pi}\right)^2 E'$, corresponding to the n^{th} zero of $j_l(\rho)$.

As an example, utilizing a finite well of radius $a = 10$ nm, potential barrier $V_0 = 5$ eV, and effective mass $\mu = 0.023m_0$ leads to the energy eigenstates

$$E_{n=1,l=0} \approx 0.15 \text{ eV}$$

$$E_{n=1,l=1} \approx 0.31 \text{ eV}$$

$$E_{n=1,l=2} \approx 0.51 \text{ eV}$$

$$E_{n=2,l=0} \approx 0.61 \text{ eV}$$

$$E_{n=1,l=3} \approx 0.75 \text{ eV}$$

Since the wave function extends into the boundaries for the finite well, there will be less confinement than in the infinite well case. Therefore, for any state other than $n, l = 1,0$, the actual energy eigenvalues should be lower than the derived values as there is less confinement. Each energy eigenstate has $2l + 1$ degeneracy due to the conditions imposed on the magnetic quantum number, m, in equation (3.16). This degeneracy represents the different spatial orientations that the wave function can exhibit in 3-dimensional space.

To simulate these results in COMSOL, a model was built using an inner sphere of radius 10 nm and an outer sphere of radius 20 nm. Only the size of the inner sphere impacts the resulting eigenstates; the size of the outer sphere is not important. However, it is necessary to include the outer region as the wave function will extend into this boundary for the finite well. The wave function cannot be simulated without a modelling domain, hence the importance of the two sphere model.

Since finite element method requires boundary conditions to solve partial differential equations, this is a critical aspect for solving the Schrödinger equation in the case of the finite well. Boundary constraints are only imposed on the surface of the outer sphere. This is where modelling diverges from traditional physical boundary constraints, as typically the condition would be imposed on the interface between the inner and outer sphere and the outer sphere is assumed to be infinitely large. However in this case, the boundary constraint is imposed on the surface of the modelling domain. The solution has to adhere to this constraint as it would interact with the region outside of the model in the physical world. The boundary condition which was chosen is that the wave function is allowed to exit the modelling domain with no reflection of the outgoing waves at the boundary. This condition works well if the wave vector is orthogonal to the boundary surface, otherwise some reflection will occur.[54] For the finite spherical model, wave vectors are calculated for each finite element at the boundary surface of the outer sphere, based on their position with respect to the origin (centre of the spherical wave).

The geometry is composed of several domains which are automatically numbered based on the software's algorithm. It begins by enumerating the domain with the minimum set of coordinates. It then increments each domain with priority given to those first along the $\hat{z}$ direction, then followed by the $\hat{y}$ direction, and lastly followed by the $\hat{x}$ direction. The outer sphere is subdivided into octants, while the inner sphere contains one domain, marked 5, for a total of 9 domains overall. Domains 4 (bottom hemisphere) and 6 (top hemisphere) cannot be seen for the visual representation in figure 3.1.

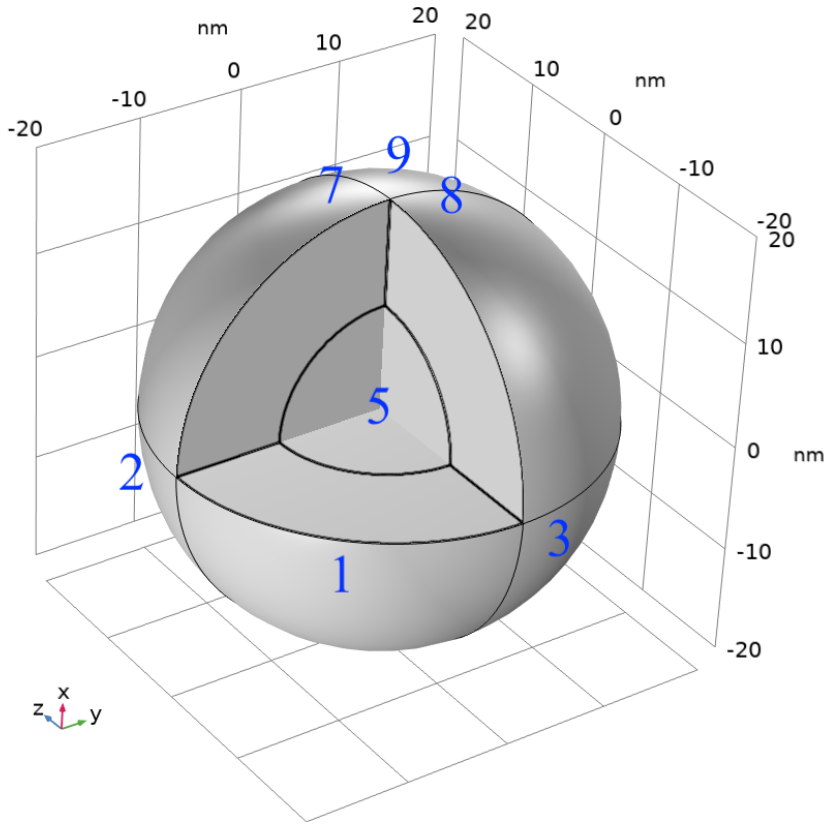

Figure 3.1 - Domain enumeration in spherical COMSOL model

Each domain is addressed through this method when assigning physical properties for the system. For example, a potential energy and effective mass is appended to the Hamiltonian for every domain. To compare the eigenenergies listed above, every domain, except the inner sphere (domain address 5), is assigned a potential energy of 5 eV, and all domains are assigned an effective mass of $\mu = 0.023m_0$. The $n = 1$, $l = 0$ eigenstate is shown below in figure 3.2.

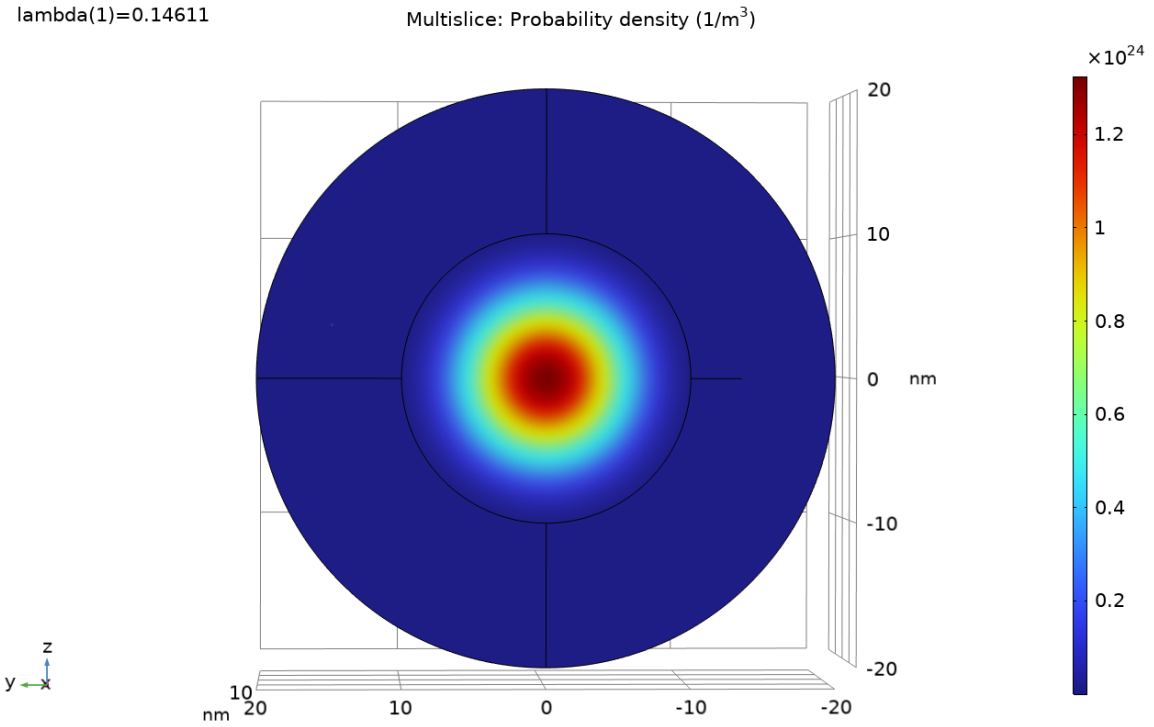

Figure 3.2 - Ground State Probability Density ($n, l = 1,0$)

The other eigenstates are included in Appendix 3. The degeneracy of eigenstates, number of nodes, and orbital shapes match the analytical expectations of the finite spherical well. The simulated eigenenergies are 2-4% lower than their analytical solutions, possibly as a result of utilizing the zeros of the spherical Bessel functions. However, differences in eigenenergies between analytical solutions and those obtained through finite element method have been documented.[55] Though infinite spherical models were used, the authors experienced a similar amount of error (1-4%), and a clear trend was observed indicating that higher order eigenstates by FEM experience more deviation from their analytical solutions than lower energy states.[55] This confirms that the modelling methods utilized by COMSOL are functioning correctly to solve eigenstates.

3.2 Finite Element Method

As seen in 3.1, COMSOL requires geometric entities to enclose any arbitrary region of 3-dimensional space, including the outside of the finite spherical well. This enclosure is known as a domain which encompasses the subset of space within its volume. Similar to other geometric entities, domains have boundaries, faces, edges, and vertices. The subset of space within the domain becomes further subdivided into a set of finite elements that are connected at nodal points and fill the entire volume of the system (every domain becomes interconnected through finite elements).[55] A set of partial differential equations are formed by the boundary value problem for each finite element which is then combined into a larger system of equations that governs the entire problem by minimizing the associated error.[55] Finite element discretization leads to the generalized eigenvalue system[56]

$$(\lambda - \lambda_0)^2 EU - (\lambda - \lambda_0)DU + KU + N_F\Lambda = 0 \tag{3.43}$$

$$NU = 0 \tag{3.44}$$

The solver evaluates E, D, K, N and N_F for the solution vector, U_0, with eigenvalue λ and linearization point λ_0.[56] E dictates whether the eigenvalue problem is linear ($E = 0$) or quadratic ($E \neq 0$). Quadratic eigenvalue problems are reformulated to linear eigenvalue problems using constraint handling to rewrite the system in the form[56]

$$Ax = \lambda Bx \tag{3.45}$$

The Schrödinger equation is a second order partial differential equation with linear dependence on the eigenvalue as depicted in equation (3.45). If the problem contains any general nonlinear dependence on the eigenvalue, such as through boundary conditions or material properties, a quadratic approximation around the eigenvalue linearization point, λ_0, is formed.[56] Linearization is useful to determine the local stability of the system as any small perturbation around the linearization point will determine if it is a stable equilibrium solution. Iteratively updating the linearization point leads to rapid convergence of the solution.[56]

3.3 Geometric Reconstruction

A spherical or ellipsoidal geometry, similar to the one used in section 3.1, would be helpful if trying to devise a simplified model depicting an average quantum dot within the ensemble. The proximity histogram would then be useful for this purpose, as it creates a statistical representation of the concentration going into the core of the quantum dot, as seen in section 2.16. Using this representation and assigning energy barriers, as demonstrated later in section 3.8, results in unbound states with $E > V_0$. Utilizing a simplified approach leads to inaccuracy as the sizes, shapes, and concentrations of the entire ensemble is averaged. Even if the quantum dots appear to be homogeneous by means of AFM and TEM, in reality they are all very unique. Indium atoms cluster differently in each quantum dot, leading to a range of energy eigenstates.

The goal of this thesis is to harness the full detail from the APT 3-dimensional composition profile to explore more realistic quantum dot bound states. It becomes justifiable to create a model that utilizes every aspect of the raw data itself, allowing for any imperfections to be incorporated as well. This helps to establish the validity of the representation, as there is no custom tailoring to obtain a desired outcome. Instead, outcomes are based solely on the raw data with no influence from the user. Using a representation of that nature also provides many interesting benefits. For example, the interaction of neighbouring quantum dots would be resolved as hybridized states are formed between them. Elongated quantum dots in a stacked structure would exhibit carrier delocalization between layers. Moreover, any complex 3-dimensional geometric arrangement is easily formed at will. In nontrivial quantum dot geometries, eigenstate wave functions and energies are sometimes deemed impossible to attain.[55]

The raw APT data itself resembles a list of 3-dimensional scatter points. As discussed in 3.2, a volumetric domain representation is necessary for the finite element method. Since scatter data is essentially a point with zero-dimensional width, it would enclose no subset of space within its bounds. This subchapter focuses on devising a strategy that connects the scatter point data to its required volumetric enclosures.

An arbitrary 3-dimensional space can be decomposed into infinitesimally small subvolumes. As the scatter data is in cartesian coordinates, it is helpful to create these subvolumes using the same basis set. For any region of $width = W$, $length = L$, and $height = H$, let dx, dy, and dz represent the respective edges of the subvolumes.

Therefore, the total region that will be modelled is a rectangular prism with dimensions $W \times L \times H$. The modelling volume is decomposed into many subvolumes of rectangular prisms with dimensions $dx \times dy \times dz$. Each individual subvolume will be referenced using the terms *domain*, *voxel*, or *cell* in the subsequent chapters. For the purpose of this thesis, $dx = dy = dz$, but each component will still be referenced explicitly to prevent loss of generality. This is because it is not necessary to use the cubic subvolume case, as each individual edge length could be altered if desired. The number of voxels that fit into each dimension are

$$n_x = \frac{W}{dx} \tag{3.46}$$

$$n_y = \frac{L}{dy} \tag{3.47}$$

$$n_z = \frac{H}{dz} \tag{3.48}$$

Domain enumeration was a key aspect toward modelling the finite spherical well in COMSOL. Therefore, each subvolume must be addressed using the same algorithm discussed in 3.1. Domain enumeration begins with the voxel containing the minimum coordinate set (circled green in fig 3.3). The assignment continues by incrementing along the z direction until the column is completed (circled orange in fig 3.3). The process is repeated for each column of the first y-z plane until reaching the end (circled blue in fig 3.3). Sequentially, each y-z plane along the x-direction follows the same numbering scheme, until the final domain is enumerated (circled red in fig 3.3).

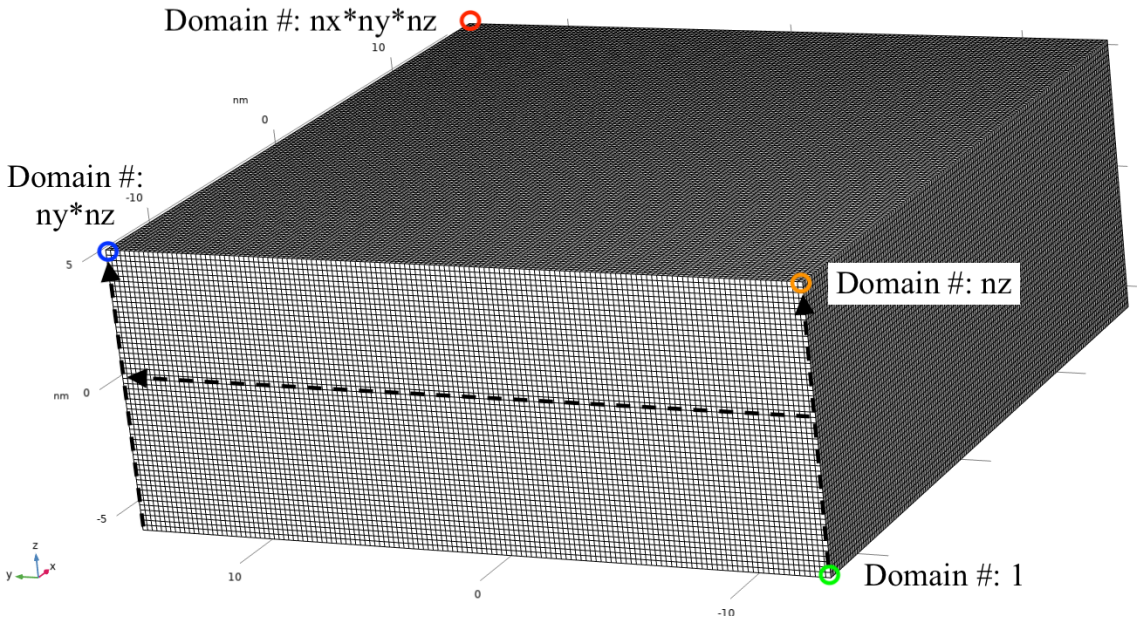

Figure 3.3 - Domain enumeration expanded

By creating a geometry of this structure, the enumeration of subvolumes into domains becomes straight forward such that the physical properties of the entire system can be decomposed for each voxel. Voxels are uniquely defined by a certain set of minimum and maximum coordinates, x_0, x_i, y_0, y_i, z_0, z_i. The spacing between these coordinates is known based on the chosen subvolume size dx, dy, and dz.

3.4 Mesh Analysis

The domains must be further subdivided into a discrete set of finite elements as discussed in 3.2, a process known as meshing. The individual voxels become composed of a set of tetrahedra using Delaunay triangulation to encompass the entire volume of space within the domain. The finite elements are connected together such that there is unity within the entirety of the structure. As a result, transitions of the physical boundary constraints between interconnected voxels becomes smoother and more precise.

Ultimately, the size of the mesh, or the number of tetrahedra that compose each voxel, did not dictate convergence to a solution. This is likely because the voxel size is already sufficiently small. Since a finite number of tetrahedra are required to fill a cubic subvolume, shrinking the voxel must also decrease the size of the tetrahedra within it. This means that using a coarser mesh results in a faster, less memory intensive solution by decreasing the number of degrees of freedom while also having negligible impact on the outcome. Meshing must be executed sequentially as the model contains too many domains to be completed altogether. The number of domains that can be meshed at once is dependent on the constraints of the computing system, dictated by the amount of physical and virtual memory.

3.5 Atom Probe Data Processing in Matlab

The raw atom probe data is in the form of a large text file containing a list of comma-separated values. Each entry in the list contains a mass-to-charge ratio that has been evaluated by the mass spectrometer, the x and y coordinates determined by the location where the signal is read on the mass spectrometer plane, along with the z coordinate which is determined by the time-of-flight from the laser pulse to the moment the ion reaches the spectrometer. The mass-to-charge ratio is then used to deduce which ions are present at a particular location in the 3-dimensional space within the sample.

The entire data set is sorted to include only a particular subset from a region of interest (ROI), while also neglecting any entry that does not contain an ion of interest. This improves the data processing efficiency as anything not needed to build the model is discarded. The ions of interest for the purpose of this study are indium and gallium, while the arsenic is neglected. To match the COMSOL geometry discussed in section 3.3, the ROI is decomposed into a 3-dimensional grid containing cubic volumetric elements, voxels, that span the entirety of the modelling domain. Each detected ion of interest is assigned to their corresponding voxel based on their position. Due to the ~80% detection efficiency of the atom probe coupled with the finite spacing of the Bravais lattice, some of the voxels may contain no ions of interest, especially if each voxel is made sufficiently small. Every voxel in the modelling region must have physical properties assigned to it as the energy barrier or effective mass associated with a null voxel is undefined.

3.6 Neighbour Searching and Spatial Resolution

Removing null voxels from the modelling domain would exclude those regions entirely from the finite element method process. As the wave function is still able to exist in those regions, this would cause a divergence between physical reality and the model. To accommodate for this shortcoming, the model instructs every voxel (including the non-null voxels) to assess its nearest neighbours and determine all nearby ions of interest.

The current voxel contains the set of coordinates ($x_0, x_i, y_0, y_i, z_0, z_i$) where the subscripts represent the voxel's minimum and maximum bounds respectively. A nearest neighbour search would expand to all voxels in the region

$$x_0 - n * dx,\ x_i + n * dx,\ y_0 - n * dy,\ y_i + n * dy,\ z_0 - n * dz,\ z_i + n * dz$$

dx, dy, and dz represent the voxel edge length and n is the number of nearest neighbours for the search. This method forms a rectangular prism (or cube since $dx = dy = dz$), that can expand if necessary and contains the current voxel at its centre. This search method encompasses all neighbouring voxels laterally, vertically, and diagonally.

If any of the voxels cannot find at least one ion of interest within a single nearest neighbour, it expands the search radius to include two nearest neighbours. This process repeats itself until at least one ion of interest is found. If multiple ions are found during the same search, they all are used to determine the current voxels concentration. The current search can then be stopped and the entire process is repeated for the next voxel. If a voxel is located on the border of the ROI, as for the faces or edges of the modelling domain, it can still search its neighbours outside the ROI utilizing the original dataset.

The aim of the following section is to obtain the highest and most uniform spatial resolution possible throughout the entire modelling domain. Spatial resolution corresponds to the smallest possible region that each voxel can resolve the APT data. Since the voxels are cubes with edge length $dx = dy = dz$, the body-diagonal of the voxel is the longest axis. The voxel size itself can be altered and made smaller or larger depending on the dx, dy, and dz parameters. The following discussion begins with a very large voxel size and slowly decreases it to analyze the associated benefits and disadvantages. The voxel size used in this thesis was determined through this process.

A very large voxel size can be used without any neighbour searching, as each voxel would contain at least one ion of interest. However, this would induce a coarse grain for the model as the transition between different domains becomes very abrupt. Since the quantum dot structures are less than 10 nm in all spatial dimensions (as described in 2.16), they would be composed of very few voxels. For example, if the voxel size was 1 nm (a reasonable size to rectify all the data with no neighbour searching), at most they would be composed of ~10 voxels laterally and ~5 voxels along the growth axis. This means that minute composition fluctuations within the quantum dot itself would be neglected. Section 2.16 only describes the 16 largest dots that were obtained through APT, therefore even smaller 12% indium isosurfaces exist in the sample region. These smaller volumes would be completely blurred by the surrounding matrix. Neighbour searching with a smaller voxel size would create a much smoother and slowly varying depiction of how the ions of interest fluctuate throughout space.

If the voxel is made to be slightly less large than just described, neighbour searching would be required as all the voxels cannot be rectified without it. If only the null voxels are chosen for neighbour searching, and since the voxel size is still relatively large, there will be a great discrepancy in spatial resolution between the null and non-null voxels. For example, a voxel size of 0.4 nm would resolve ~80% of the total number of voxels utilizing no neighbours. The remaining 20% would require a single neighbour search, thereby making the spatial resolution for the null voxels 3x worse than the non-null voxels. Assessing the ratio between the null and non-null voxels demonstrates the difference in spatial resolution, δ.

$$\delta_{non-null} = \sqrt{(dx)^2 + (\sqrt{2}dx)^2} = \sqrt{3}dx \tag{3.49}$$

$$\delta_{null} = \sqrt{(3dx)^2 + (3\sqrt{2}dx)^2} = 3\sqrt{3}dx \tag{3.50}$$

$$\therefore \frac{\delta_{null}}{\delta_{non-null}} = 3 \tag{3.51}$$

Using $dx = 0.4$ nm, $\delta_{non-null} \approx 0.7$ nm and $\delta_{null} \approx 2.1$ nm. Therefore, ~20% of the voxels will have much worse spatial resolution than the APT measurement itself.

Let $\eta_{null}(dx)$ be the percentage of null voxels that get found with a single nearest neighbour search and $\delta_{null}(dx)$ be their spatial resolution. There exists a maximum of $\eta_{null}(dx)$ as there's competitive behaviour between voxels seeking to use either 0, 1, 2, … neighbours by variation of dx. As every voxel is constrained to have at least one neighbour search, the percentage of voxels that get found using 0 neighbours, $\eta_{non-null}(dx)$, is integrated with the $\eta_{null}(dx)$ curve.

$$\eta(dx) = \eta_{non-null} + \eta_{null} \tag{3.52}$$

$$\delta(dx) = \delta_{null} \tag{3.53}$$

η and δ correspond to the overall spatial resolution and percentage of total voxels using a single neighbour search. The value that was chosen for this model is $\eta \approx 99.5\,\%$. This means that a certain dx will rectify 99.5% of the atom probe data using a single search. Any dx above this maximum results in negligible increase to η, but δ would deteriorate by equation (3.53). Since utilizing a voxel edge length of a certain size resolves vast majority of the data within a single neighbour, there becomes no added benefit (besides runtime efficiency) of using a broader size as it will only reduce the spatial resolution.

If dx was decreased below the associated maximum for η_{null}, more voxels would require two nearest neighbours. For example, the edge length used in this thesis was $dx = 0.2$ nm. If the edge length were decreased to $dx = 0.15$ nm, η would drop from ~99.5% to ~90% as those voxels would now require an expanded neighbour search. The spatial resolution can be generalized to any voxel using n neighbours.

$$\delta_n(dx) = (2n+1)\sqrt{3}dx \tag{3.54}$$

From the example above and using equation (3.54), it can be seen that the voxels using a single neighbour with $dx = 0.2\ nm$ have a better spatial resolution than the ~10% of voxels using two neighbours with $dx = 0.15\ nm$. However, the remaining 90% of voxels would have a better spatial resolution.

$$\delta_1(dx = 0.2\ nm) \approx 1.0\ nm$$

$$\delta_1(dx = 0.15\ nm) \approx 0.8\ nm$$

$$\delta_2(dx = 0.15\ nm) \approx 1.3\ nm$$

Further lowering dx would result in better spatial resolution of the single neighbour family, but the overall amount of voxels in that family would become smaller as more voxels transition to the two neighbour family. The two-neighbour family becomes better spatial resolution than $\delta_1(dx = 0.2\ nm)$ when $dx \approx 0.12\ nm$. However, at that size, the disparity in resolution between $\delta_1(dx = 0.12\ nm)$ and $\delta_2(dx = 0.12\ nm)$ is

$$\delta_2(dx = 0.12\ nm) - \delta_1(dx = 0.12\ nm) \approx 0.4\ nm.$$

This amount is significant compared to the value $\delta_1(dx = 0.12\ nm) \approx 0.6\ nm$ as well as the overall dot sizes. As a result, there would be random fluctuations in spatial resolution inside and surrounding the quantum dots. Though the effect this would have on the results has not been studied, it has been avoided in favour of using a dx that does not induce this behaviour. Additionally, a certain number of voxels would transition to the 3 neighbour family at this size, having worse spatial resolution than $\delta_1(dx = 0.2\ nm)$.

Another reason against using a smaller voxel size is due to runtime complexity. If the modelling domain is of a certain size with dimensions W, L, and H, the number of voxels that compose it can be found using equations (3.46-3.48).

$$n_{total} = n_x n_y n_z = \frac{W}{dx}\frac{L}{dy}\frac{H}{dz} \tag{3.55}$$

Letting $dx = dy = dz$, and if dx' is now used to subdivide the region such that $0 < dx' < dx$, then

$$dx' = \frac{dx}{\alpha} \quad \alpha > 1 \tag{3.56}$$

Making the substitution into equation (3.55) results in

$$n'_{total} = \alpha^3 \frac{WLH}{(dx)^3}$$

$$\therefore \frac{n'_{total}}{n_{total}} = \alpha^3 \tag{3.57}$$

For n_{total} voxels, each voxel would require searching at least n_{total} others (since it also searches itself). This is a best case scenario, as the algorithm is instructed to start the search using a single neighbour. If all voxels utilize just a single neighbour, the algorithm complexity for neighbour searching is $\mathcal{O}(n_{total}^2)$. As the radius expands to include more nearest neighbours, the search is repeated. Therefore, the more neighbours that are required for the voxel, the more times it will have to search the others. This can be generalized to a worst-case complexity time if every voxel uses at most n neighbours.

$$\mathcal{O}(n_{total}^{n+1}) \tag{3.58}$$

The runtime complexity for n'_{total} can be determined by substituting (3.57) into (3.58).

$$\mathcal{O}(n'^{n+1}_{total}) = \mathcal{O}([\alpha^3 n_{total}]^{n+1}) = \mathcal{O}(\alpha^{3(n+1)} n^{n+1}_{total})$$

The term α^{3n} cannot be discarded as the maximum number of neighbours, n, is dependent on n_{total} since they are both functions of $d\,x$. The complexity simplifies to

$$\mathcal{O}(n'^{n+1}_{total}) = \mathcal{O}(\alpha^{3n} n^{n+1}_{total}) \tag{3.59}$$

Although this particular algorithm could be made more efficient for neighbour searching, parallel computing allows this process to be done much faster by analyzing all n_{total} voxels simultaneously on multiple computer cores. Other aspects of model generation are more drastically prolonged by increasing the total number of voxels. Though COMSOL uses parallel computing for meshing the system, partitioning interconnected domains creates boundaries that imposes constraints on the mesh and increases complexity.[57]

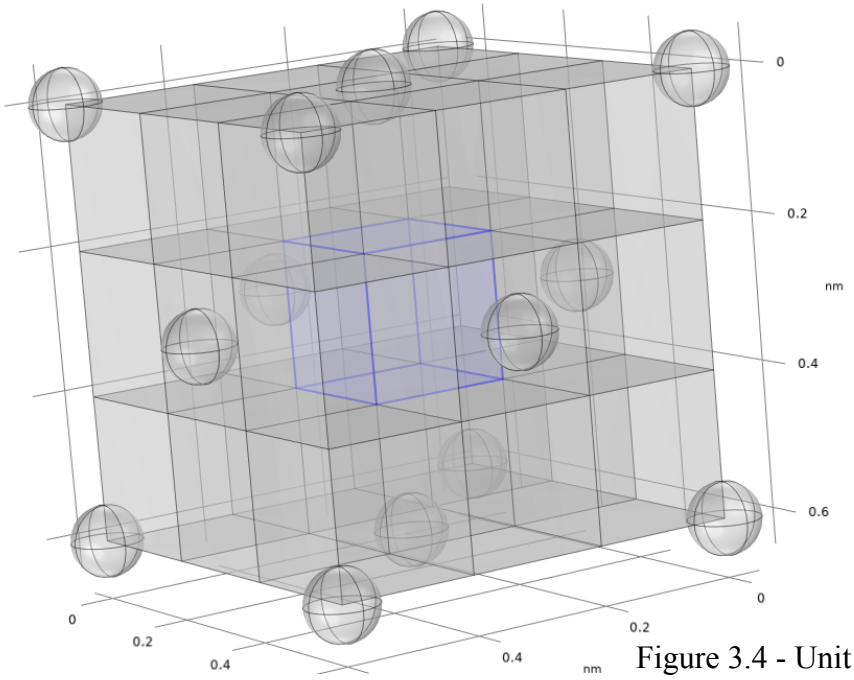

Figure 3.4 - Unit cell with centre voxel highlighted

The total number of voxels used in the subsequent chapter is $n_{total} = 1.44 \times 10^6$ with size $dx = dy = dz = 0.2\ nm$. This resolves $\eta \approx 99.5\ \%$ of the voxels with a single nearest neighbour search and has $\delta \approx 1\ nm$ spatial resolution. This corresponds to a cube with edge length 0.6 nm, which is very similar to the lattice constant of $In_xGa_{1-x}As$.

The lattice parameter will dictate the most reasonably attainable spatial resolution. One possible explanation for this occurrence is best depicted using the zincblende cubic cell in figure 3.4 where only the ions of interest have been illustrated. If a voxel is located near the centre of the unit cell, and if the voxel size is less than one-third the lattice parameter, it would be highly unlikely to find any ions of interest using a single neighbour. However, this is not limited to the centre of the unit cell, as the centre of the edges will also present the same issue as the unit cell repeats itself in all spatial dimensions. Combining this result with the APT detection efficiency of ~80%, it becomes increasingly probable that a voxel will contain no ions of interest using a single neighbour with $dx < \frac{a}{3}$, where a is the lattice parameter.

If the search radius expands to include more neighbours, it would degrade the spatial resolution of those voxels since overshoot will occur. This was depicted in the example with $\delta_1(dx = 0.2\ nm)$ and $\delta_2(dx = 0.15\ nm)$. Though, the spatial resolution would be on average better because of the $\delta_1(dx = 0.15\ nm)$ family, large fluctuations in spatial resolution and immense increases to runtime complexity make the minor average improvement to spatial resolution not worthwhile.

3.7 Voxel Concentration

One major benefit of using COMSOL for finite element analysis is that it can be easily integrated alongside Matlab. This serves the advantage of being able to perform data processing in Matlab as a means of extracting from the raw APT data, and to then also generate a complex system that requires the manipulation of ~1.44 million domains. To build a model of such magnitude would be impossible without additional software to aid in its generation. Furthermore, it allows the ROI to easily be shifted to different areas within the sample without having to rebuild the model by hand. Every voxel is addressed based on their position within the ROI using the same algorithm discussed in section 3.3 to prioritize the enumeration of geometric domains. The assigned addresses and concentrations for every voxel are used to automatically generate the COMSOL model.

Each voxel determines the concentration of indium based on the fraction of indium counts compared to the total number of ions of interest (both indium and gallium). The counts are unique to each voxel, as they are based on the voxel itself as well as its surrounding neighbours. The concentration for each voxel can only be determined after it has been populated with at least one ion of interest.

To locate a region of interest, a concentration map of the $\hat{x}$-$\hat{y}$ plane was created where $\hat{z}$ represents the growth axis. The maximum indium concentration of all voxels for a particular column along $\hat{z}$ is displayed on the $\hat{x}$-$\hat{y}$ plane for every column. This results in a 2-dimensional projection for the location of indium clusters. The same could be done for the $\hat{x}$-$\hat{z}$ and $\hat{y}$-$\hat{z}$ planes to assess the cluster height.

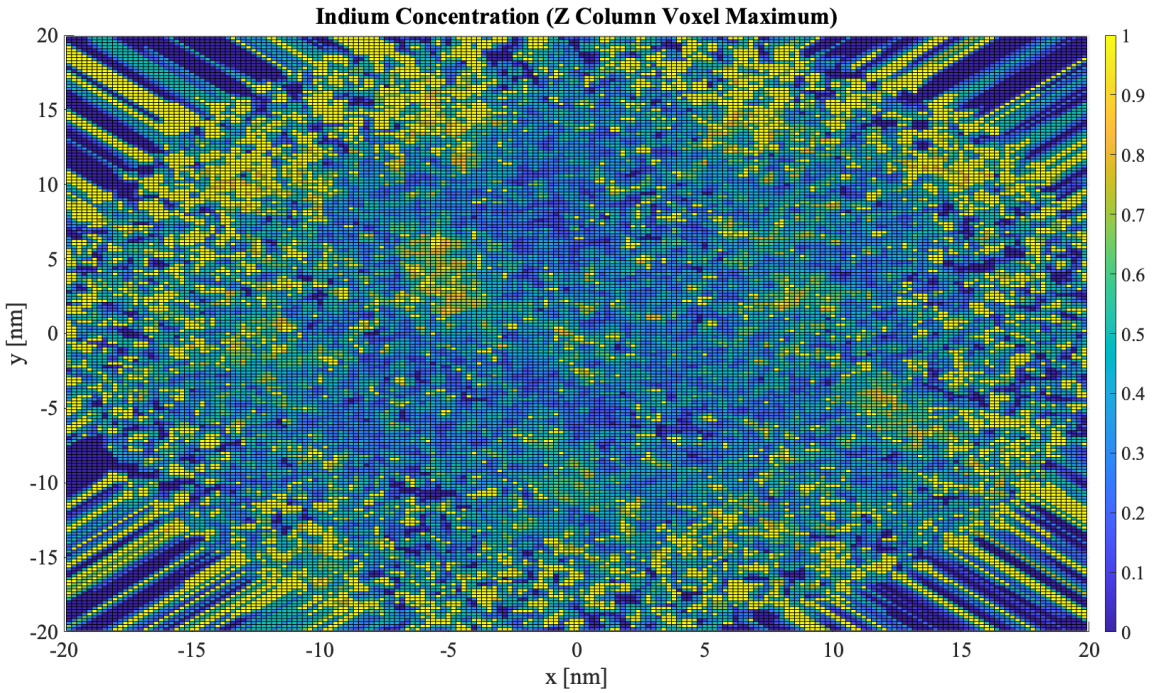

Figure 3.5 - $\hat{x}$-$\hat{y}$ plane concentration map

Figure 3.5 depicts a concentration map of the $\hat{x}$-$\hat{y}$ plane for a 40 x 40 nm wide and 10 nm thick section containing the isolated middle quantum dot layer. The streaking close to the border symbolizes regions where data is not available. Since atom probe tomography ionizes atoms along a cone aligned with the growth direction, the $\hat{x}$-$\hat{y}$ cross section is circular. The streaking is an artifact of the chosen algorithm for filling null voxels, as they converge to the same nearest neighbour along the border of the available data set. A subset of this region ($x \in [-16,16] \cup y \in [-18,18]$) is used in subsequent chapters to minimize the incorporation of null voxels on the border. Figure 3.6 is useful as a comparison for the concentration map.

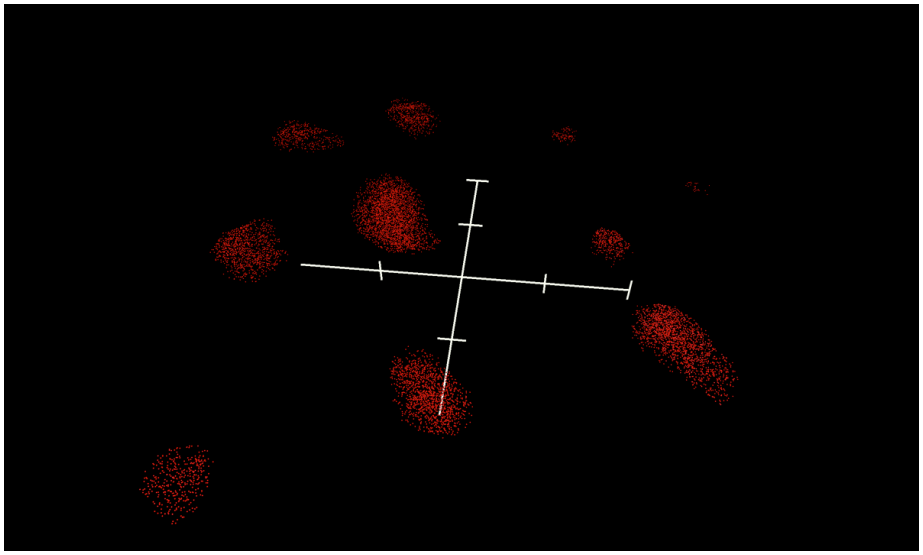

Figure 3.6 - Middle layer 12% indium isosurfaces with volume threshold lowered to 5 nm^3 (5 nm tick marks)

A value of 1 symbolizes that there exists a voxel along the column that only contains indium within its vicinity (single nearest neighbour). Therefore, some voxels are entirely composed of pure InAs or pure GaAs as the voxel size (and its search radius) has been made sufficiently small. A larger size (or search radius) would cause those voxels to smooth out into an $In_xGa_{1-x}As$ alloy.

The different nature of these two affects is realized when examining the energy band structure. $\hat{z}$ represents the growth axis, passing straight through the core of a quantum dot with the GaAs matrix on either side. For large voxels, the band structure forms a graded index where the area between the core and the surrounding matrix is an $In_xGa_{1-x}As$ alloy. Furthermore, the core would also be an alloy for sufficiently large voxels. This would affect the depth of the potential well as it would be more shallow than pure InAs. Shallow potential wells allow the carriers to tunnel further into the barriers than in a deep potential well, resulting in less confinement energy.

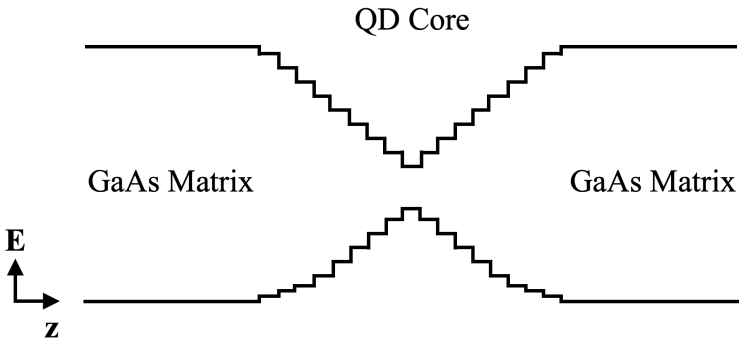

Figure 3.7 - Theoretical band structure for large voxel size

As the voxel size becomes smaller, there is an increasing probability that only one indium or gallium ion will be detected. If every voxel exhibits this binary nature, then the band structure no longer becomes a graded index as no $In_xGa_{1-x}As$ alloys are formed. The frequency of pure indium voxels increases toward the core, causing a periodic nature in the band structure, albeit with indiscernible periodicity. Though the energy barriers are tall, they are not wide since they would be of the same order as the voxel size. Carriers would easily be able to tunnel through them as their Bohr radius is 2 orders of magnitude larger than the barrier width. This would cause the carriers to become delocalized as they hop between wells.

Similar results have been demonstrated in literature through the use of digital alloys.[58] A quantum well can be sandwiched between very-short period multi-quantum wells whereby confinement is enhanced.[58] If the width of the main quantum well is larger than the width of the surrounding wells, a delocalized mini-band is formed that efficiently transports carriers to the main well.[58] Therefore, as long as there are a sufficient number of indium containing voxels that compose the main well, the eigenstate energy will be increased. Figure 3.8a and 3.8b represent two different scenarios with variation in the

main quantum well width. The width of the surrounding wells represent the width of one single voxel.

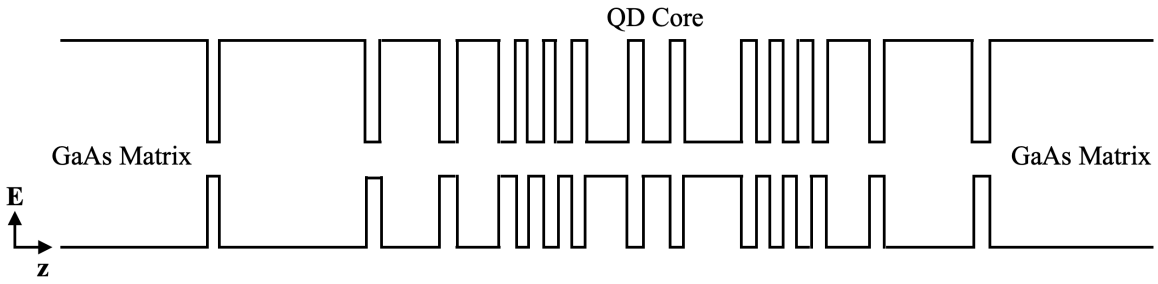

Figure 3.8a - Very small voxel band structure with small main well

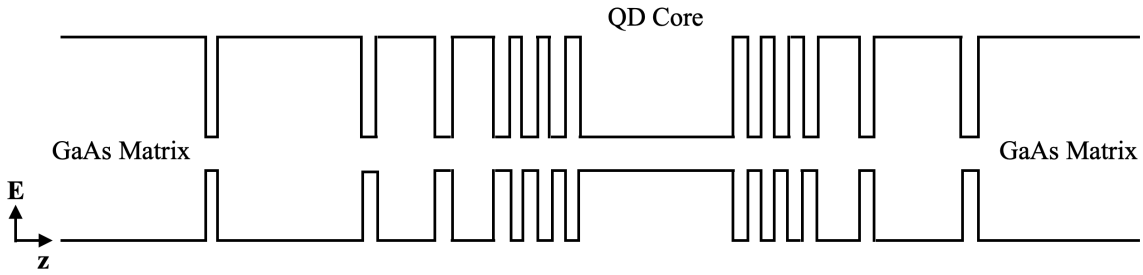

Figure 3.8b - Very small voxel band structure with large main well

Though a truly digital quantum dot was never simulated, this would agree with what was experimentally observed through means of decreasing the size of all voxels. Utilizing a single quantum dot, the ground state eigenenergy decreased by only ~3% even though the voxel size increased by 150%. This result has two important conclusions. The more “digital” alloy with reduced voxel size had higher eigenstate energy than the graded index alloy with larger voxel size. It also proved that voxel size refinements had small overall impact on the eigenstate solutions. The model utilized in this thesis lies between these two limiting cases, as some voxels are able to form alloys and other voxels form binary compounds.

3.8 Computation of Material Properties

The concentration of indium versus gallium within each voxel determines the optical properties such as the band structure, relative permittivity and the effective mass of both electrons and holes. Electron and hole barrier heights can then be assigned to each voxel based on the computed concentration of indium. The bandgap and relative band offsets as a function of concentration for $In_xGa_{1-x}As$ at low temperature can be referenced from literature.[59] For example, the fundamental gap obeys a quadratic relationship dependent on the concentration of indium.

$$E_g(x) = 1518 - 1580x + 475x^2 \quad meV \quad 0 \leq x \leq 1 \tag{3.60}$$

This function has a minimum when the concentration is unity, indicating that pure InAs has the smallest bandgap. It will become helpful to define the bottom of the conduction band and the top of the valence band as the zero energy surface, both corresponding to pure InAs. Any concentration of Ga will induce a potential barrier with a magnitude that is dependent on x.

$$E_{gmin} = 413 \ \ meV \tag{3.61}$$

Similarly, the valence band edge as a function of concentration.

$$E_v(x) = 231x - 58x^2 \quad meV \quad 0 \leq x \leq 1 \tag{3.62}$$

This function has been shifted such that the zero point is at the pure GaAs concentration. The maximum is when the concentration is unity, corresponding to pure InAs.

$$E_{vmax} = 173 \ \ meV \tag{3.63}$$

The hole barrier height with respect to the pure InAs valence band edge.

$$E_h(x) = E_{vmax} - E_v(x) \tag{3.64}$$

The electron barrier height with respect to the pure InAs conduction band edge.

$$E_c(x) = E_g(x) - E_{gmin} - E_h(x) \tag{3.65}$$

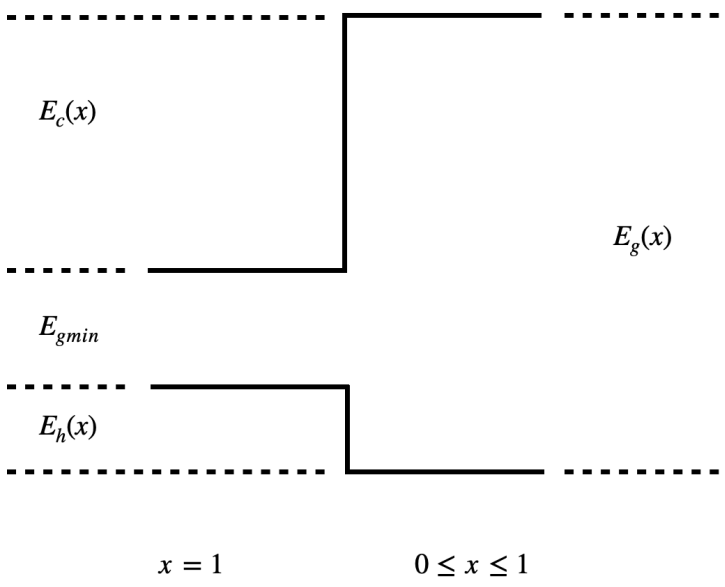

Figure 3.9 - Band diagram for determining energy barriers

The electron effective mass can also be derived based on the concentration,[59] where m_0 is the free electron mass.

$$m_e(x) = \left[0.0667 - 0.0419x - 0.00254x^2\right] m_0 \tag{3.66}$$

Since the heavy hole has a much larger effective density of states than the light hole, the heavy hole effective mass is utilized by the model. There may be some coupling between the light hole and heavy hole states,[59] however this has been neglected for the purpose of

the simulation. The heavy hole effective mass as a function of the indium concentration is given by,[60]

$$m_{hh}(x) = \left[0.34 + 0.0013x\right]m_0 \tag{3.67}$$

The static relative permittivity as a function of the indium concentration is,[60]

$$\epsilon_r(x) = 12.4 + 2.15x \tag{3.68}$$

All of these values correspond to the physical parameters of the material system at a temperature below 10K. Strain has been neglected for this model.

3.9 Potential Energy Landscape

The same middle quantum dot layer is shown in figure 3.10 after assigning electron barrier heights to each voxel. A cross section has been taken along the planes that intersect one of the indium clusters. The emphasized blue region depicts the same cluster that is located at $(x, y) \approx (-5, 5)\ nm$ in figure 3.5.

These visualization techniques aid in the understanding of various composition fluctuations and sizes of quantum dots within the layer and their surrounding. The indium signal in the GaAs matrix could either be due to As_3^{2+} incorporation (as described in 2.10) or indium diffusion along the growth axis as no indium flushing step was performed during growth. This process consists of raising the substrate temperature to above ~540°C as the sticking coefficient for indium falls rapidly to zero;[61] a useful technique for preventing indium incorporation in the GaAs spacer between quantum dot layers.

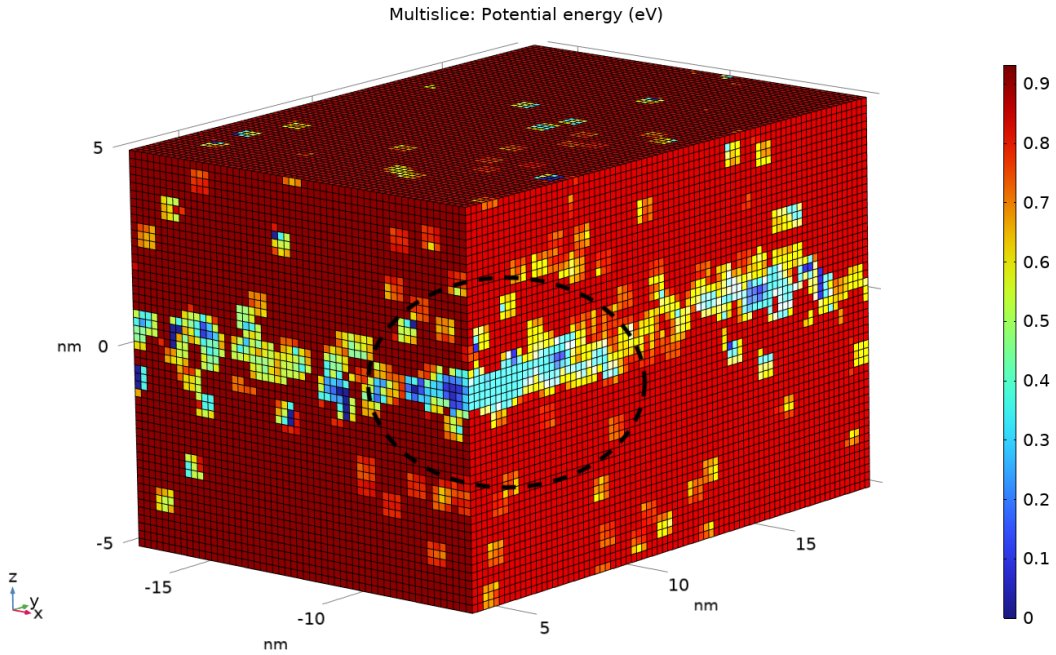

Figure 3.10 - Middle QD layer potential energy

Appendix 4 contains plots that are similar to figure 3.5, however now the electron barrier heights have been assigned to each voxel based on the indium concentration. Additionally, figure 3.5 utilized the maximum voxel value along each $\hat{z}$ column, whereas the exact voxel value is displayed in Appendix 4. These plots show the entire $\hat{x}$-$\hat{y}$ plane that is used for the modelling domain (32 x 36 nm), with a thickness of 0.2 nm (1 voxel). Utilizing these sizes for the sections, the z-coordinate is swept over the span of 4 nm from above the quantum dot layer to just below it. The step size is 0.4 nm (2 voxels) to show how the electron barrier heights change with depth into the QD layer. Indium clusters are not situated at the exact same height along the growth axis, but are roughly separated by 1-2 nm. This could either be a result of quantum dot nucleation on separate terraces or sample misalignment during the growth or atom probe evaporation.

Chapter 4 Eigenstate Solutions

4.1 Photoluminescence Spectra

This chapter begins by assessing the photoluminescence emission spectra of the quantum dot ensemble at 7.7 K. This value becomes very useful to compare to the calculated eigenstate energies in the subsequent sections, as the emission is representative of the true transition energy of the exciton. The sample has been excited with an Argon ion laser at 488 nm wavelength. The main peak in figure 4.1 corresponds to the quantum dot emission, while the smaller peak is from the surrounding GaAs matrix.

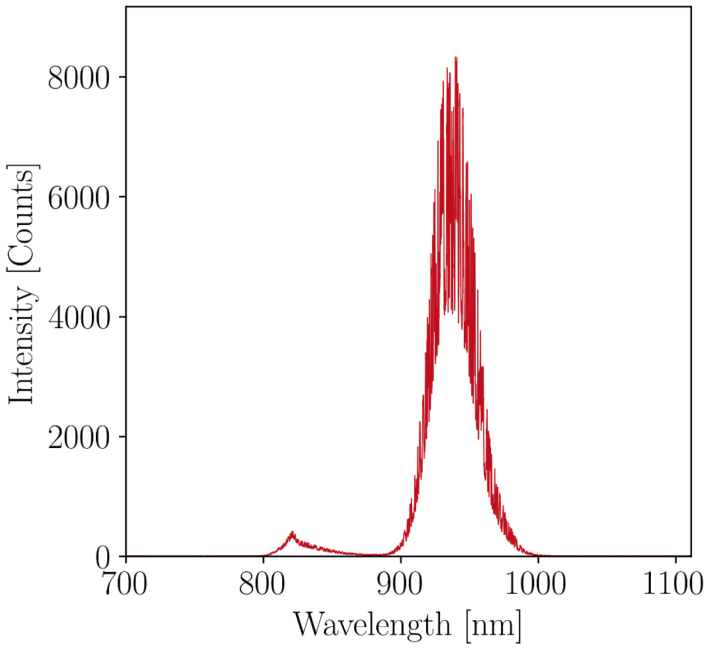

Figure 4.1 - PL emission spectra at 7.7 K

The smaller peak has been magnified in figure 4.2. The FWHM has been used to calculate the standard deviation assuming a Gaussian distribution.[62]

$$\sigma = \frac{FWHM}{2\sqrt{2\ln 2}} \tag{4.1}$$

Therefore, the emission peak is at a wavelength of $820 \pm 10\ nm$. The direct bandgap of GaAs as a function of temperature is[63]

$$E_g(T) = 1.522 - 5.8 \times 10^{-4}\left(\frac{T^2}{T+300}\right)\ eV \tag{4.2}$$

$$E_g(T = 7.7\ K) \approx 1.52\ eV$$

The energy is related to the photon wavelength by

$$E = \frac{hc}{\lambda} \tag{4.3}$$

Substituting the appropriate values for the speed of light and Planck's constant results in a wavelength that is within the uncertainty provided by the measurement.

$$\lambda \approx 816\ nm$$

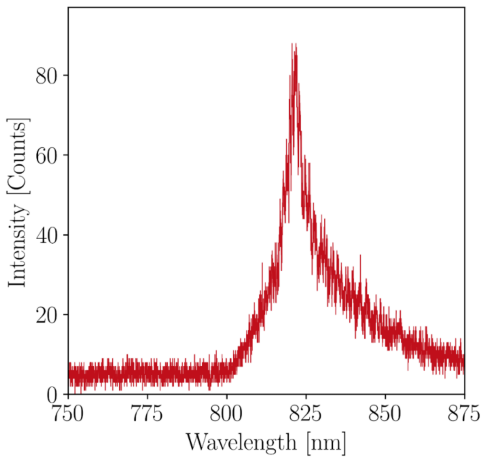

Figure 4.2 - PL emission spectrum of GaAs at 7.7 K

The larger peak of the quantum dot emission is magnified in figure 4.3. Using the same method of assessing the FWHM to calculate the standard deviation in equation (4.1), the emission wavelength is $940 \pm 30\ nm$.

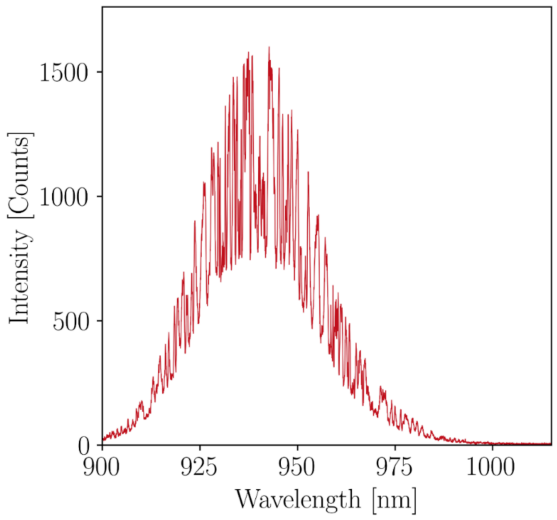

Figure 4.3 - PL emission spectrum of QDs at 7.7 K

Converting this wavelength to energy using equation (4.3), the transition energy of the exciton is

$$E_{exciton} \approx 1.32 \pm 0.04\ eV$$

4.2 Eigenenergies of the Ensemble

A total of 10 bound eigenstates ($E < V_0$) were found in the isolated middle layer using the APT model devised in this thesis. The subsequent subchapters will examine the eigenenergies and wave functions of these bound states. Some of the wave functions exist near the boundary of the available data set, indicating that they may become unbound if the potential energy landscape outside the available data set allows them to leave the modelling domain. This is because many of the quantum dots obtained in the APT sample region exist near the boundary since the quantum dot density is high and the sample region is comparatively small. In figure 3.6, all of the isosurfaces furthest away from the origin represent quantum dots that exist on the boundary of the modelling domain. However, their eigenenergies are very similar to eigenstates that are fully encapsulated within the modelling domain. As such, all 10 eigenstates have been used to determine the band-band transition energy of the exciton.

The plots in this chapter reference the eigenenergy in relation to the zero energy surface, which would be the pure InAs conduction/valence band edge. To obtain the transition energy, the eigenstates must be added to the bandgap minimum discussed in equation (3.61). E_e and E_h represent the mean eigenstate energy of the electron and hole. Therefore, the simulated transition energy is

$$E_{simulated} = E_e + E_h + E_{gmin} \tag{4.4}$$

$$E_{simulated} = 1.45 \pm 0.04\ eV$$

The mean and standard deviation have been calculated using the entire ensemble of eigenstates. Interestingly, the standard deviation is the same as observed through photoluminescence spectroscopy. Therefore, this is a very useful technique in order to assess the distribution of eigenenergies that would cause the emission spectrum to broaden. The mean energy is blue shifted from the PL data for reasons that will be discussed in section 4.4. At room and cold temperatures, the thermal energy is

$$E_{thermal}(T = 300\ K) = kT \approx 26\ meV$$

$$E_{thermal}(T = 7.7\ K) = kT \approx 1\ meV$$

The deepest electron and hole state with the lowest eigenenergies are

$$E_e' \approx 848\ meV$$

$$E_h' \approx 158\ meV$$

The largest energy barriers for the electron and hole are when $x = 0$ in equations (3.64) and (3.65), representing the pure GaAs band edge. The difference in energy between these states and the GaAs band edge is

$$\Delta E_e = E_c(x = 0) - E_e' = 84\ meV \tag{4.5}$$

$$\Delta E_h = E_h(x = 0) - E_h' = 15\ meV \tag{4.6}$$

The sample had no photoluminescence emission at room temperature, which is uncommon for sufficiently small and dense InAs/GaAs quantum dots that are not drastically dislocated. Dislocations in this system typically occur as a result of excessive strain in the lattice due to over deposition of indium. Normally InAs/GaAs quantum dots are made larger by raising indium deposition or increasing growth temperature, thereby decreasing the QD density and redshifting the emission wavelength closer toward 1.3 μm. Reaching a 1.3 μm wavelength emission generally cannot be accomplished without additional use of strain reduction layers to further redshift the transition energy of the exciton. This would increase ΔE_e and ΔE_h as the lowest energy states become deeper with respect to the surrounding GaAs band edge since the transition energy is lowered. However, in the grown sample $\Delta E_h < E_{thermal}(300\ K)$, this allows holes to effectively escape the quantum dots through nonlocal Auger recombination (see section 1.3). Electron eigenstates are deeper than hole eigenstates and are not as affected by thermal energy since $\Delta E_e > E_{thermal}(300\ K)$. At cold temperatures, neither carrier is affected by the thermal energy and the exciton can effectively recombine without carrier escape into the surrounding reservoir as they are contained within the quantum dot energy states.

4.3 Eigenstate Wave Functions

The wave functions form a complex and intriguing arrangement of hybridized states. There exists bonding and anti-bonding between neighbouring quantum dot molecular orbitals. The bonding states have lower energy than the anti-bonding states and the anti-bonding states contain node lines between orbitals. There also exists a near degenerate state with eigenenergies that are within 2 meV of one another, experiencing very similar orbital patterns.

The location of quantum dots given by the isosurfaces in figure 3.6 is very helpful for interpreting the probability density solutions that were obtained through the simulation. Refer to figure 3.6 to assess the orbitals of the eigenstate solutions against the location of indium clusters. The indium clusters can also be seen in Appendix 4, presenting the same orientation and layout as the eigenstate solutions shown in this chapter. Though the solutions are inherently three-dimensional and can be visualized in any means, a 2-dimensional $\hat{x}$-$\hat{y}$ cross-section is used for clarity and comparison. In figures 4.8 and 4.9, the entire wave function cannot be shown altogether since the orbitals exist at slightly different elevations along $\hat{z}$.

At the boundaries of the exterior modelling domain, a wave vector is calculated for each finite element using its potential energy, effective mass, and energy eigenvalue. Continuity is assumed such that the wave function only contains a normal component to the exterior boundary surface. This determines the rate of decay for the exiting plane wave at each exterior boundary finite element.

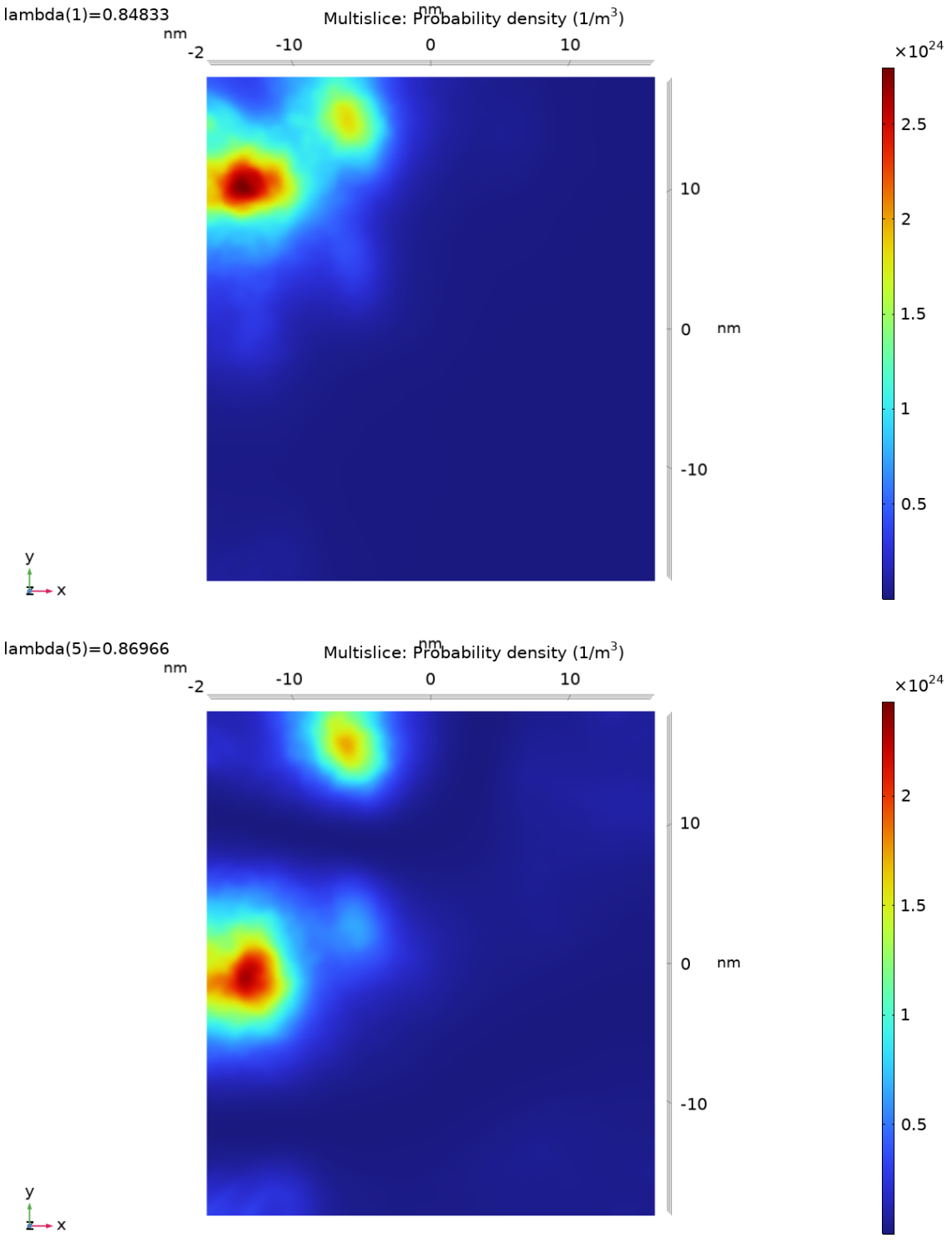

Figure 4.4 - Electron Bonding and Anti-Bonding States

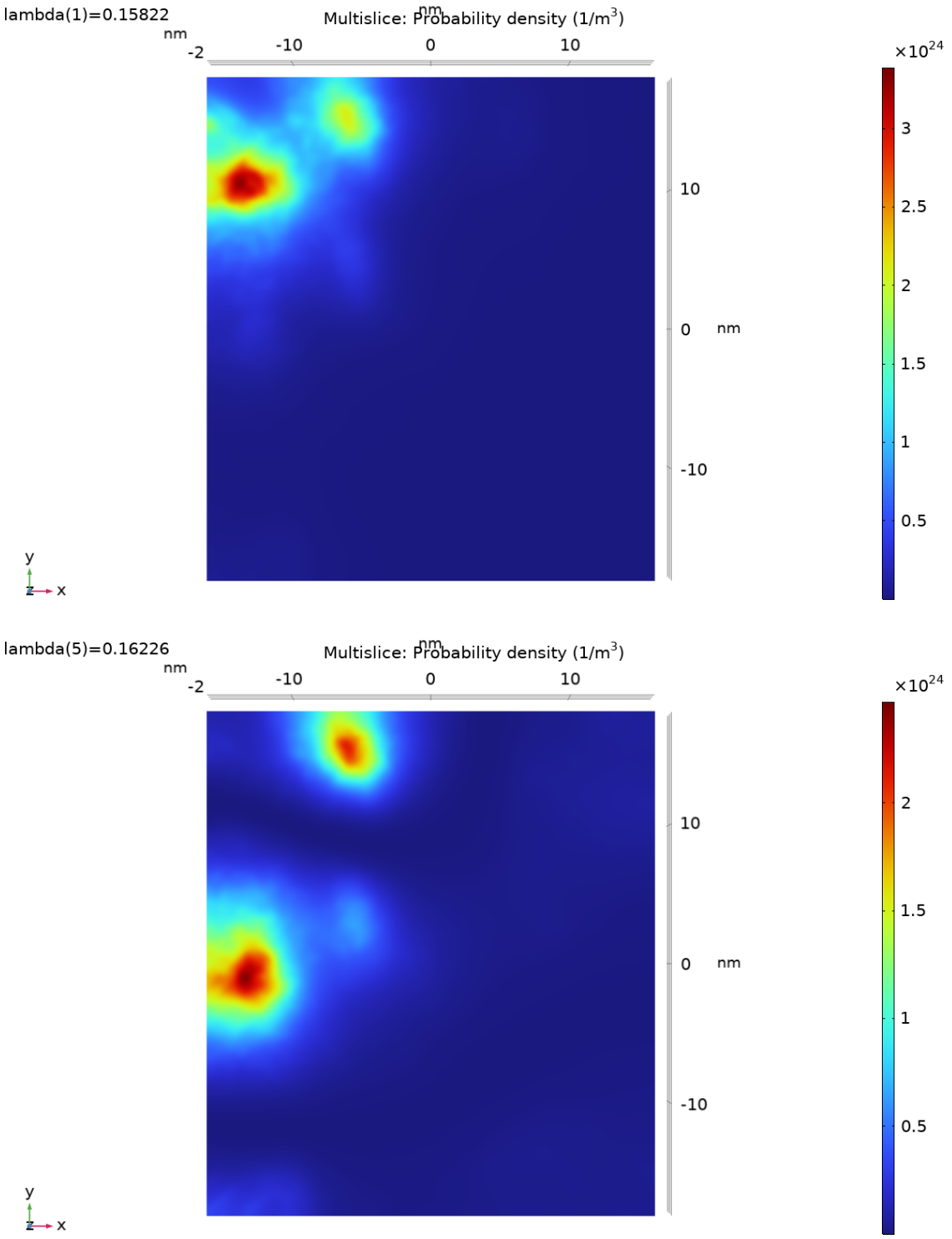

Figure 4.5 - Hole Bonding and Anti-Bonding States

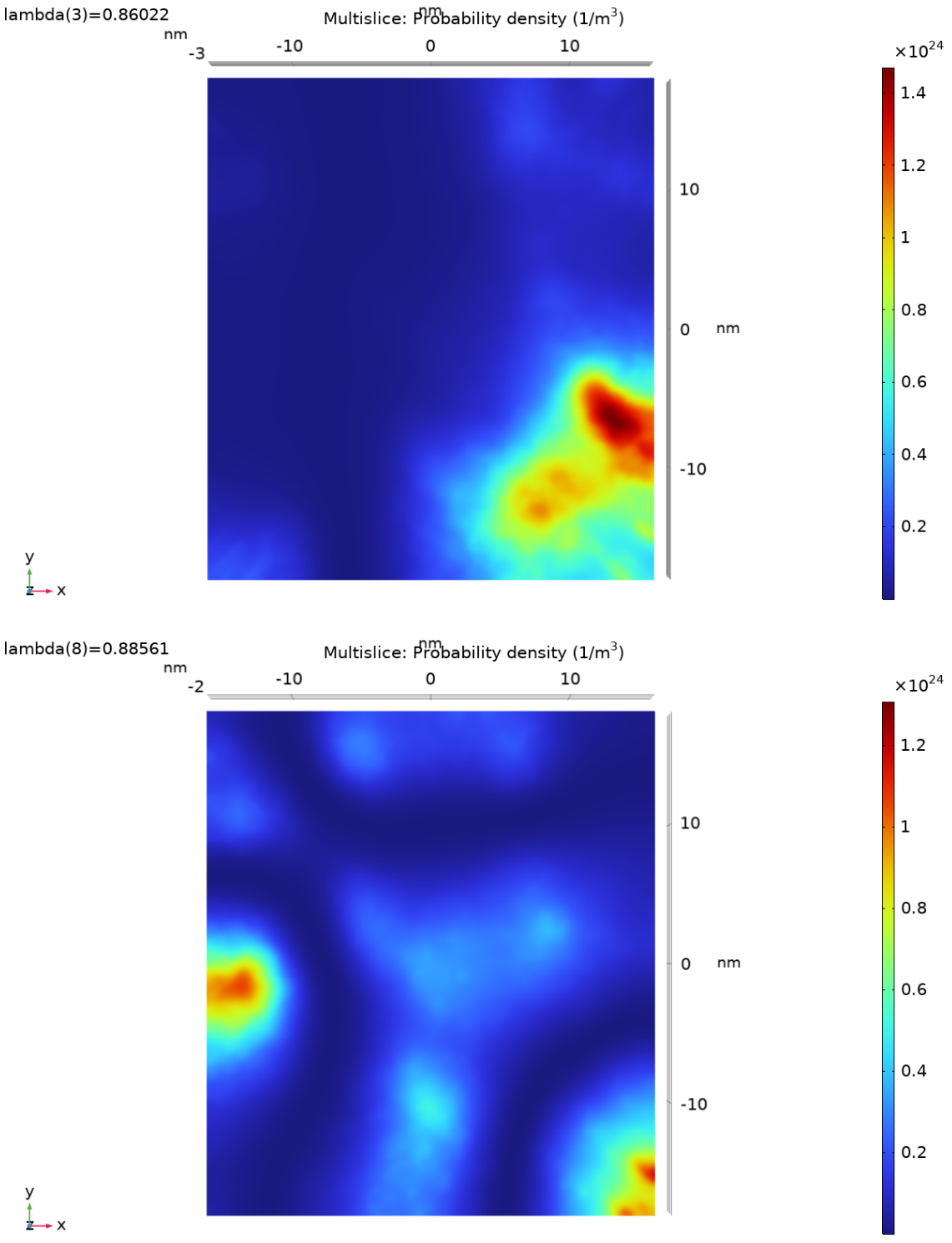

Figure 4.6 - Electron Bonding and Anti-Bonding States

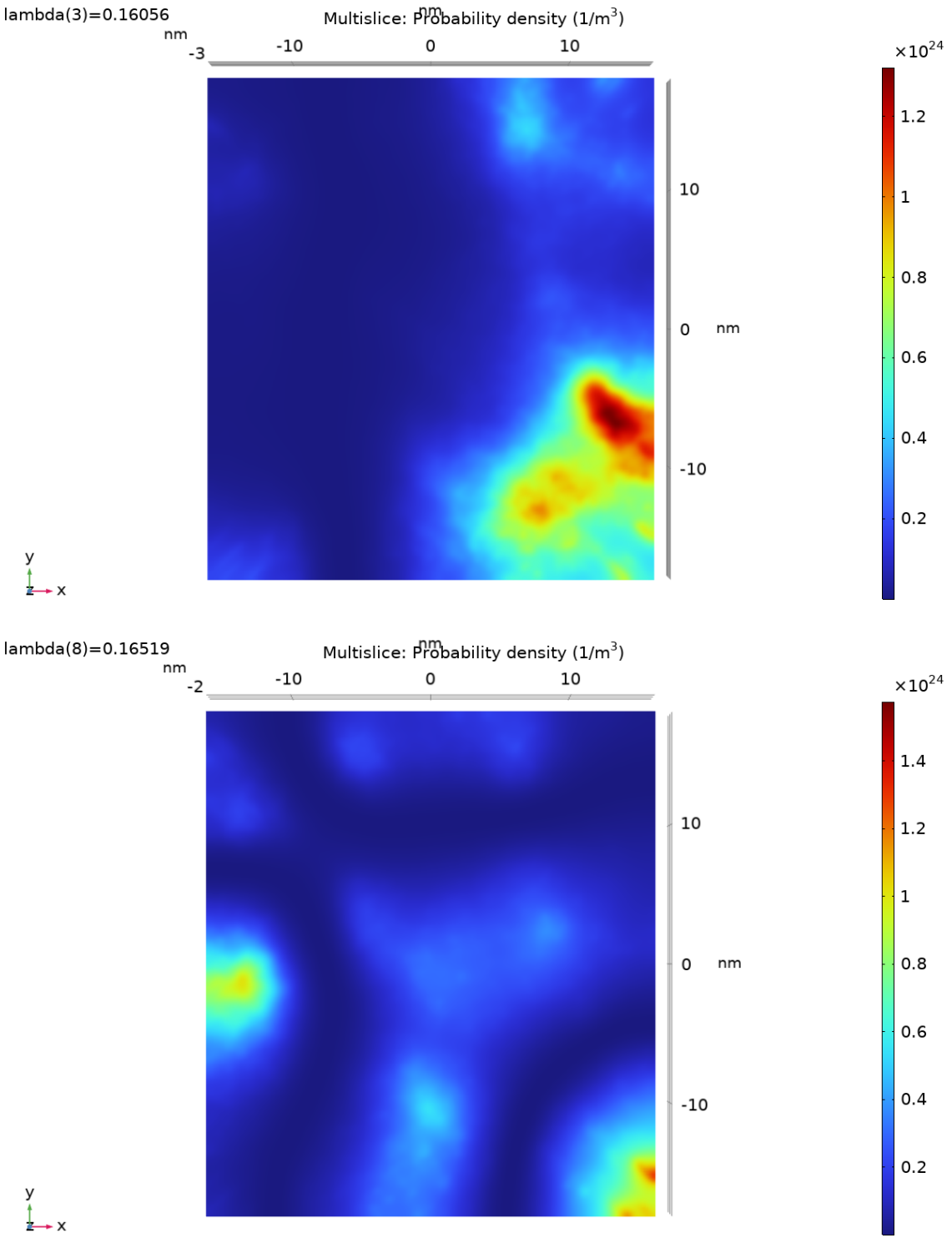

Figure 4.7 - Hole Bonding and Anti-Bonding States

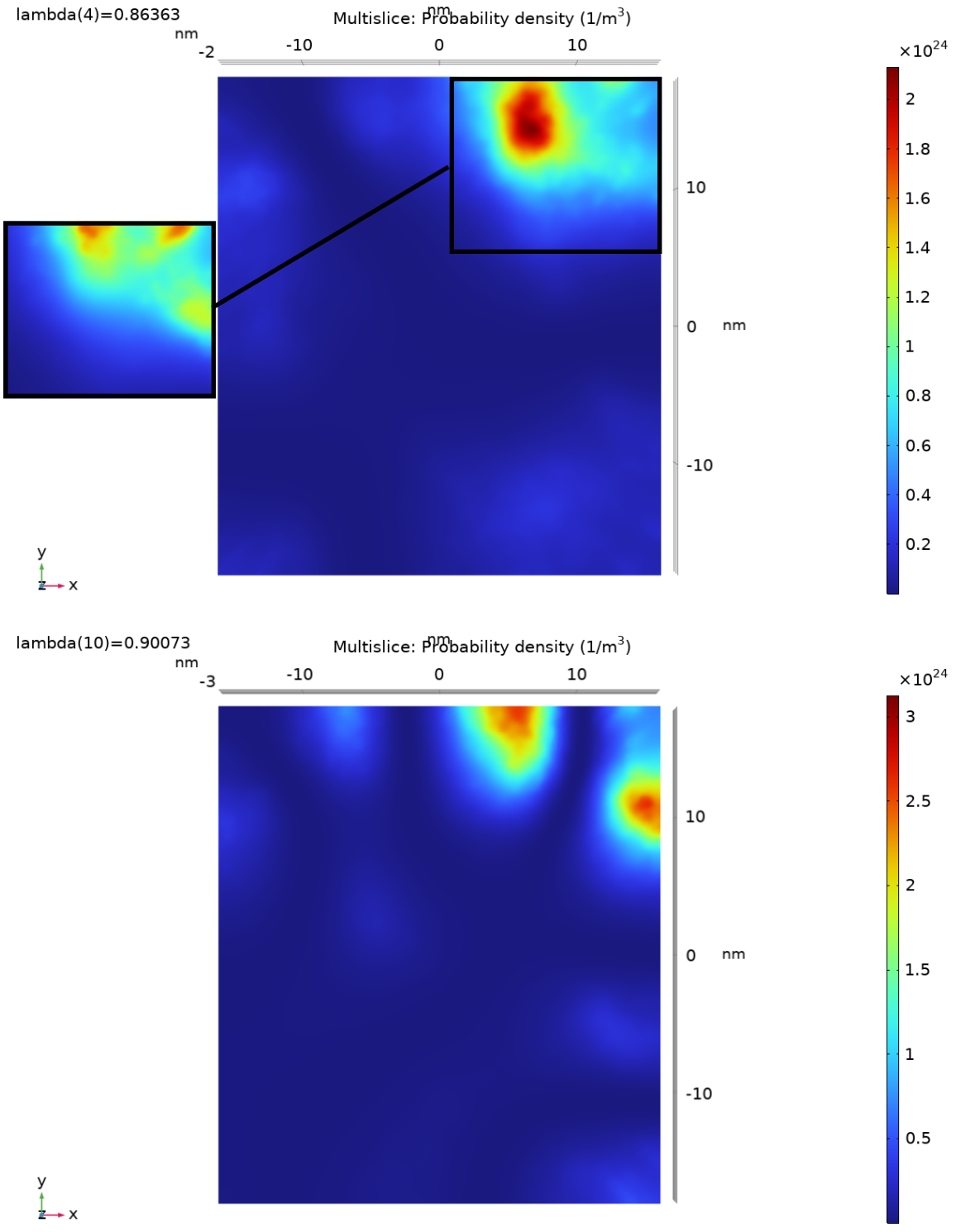

Figure 4.8 - Electron Bonding and Anti-Bonding States
(lower cross section shown)

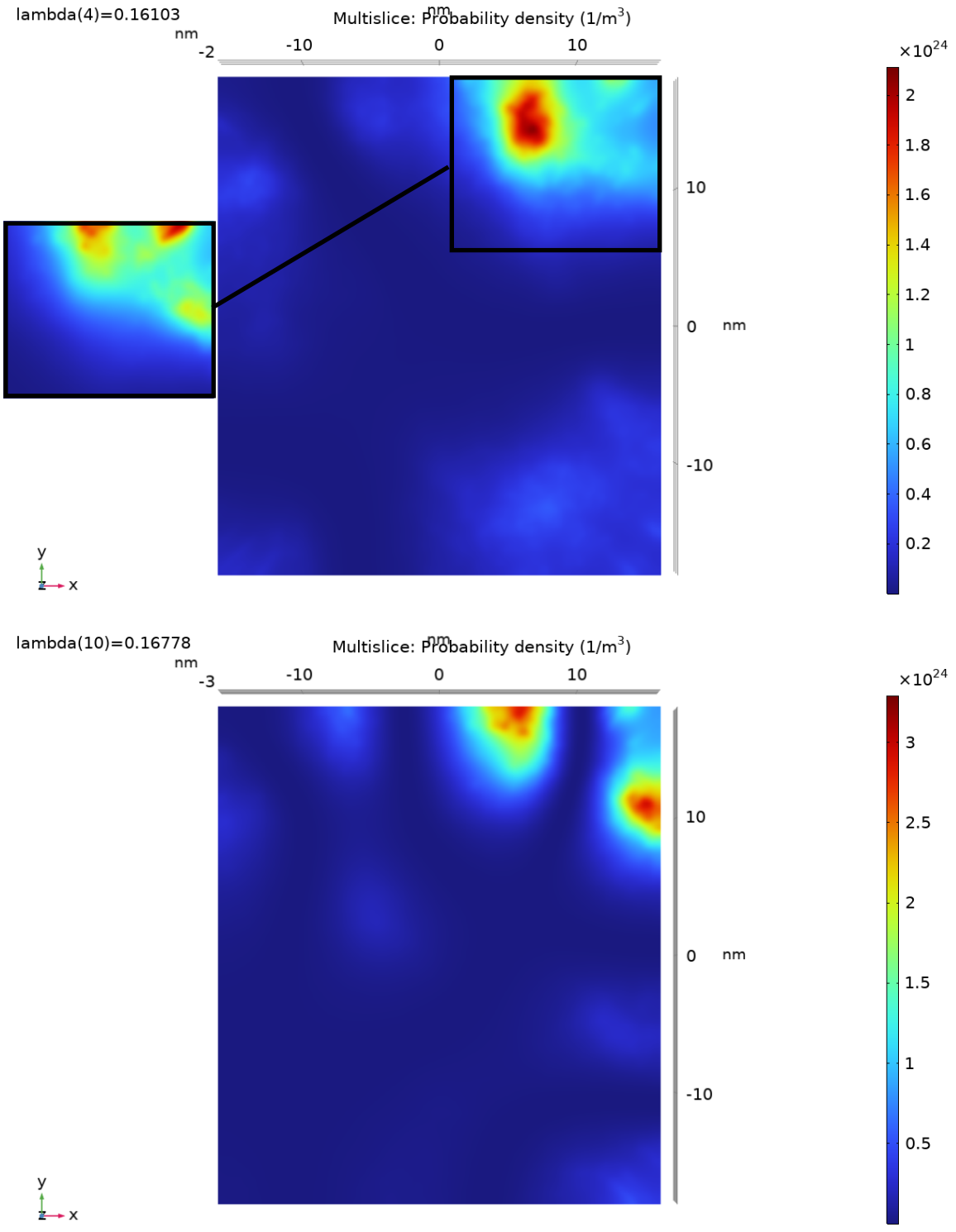

Figure 4.9 - Hole Bonding and Anti-Bonding States
(lower cross section shown)

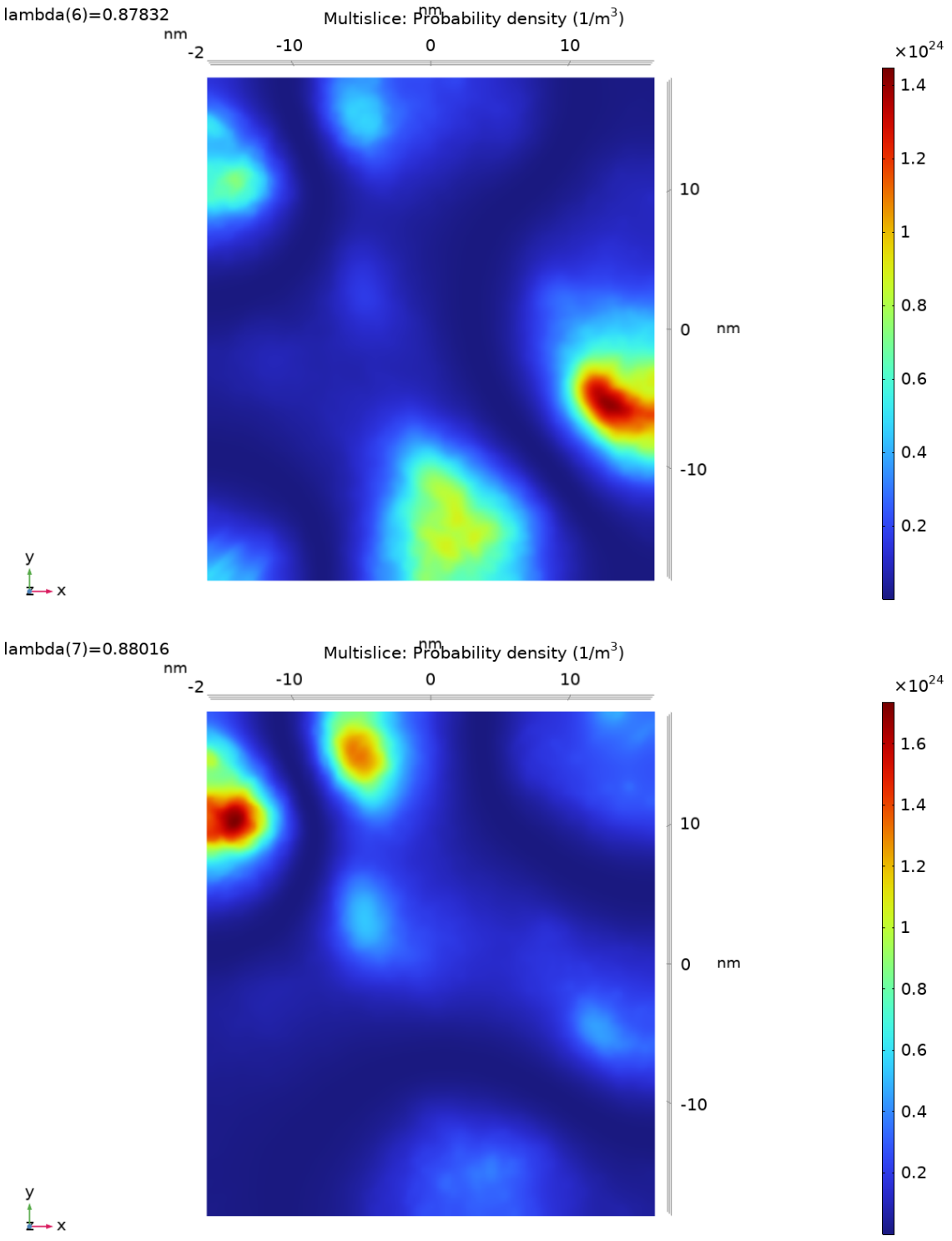

Figure 4.10 - Degenerate Electron States

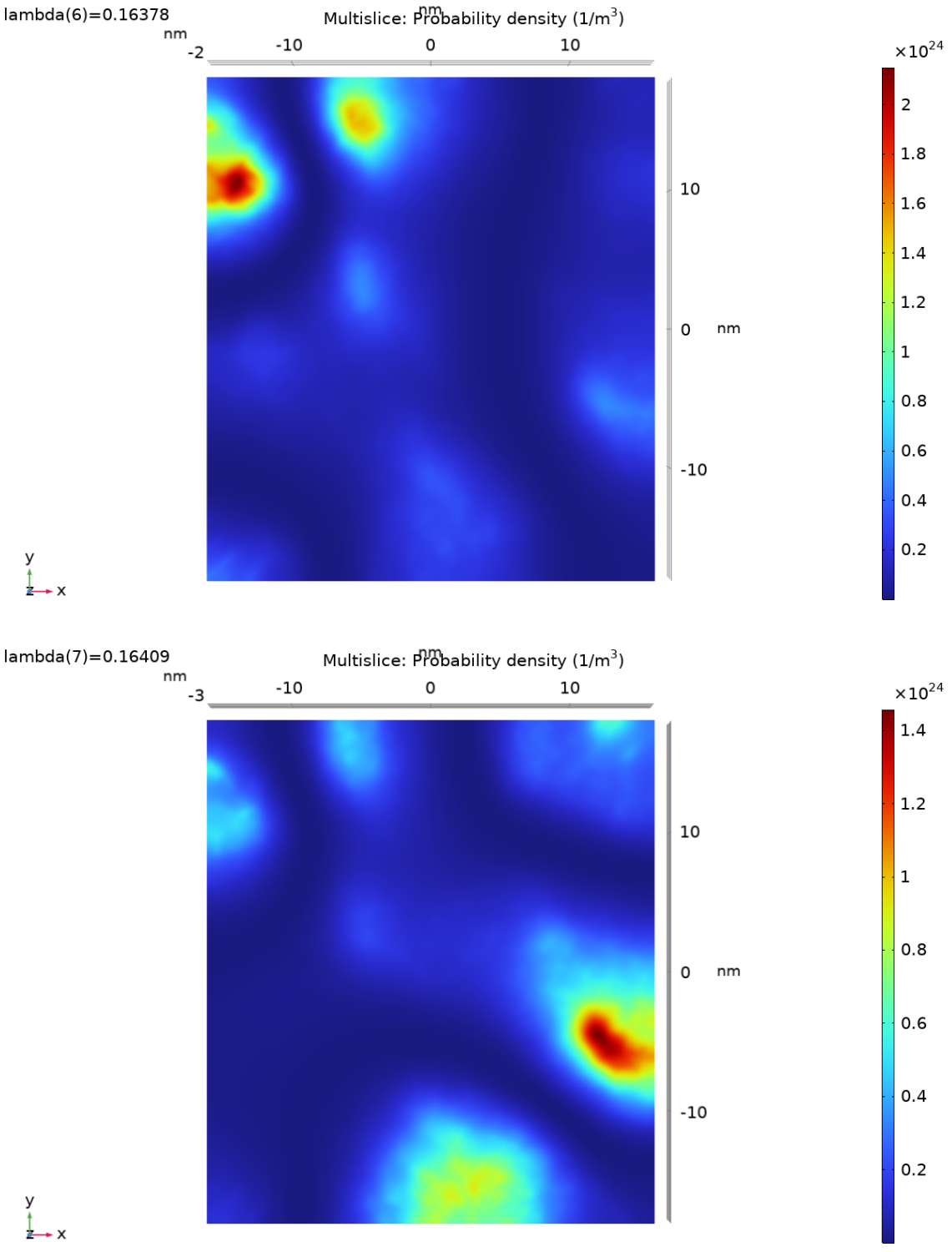

Figure 4.11 - Degenerate Hole States
(order reversed from electron states)

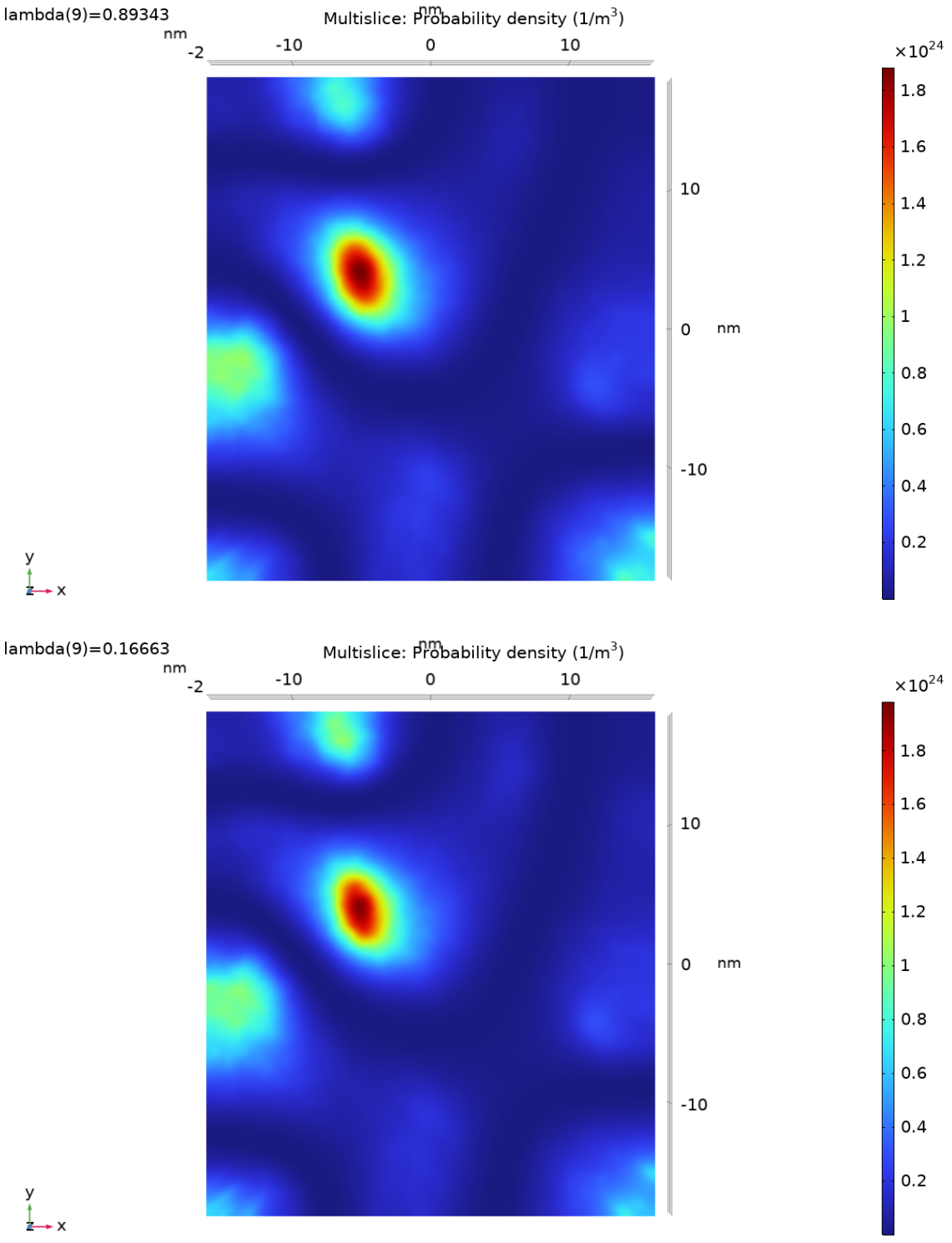

Figure 4.12 - Electron and Hole State

4.4 Coulomb Interaction and Polarization

The observed emission spectrum of the quantum dot ensemble through PL spectroscopy is at lower energies than the simulated transition energy. Additional terms representing strain energy, piezoelectric effects, and other external fields (such as Coulomb interaction and interfacial polarization)[25] are necessary to obtain the most accurate results of the ensemble.[55] This appears in many quantum dot models as confinement is not the only influence on the transition energy of the exciton. Coulombic forces between the oppositely charged (quasi)particles introduce additional energy factors during recombination. Since electrons and holes are attracted to one another, the overall band-band transition energy of the exciton is lowered.

To obtain an estimate for how much Coulomb forces would impact the ensemble energy, it is helpful to use the Brus model which assumes an infinite spherical potential. The magnitude of the Coulomb energy is not significantly affected by the existence of a finite potential.[25] This is because the Coulomb force is proportional to $\frac{1}{R^2}$ and decreases slowly for large R,[64] such as in the case where the wave function extends into the boundary. In the original Brus model, the energy decrease due to Coulomb interaction is[65]

$$E_{Coulomb} = -1.786\frac{e^2}{\epsilon_0 \epsilon_r R} \tag{4.7}$$

where e is the elementary charge and R is the radius of quantum dot. This is a model that many authors still use to this day,[25,66] in spite of its initial inception 40 years ago.

Shortly after Brus released his model, it was refined by Kayanuma to account for the electron-hole spatial correlation effect.[67,68] As a result, a factor of 4π was introduced into the denominator, and the Coulomb energy can be approximated as[69]

$$E'_{Coulomb} = -1.786\frac{e^2}{4\pi\epsilon_0\epsilon_r R} \tag{4.8}$$

The Coulomb energy would be most impacted by the smallest spatial dimension of the quantum dot since it is proportional to $\frac{1}{R}$. This would correspond to height of the ensemble. It is helpful to use the model built in section 2.16 to assess the dielectric permittivity of the core as well as the ensemble height. Recall the cross-sectional height is $4.4\ nm \pm 18\,\%$. None of the observed eigenstates had a probability density greater than this cross-section along the growth axis. Converting this to a radius, $R = 2.2\ nm \pm 18\,\%$. The indium concentration of the core was found to be ~30.5% by isosurface reconstruction for this particular ensemble (in agreement with 31% by Z-contrast HAADF). Using equation (3.68),

$$\epsilon_r(x = 0.305) \approx 13.06$$

Solving equation (4.8) with these values results in

$$E'_{Coulomb} \approx 90 \pm 16\ meV$$

The binding energy is large as the carriers are confined to a region much smaller than their Bohr radius. The Brus model also indicates that there is a surface charge created on the interface between the two connected dielectric media.[65] Differences between

dielectric constants create charge at the interface, generate an electric field, and thereby shift the band structure to lower the recombination energy. In the limit of an infinite confining potential, the polarization energy will reduce the exciton transition energy by[25]

$$E_{Polarization} = \beta \frac{e^2}{\epsilon_0 \epsilon_r R} \tag{4.9}$$

$$\beta = -2 \sum_{n=1}^{\infty} \frac{(\epsilon - 1)(n+1)}{(n\epsilon + n + 1)} \int_0^1 x^{2n} sin^2(\pi x) dx \tag{4.10}$$

$$\epsilon = \frac{\epsilon_{core}}{\epsilon_{matrix}} = \frac{\epsilon_r(x = 0.305)}{\epsilon_r(x = 0)} \approx \frac{13.06}{12.4} \tag{4.11}$$

In order to ensure convergence of β, $n > 14000$.[25] Solving for β in Matlab with $n = 10^6$

$$\beta \approx -0.018$$

Using the same values for $\epsilon_r = \epsilon_{core}$ and $R = 2.2\ nm \pm 18\,\%$ in equation (4.9)

$$E_{Polarization} = 11 \pm 2\ meV$$

Neglecting strain, the transition energy will redshift by approximately

$$E_{redshift} = E'_{Coulomb} + E_{Polarization} \approx 101 \pm 18\ meV \tag{4.12}$$

$$\therefore E'_{simulated} = E_{simulated} - E_{redshift} = 1.35 \pm 0.06\ eV \tag{4.13}$$

Which is in agreement with the transition energy obtained through PL spectroscopy.

$$E_{exciton} \approx 1.32 \pm 0.04\ eV$$

This chapter concludes with assessing the validity of the Brus approach, by assuming an infinite spherical potential and comparing to the obtained eigenstate

solutions. The quantum confinement energies of the electron and hole in an infinite spherical well in the ground state are

$$E_e^{\infty} = \frac{\hbar^2 \pi^2}{2 m_e R^2} \tag{4.14}$$

$$E_h^{\infty} = \frac{\hbar^2 \pi^2}{2 m_h R^2} \tag{4.15}$$

As before, using $R = 2.2\ nm \pm 18\,\%$ for the radius of the quantum dot and equations (3.66) and (3.67) for the electron and heavy hole mass.

$$m_e(x = 0.305) \approx 0.0538 m_0 \approx 4.9 \times 10^{-32}\ kg$$

$$m_h(x = 0.305) \approx 0.3404 m_0 \approx 3.1 \times 10^{-31}\ kg$$

$$E_e^{\infty}(R = 2.2\ nm) \approx 1.44 \pm 0.52\ eV$$

$$E_h^{\infty}(R = 2.2\ nm) \approx 0.23 \pm 0.08\ eV$$

These states are unbound since $E > V_0$ in reference to the GaAs band edge. This is because the wave function is much more confined along the growth axis than along the lateral axis, and the Brus model begins to break down for such small volumes as quantum confinement begins to dominate.[25] Using the semi-minor cross sectional width instead, $R = 6.8\ nm \pm 25\,\%$, solves for much too small confinement energies.

$$E_e^{\infty}(R = 6.8\ nm) \approx 0.15 \pm 0.08\ eV$$

$$E_h^{\infty}(R = 6.8\ nm) \approx 0.02 \pm 0.01\ eV$$

Therefore, neither of these approaches result in the true eigenenergies of the ensemble.

Chapter 5 Future Considerations

5.1 Appending to the Hamiltonian

In the last chapter, it was discussed that quantum confinement is not the only energy that influences the exciton transition. Approximations were made based on the isosurface reconstruction. Although the comparison to photoluminescence spectroscopy indicate that these approximations are reasonable, this is not the main scope of this thesis. The motivation behind this thesis is to provide an accurate means of resolving eigenstates within any general system, whereas in section 4.4 it was limited to the spherical well.

The influence of Coulomb interaction can be generalized using the initial eigenstate solutions. The wave function of each carrier creates a spatial distribution of charge, also known as the space charge density. The space charge density for each carrier is related to the probability density by[70]

$$\rho_e = -e\,|\Psi_e|^2 \tag{5.1}$$

$$\rho_h = +e\,|\Psi_h|^2 \tag{5.2}$$

In the devised model, each finite element has an associated probability density for the eigenstates. Therefore, each element will have a space charge density as well. The space charge density can be used to solve Poisson's equation independently for each carrier with the relative permittivity given by the concentration of the voxel.

$$\nabla^2 V_e = -\frac{\rho_e}{\epsilon_0 \epsilon_r} = \frac{e\,|\Psi_e|^2}{\epsilon_0 \epsilon_r} \tag{5.3}$$

$$\nabla^2 V_h = -\frac{\rho_h}{\epsilon_0 \epsilon_r} = -\frac{e\,|\Psi_h|^2}{\epsilon_0 \epsilon_r} \tag{5.4}$$

V_e and V_h can be determined in COMSOL for each of the finite elements by solving the differential equations. The Hamiltonian can then be appended to include[51]

$$(H + V_h)\Psi'_e = E'_e \Psi'_e \tag{5.5}$$

$$(H + V_e)\Psi'_h = E'_h \Psi'_h \tag{5.6}$$

Where the spatial charge distribution will affect the opposite carrier. H is the single particle Hamiltonian that was used to find the initial set of solutions in chapter 4 without Coulomb interaction. $\Psi'_{e/h}$ and $E'_{e/h}$ represent the new set of wave functions and eigenenergies that are obtained through resolving the system with the included electrostatic potential using the Poisson correction. This process can be repeated until the wave functions and eigenenergies stop changing with each successive iteration. This is termed a self-consistent solution as there is convergence to the system of equations.[51] The exciton transition energy can then be determined[51]

$$E_{exciton} = E'_e - E'_h + \frac{1}{2}\left[< \Psi'_h\,|\,V_e\,|\,\Psi'_h > - < \Psi'_e\,|\,V_h\,|\,\Psi'_e > \right] \tag{5.7}$$

Where the matrix elements represent energy corrections to account for Coulomb energy being included twice, for both charge carriers simultaneously.[51]

If it is known how an external field (magnetic, strain, electrostatic, etc) influences the potential of the Hamiltonian, any correctional technique can be applied throughout the entire modelling domain.

5.2 Improving Reconstruction Geometry

During atom probe tomography, data is acquired along a cone aligned with the growth axis. One downfall of the model created in this thesis is that it is unable to use the complete data set and uses a small subset of space that contains no data. It fills the null space with the closest available region, which would be on the border of the available data set. This creates an artificial extension of the band structure into the null region. The problem stems from utilizing a cubic reconstruction of the conically shaped data.

The plot in figure 5.1 depicts the minimum nearest neighbour used for each of the columns in the modelling domain. The corner maximum of 11 nearest neighbours is different than the spatial resolution provided in chapter 3, as it only accounts for half of the search to the boundary. However, it is ~ 4x worse than the spatial resolution in the centre. Using equation (3.54) and dividing by 2,

$$\delta_{11} = \frac{1}{2}\left(2(11)+1\right)\sqrt{3}(0.2\ nm) \approx 4\ nm$$

There exists more data along the centre of the $\hat{x}$ and $\hat{y}$ axes that cannot be used as it is outside the modelling domain. If the modelling domain was expanded, the corners would encompass more null space and would not be an accurate reconstruction of the

available data set. A greater number neighbours would be needed for the corners, thereby further deteriorating the corner spatial resolution. Similarly, if the modelling domain was contracted to completely remove all null space, some of the large indium clusters would be missed in the model. A simple way around this is to box the clusters individually. This has the benefit of a utilizing a much faster build and solve time, but would not depict any of the interesting hybridized dot-dot states that were observed.

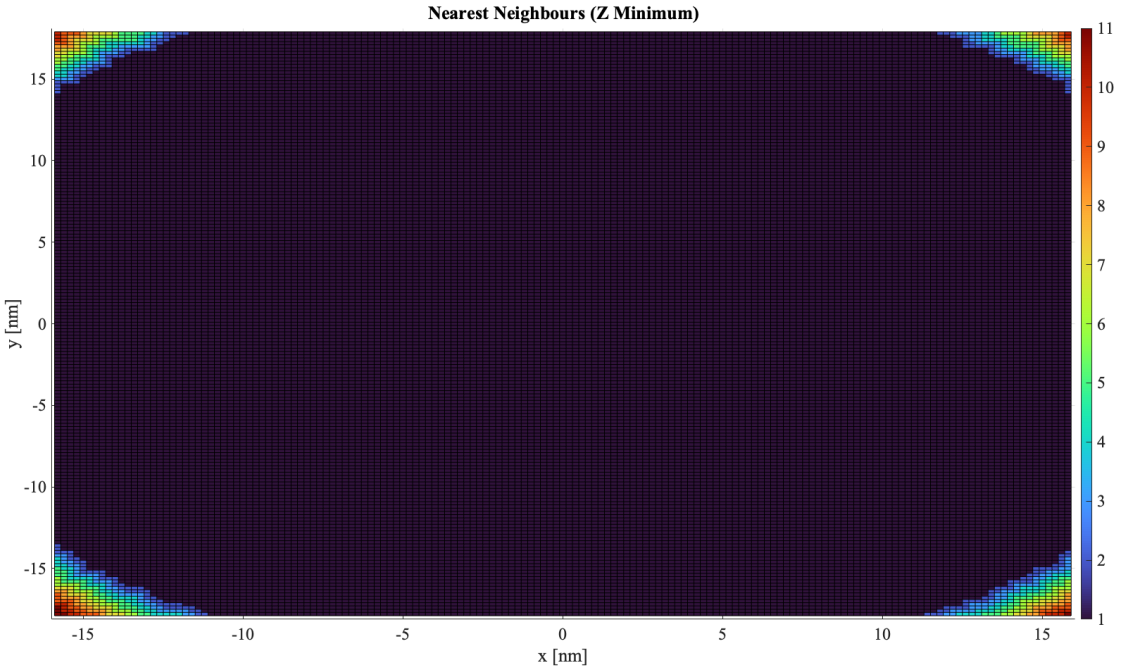

Figure 5.1 - Null Corners

The best method to remedy this issue is to remove all the null voxels from the modelling domain altogether. This would be different than resolving null voxels in the central component of the data, as now obtaining a wave function in the corners would be undesirable from lack of data. The entire data set could then be used and all the null

regions outside would be completely neglected. This solution is viable, but isn't very straightforward to implement due to the complexity of domain enumeration. Similar to an address, each voxel has its own numerical value assigned to it based on its position in the modelling domain. This is a key aspect toward determining the voxel material properties (effective mass, potential energy, and relative permittivity) as well as systematically meshing the model. Domain enumeration no longer becomes a simple process like the method demonstrated in chapter 3. Instead, different planes will contain a variable number of domains that would require more sophisticated mapping algorithms.

Moving toward a Voronoi tessellation would also be interesting and provide many benefits. Instead of a cubic voxel, each grid component becomes a polyhedron consisting of the subset of space that is the shortest Euclidean distance to any one of the points in the data set (one singular ion of interest). Since Delaunay triangulation is the dual graph of Voronoi tessellation, meshing may become quicker to resolve than triangulating a cube. This is the current bottle-neck in building and solving models, taking up vast majority of the time and imposing the most demanding memory requirements. Furthermore, this would be the only method to accomplish building a truly digital alloy QD without utilizing any neighbour searching. The only downfall is that voxel reconstruction and domain enumeration would become much more complex than a simple cubic grid.

Chapter 6 Conclusion

The model presented in this paper represents a good starting point for realistic 3-dimensional eigenstate solutions of the Schrödinger equation within a quantum dot ensemble. More work is necessary to obtain the most accurate results possible by including other forms of potential energy within the system. However, in its current state, the model is still very promising and useful for its purpose, making it encouraging to assess its validity in a variety of differently shaped ensembles or other lattice systems.

Multiple forms of microscopy (TEM, AFM, and APT) were used to assess the size distribution and concentration of indium cores within the quantum dot ensemble. It was found that each had their own set of associated benefits and disadvantages, with APT isosurface reconstruction being the most reasonably accurate method of depicting an ensemble average. Even so, it was still unable to accurately provide the eigenstate solutions of the ensemble without devising a more sophisticated model based on the raw atom probe data itself. This is because small changes to the structure result in large changes to the eigenenergies, especially for relatively very small sized quantum dots.

Both Comsol and Matlab had to be used concurrently to be able to devise a model of such magnitude. Several considerations had to be accounted for as well during this process, namely transitioning 0-dimensional scatter data into 3-dimensional volumes, filling empty space to provide the most reasonable spatial resolution, and imposing the proper boundary constraints on the wave function.

Though the simulated transition energy of the exciton was blue shifted from the photoluminescence spectroscopy data, it was still possible to bring these two results closer together by considering other effects such as polarization and Coulomb interaction. For this purpose, isosurface reconstruction was extremely useful in conjunction with the devised model to obtain an accurate representation of the transition energy. It was found that the standard deviation between the photoluminescence emission data and the simulated quantum dot eigenenergies were the same. This was an unexpected result, possibly indicating that the emission inhomogeneity of dots can be quantified through this model. However, further testing would be necessary to confirm this result.

Hybrid states were discovered that consist of both bonding and anti-bonding between neighbouring quantum dots. To the best of my knowledge, the simulation of eigenstates for an entire quantum dot ensemble simultaneously through means of experimental data has not been documented in literature. This model would be able to successfully transition to the simulation of other structures, such as delocalized stacked quantum dot layers, quantum well digital alloys, quantum dots embedded within nanowires, and many other exciting opportunities. This opens up the door to be able to use these modelling techniques for a variety of research endeavours, including other band and lattice structures. Overall, the atom probe was an extremely excellent tool to quantify quantum dots for their size, composition, and emission energy.

Works Cited

1. Otto, C. Dynamics of Quantum Dot Lasers: Effects of Optical Feedback and External Optical Injection. Springer. (2014).

2. Alferov, Z. The double heterostructure concept and its applications in physics, electronics, and technology. Reviews of Modern Physics. Volume 73, Issue 3, Pages 767-782 (2001).

3. Kapon, E. Chapter 4 - Quantum Wire and Quantum Dot Lasers. Optics and Photonics, Semiconductor Lasers I. Academic Press. 291-360 (1999).

4. Chow, W.W., Koch, S.W. Semiconductor-Laser Fundamentals. Springer. (1999).

5. Park, J., Tang, M., Chen, S., Liu, H. Chapter Eleven - Monolithic III–V quantum dot lasers on silicon. Frontiers of Nanoscience. Elsevier. Volume 20, 353-388 (2021).

6. Ahamed, M.I., Ahamed, M., Muthaiyan, R. Modelling of density of states and energy level of chalcogenide quantum dots. International Review of Applied Sciences and Engineering. 13(1), 42-46 (2021).

7. Irvine, S., Capper, P. Metalorganic Vapor Phase Epitaxy (MOVPE): Growth, Materials Properties, and Applications. John Wiley & Sons, Inc. (2020).

8. Suzuki, T., Singh, R. Chapter Eight - Coherent control of a semiconductor quantum dot ensemble. Semiconductors and Semimetals. Elsevier. Vol 105, 347-385 (2020).

9. Pinkert, T., Salumbides, E., Tahvili, M., Ubachs, W., Bente, E., Eikema, K. Frequency comb generation by CW laser injection into a quantum-dot mode-locked laser. Opt. Express 20. (2012).

10. Liu, L., Zhang, X., Xu, T., Dai, Z., Liu, T. Simple optical frequency comb generation using a passively mode-locked quantum dot laser. Optics Communications. Vol 396, 105-109 (2017).

11. Grillot, F., Arsenijevic, D., Bimberg, D., Huang, H. Ultrafast and nonlinear dynamics of InAs/GaAs semiconductor quantum dot lasers. Quantum Dots and Nanostructures: Growth, Characterization, and Modelling (2018).

12. Huang, H. et al. Epitaxial quantum dot lasers on silicon with high thermal stability and strong resistance to optical feedback. APL Photonics 5, 016103 (2020).

13. Erneux, T., Glorieux, P. Laser Dynamics. Cambridge University Press. (2010).

14. Khanonkin, I., Bauer, S., Mikhelashvili, V., Eyal, O., Lorke, M., Jahnke, F., Reithmaier, J.P., Eisenstein, G. On the principle operation of tunneling injection quantum dot lasers. Progress in Quantum Electronics. 100362 (2021).

15. Asahi, H., Horikoshi, Y. Molecular Beam Epitaxy: Materials and Applications for Electronics and Optoelectronics. John Wiley & Sons, Inc. (2019).

16. Hong, S., Kim, J., Lee, J., Kwack, H., Han, W., Oh, D. Self-alignment of self-assembled InAs quantum dots. Journal of Crystal Growth. Vol 286, Issue 1, 18-22 (2006).

17. Gaan, S., He, G., Feenstra, R.M., Walker, J., Towe, E. Size, shape, composition, and electronic properties of InAs/GaAs quantum dots by scanning tunneling microscopy and spectroscopy. Journal of Applied Physics. 108 (11): 114315 (2010).

18. Torelly, G., Jakomin, R., Pinto, L.D., Pires, M.P., Ruiz, J., Caldas, P.G., Prioli, R., Xie, H., Ponce, F., Souza P. Early nucleation stages of low density InAs quantum dots nucleation on GaAs by MOVPE. Journal of Crystal Growth. Vol 434, 47-54 (2016).

19. Kumar, S., Biswas, D. Effects of a Gaussian size distribution on the absorption spectra of III-V semiconductor quantum dots. Journal of Applied Physics. 102 (8), 084305 (2007).

20. Jia, H., Yang, J., Tang, M., Li, W., Jurczak, P., Yu, X., Zhou, T., Park, J., Li, K., Deng, H., Yu, X., Li, A., Chen, S., Seeds, A., Liu, H. The Epitaxial Growth and Unique Morphology of InAs Quantum Dots Embedded in a Ge Matrix. Journal of Physics D: Applied Physics. 55 (2022).

21. Kabi, S., Unil Perera, A.G. Effect of quantum dot size and size distribution on the intersublevel transitions and absorption coefficients of III-V semiconductor quantum dot. Journal of Applied Physics. 117 (12), 124303 (2015).

22. Ma, J., Ji, X., Wang, G., Wei, X., Lu, H., Yi, X., Duan, R., Wang, J., Zeng, Y., Li, J., Yang, F., Wang, C., Zou, G. Anomalous temperature dependence of photoluminescence in self-assembled InGaN quantum dots. Applied Physics Letters. 101 (13), 131101 (2012).

23. Liang, S., Zhu, H.L., Pan, J.Q., Ye, X.L., Wang, W. Growth of InAs quantum dots on vicinal GaAs (100) substrates by metalorganic chemical vapor deposition and their optical properties. Journal of Crystal Growth. Vol 289, Issue 2, 477-484 (2006).

24. Williams, D., Carter, C. Transmission Electron Microscopy: A Textbook for Materials Science. Springer. (2009).

25. Ferreira, D.L., Sousa, J., Maronesi, R., Bettini, J., Schiavon, M., Teixeira, A., Silva, A.G. Size-dependent bandgap and particle size distribution of colloidal semiconductor nanocrystals. J. Chem. Phys. 147 (15), 154102 (2017).

26. Chen, Z.B., Lei, W., Chen, B., Wang, Y.B., Liao, X.Z., Tan, H., Zou, J., Ringer, S., Jagadish, C. Preferential nucleation and growth of InAs/GaAs(001) quantum dots on defected sites by droplet epitaxy. Scripta Materialia. Vol 69, Issue 8, 638-641 (2013).

27. Kaida, R., Akiyama, T., Nakamura, K., Ito, T. Theoretical study for misfit dislocation formation at InAs/ GaAs(001) interface. Journal of Crystal Growth. Vol 468, 919-922 (2017).

28. Toujyou, T., Konishi, T., Hirayama, M., Yamaguchi, K., Tsukamoto, S. Intermittent growth for InAs quantum dot on GaAs(001). Journal of Crystal Growth. Vol 551. 125891, (2020).

29. Fang. H., Bechtel, H.A., Plis, E., et al. Quantum of optical absorption in two-dimensional semiconductors. Proc Natl Acad Sci. 110(29), 11688-11691 (2013).

30. Harrison, P., Valavanis, A. Quantum Wells, Wires and Dots: Theoretical and Computational Physics of Semiconductor Nanostructures. Fourth Edition. Wiley. (2016).

31. EDS analysis: Energy Dispersive Spectroscopy: Thermo fisher scientific - US. EDS.

32. Meier, M.S., et al. Large-Scale Atom Probe Tomography Data Mining: Methods and Application to Inform Hydrogen Behavior. Microscopy and Microanalysis. Vol 29, Issue 3, 879–889 (2023).

33. Peng, Z., Vurpillot, F., Choi, P., Li, Y., Raabe, D. Gault, B. On the detection of multiple events in atom probe tomography. Ultramicroscopy. Volume 189, 54-60 (2018).

34. Atom Probe Tomography - introduction to the technique - CAMECA.

35. Miller, M.K. Atom Probe Tomography: Analysis at Atomic Level. Kluwer Academic. (2000).

36. Morita, M., et al. Evaluation of Detection Efficiency of Atom Probe Tomography. Journal of Surface Analysis. Vol 20, No. 3, 177−181 (2014).

37. Cuduvally, R., et al. Potential sources of compositional inaccuracy in the atom probe tomography of $In_xGa_{1-x}As$. Ultramicroscopy. Vol 210, 112918 (2020).

38. Di Russo, E., Blum, I., Rivalta, I., Houard, J., Da Costa, G., Vurpillot, F., Blavette, D., Rigutti, L. Detecting Dissociation Dynamics of Phosphorus Molecular Ions by Atom Probe Tomography. The Journal of Physical Chemistry A. 124 (52), 10977-10988 (2020).

39. Koelling, S., Stehouwer, L., Paquelet Wuetz, B., Scappucci, G., Moutanabbir, O. Three-Dimensional Atomic-Scale Tomography of Buried Semiconductor Heterointerfaces. Adv. Mater. Interfaces, 10, 2201189 (2023).

40. Dyck, O., Leonard, D. N., Edge, L. F., Jackson, C. A., Pritchett, E. J., Deelman, P. W., Poplawsky, J. D. Accurate Quantification of Si/SiGe Interface Profiles via Atom Probe Tomography. Adv. Mater. Interfaces, 4, 1700622 (2017).

41. Vurpillot, F., Bostel, A., Blavette, D. A new approach to the interpretation of atom probe field-ion microscopy images. Ultramicroscopy. Vol 89, Issues 1–3, 137-144 (2001).

42. Rigutti, L., et al. Statistical correction of atom probe tomography data of semiconductor alloys combined with optical spectroscopy: The case of $Al_{0.25}Ga_{0.75}N$. Journal of Applied Physics. 119 (10), 105704 (2016).

43. Schubert, M., et al. Optical constants of $Ga_xIn_{1-x}P$ lattice matched to GaAs. Journal of Applied Physics. 77 (7), 3416–3419 (1995).

44. Attolini, G., et al. Optical and structural characterization of LP MOVPE grown lattice matched InGaP/GaAs heterostructures. Materials Science and Engineering: B. Vol 91–92, 123-127 (2002).

45. Dong, Y., Feenstra, R.M., Semtsiv, M.P., Masselink, W.T. Band offsets of InGaP/GaAs heterojunctions by scanning tunneling spectroscopy. Journal of Applied Physics. 103 (7), 073704 (2008).

46. Serafińczuk, J., et al. High-resolution X-ray diffraction to probe quantum dot asymmetry. Measurement. 113451 (2023).

47. Gault, B., et al. Atom probe tomography. Nature Reviews Methods Primers. 1. 51 (2021).

48. Gault, B., et al. Transmission Kikuchi diffraction mapping induces structural damage in atom probe specimens. Microscopy and Microanalysis. 29, no. 3 1026-1036 (2023).

49. Chiarotti, G., Goletti, C. Surfaces and Interfaces, Electronic Structure of. Encyclopedia of Condensed Matter Physics. Elsevier. 133-144 (2005).

50. Gault, B., et al. Analysis Techniques for Atom Probe Tomography. In: Atom Probe Microscopy. Springer Series in Materials Science. Vol 160 (2012).

51. Nari, J., et al. Alloy Fluctuations Act as Quantum Dot-like Emitters in GaAs-AlGaAs Core-Shell Nanowires. ACS nano. (2015).

52. Townsend, J.S. A Modern Approach to Quantum Mechanics. Viva Books. (2017).

53. Griffiths, D.J. Introduction to quantum mechanics. Prentice Hall. (2005).

54. COMSOL Online Documentation. *Open Boundary*. Comsol Multiphysics.

55. Mantashian, G.A., Mantashyan, P.A., Hayrapetyan, D.B. Modeling of Quantum Dots with the Finite Element Method. *Computation*. 11 (1) (2023).

56. COMSOL Multiphysics Reference Manual. Version 5.5.

57. Gothäll, H. *Is Meshing Run in Parallel in Comsol Multiphysics?* COMSOL Multiphysics. (2019).

58. Kim, B., Kyhm, K., Je, K.C., Song, J.D., Kim, S.Y., Le, E.H., Taylor, R.A. Low gain threshold density of a single InGaP quantum well sandwiched by digital alloy. Current Applied Physics. Vol 14, Issue 9, 1293-1295 (2014).

59. Schliwa, A. Impact of size, shape, and composition on piezoelectric effects and electronic properties of In(Ga)As/GaAs quantum dots. Phys. Rev. B. 76 (20), 205324 (2007).

60. Li, H.E. Material parameters of InGaAsP and InAlGaAs systems for use in quantum well structures at low and room temperatures.

61. Sautter, K., Vallejo, K., Simmonds, P. Strain-driven quantum dot self-assembly by molecular beam epitaxy. J. Appl. Phys. 128 (3), 031101 (2020).

62. Weisstein, E.W. Gaussian Function. MathWorld — A Wolfram Web Resource.

63. Panish, M., Casey, H. Temperature Dependence of the Energy Gap in GaAs and GaP. J. Appl. Phys. 40 (1), 163–167 (1969).

64. Ivanov, D., Kolikov, K. Short-range action and long-range action of the electrostatic forces within atomic nuclei. Natural Science, 5, 508-513 (2013).

65. Brus. L.E. Electron–electron and electron-hole interactions in small semiconductor crystallites: The size dependence of the lowest excited electronic state. J. Chem. Phys. 80 (9) 4403–4409 (1984).

66. Mughnetsyan, V., Movsisyan, A., Kirakosyan, A. Electron–hole interaction in cylindrical quantum dots. Physica E: Low-dimensional Systems and Nanostructures. Vol 144, 115366 (2022).

67. Kayanuma, Y. Quantum-size effects of interacting electrons and holes in semiconductor microcrystals with spherical shape. Physical Rev B Condensed Matter. 38(14) 9797-9805 (1988).

68. Chukwuocha, E., Onyeaju, M., Harry, T. Theoretical Studies on the Effect of Confinement on Quantum Dots Using the Brus Equation. World Journal of Condensed Matter Physics. 2. 96-100 (2012).

69. Safeera, T.A., Khanal, R., Medvedeva, J., Martinez, A., Vinitha, G., Anila, E. Low temperature synthesis and characterization of zinc gallate quantum dots for optoelectronic applications. Journal of Alloys and Compounds. Vol 740, 567-573 (2018).

70. Sebens, C. Electron Charge Density: A Clue from Quantum Chemistry for Quantum Foundations. California Institute of Technology. Forthcoming in Foundations of Physics (2021).

Appendix 1: InGaP Interface Proxigrams

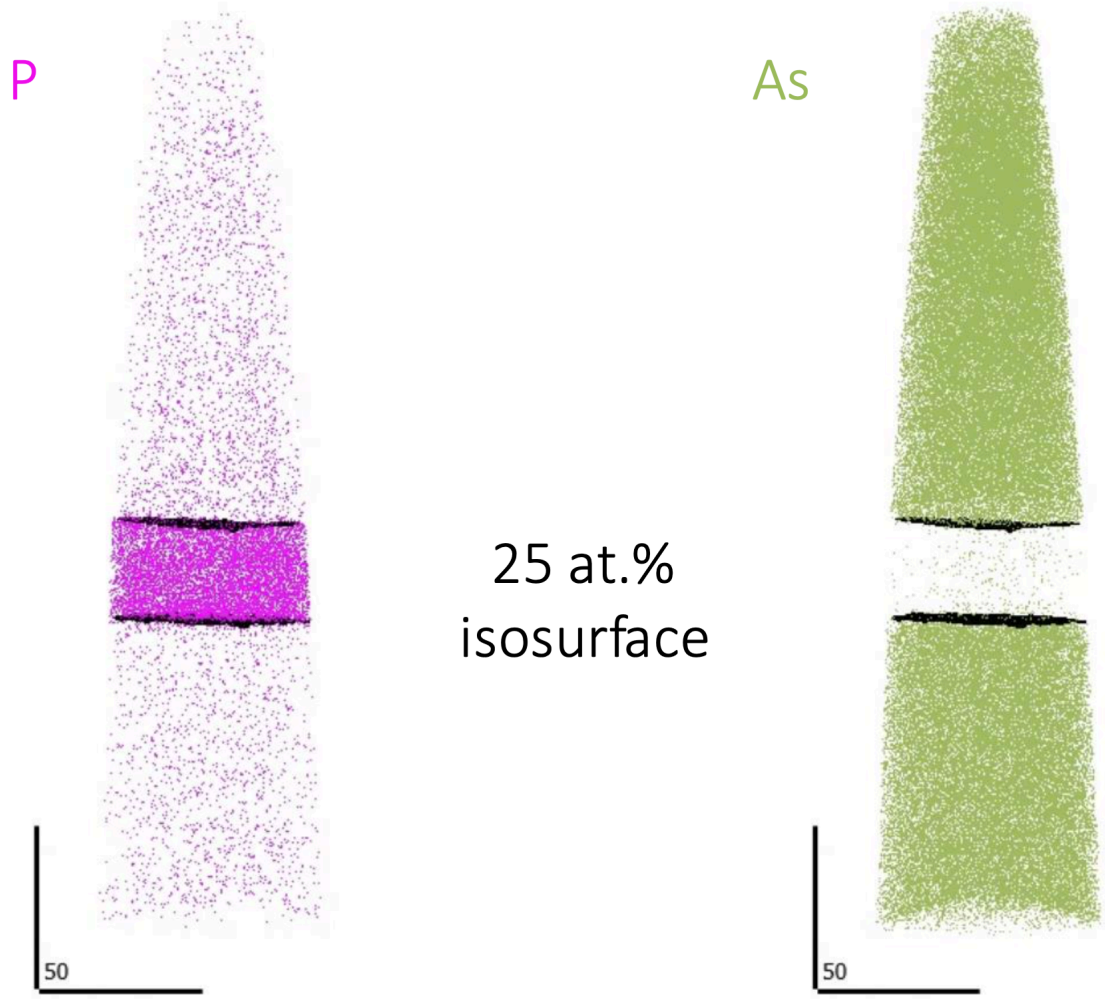

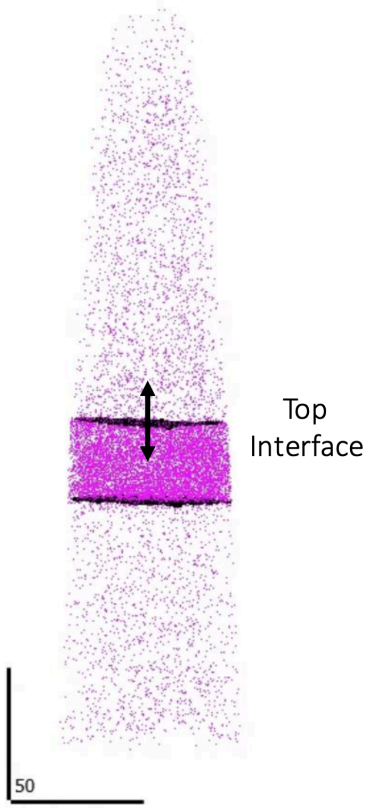
Top
Interface
50

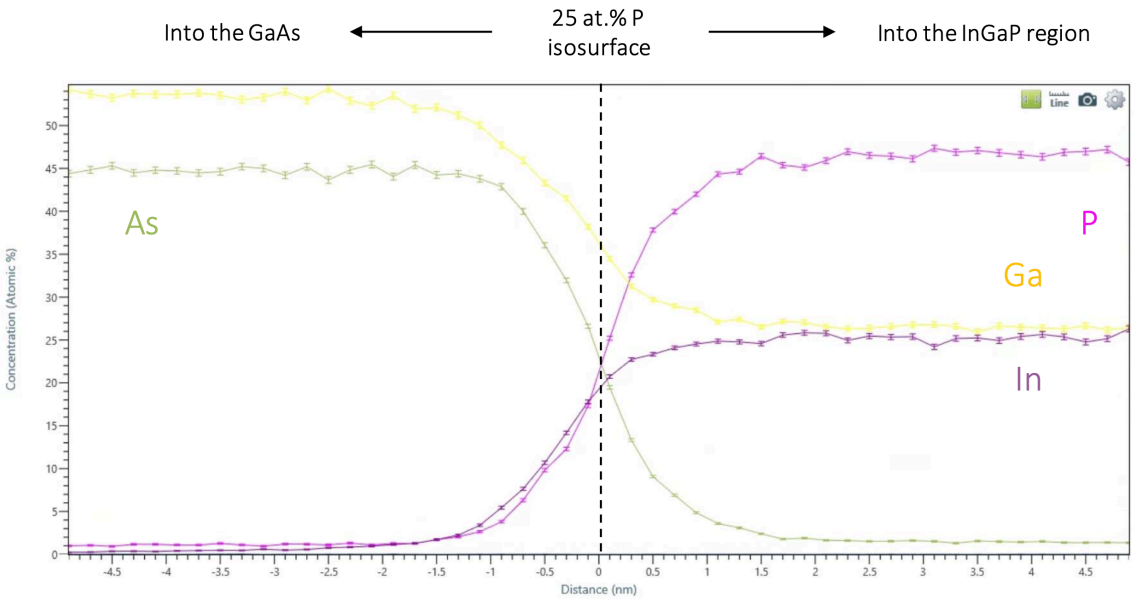
Into the GaAs
25 at.% P
isosurface
Into the InGaP region
As
P
Ga
In
Concentration (Atomic %)
Distance (nm)

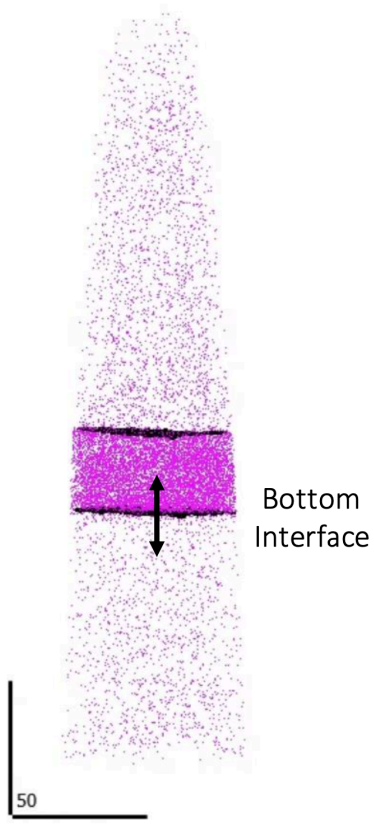
Bottom
Interface
50

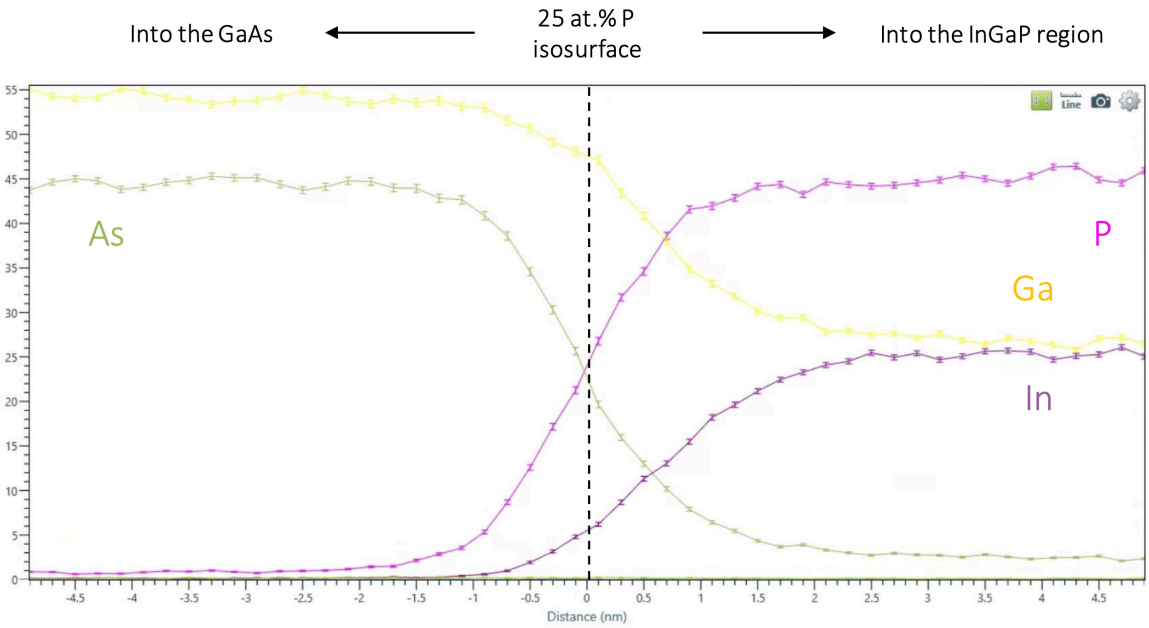
Into the GaAs
25 at.% P
isosurface
Into the InGaP region
As
P
Ga
In
Distance (nm)

Appendix 2: $In_{1-x}Ga_xP$ HRXRD

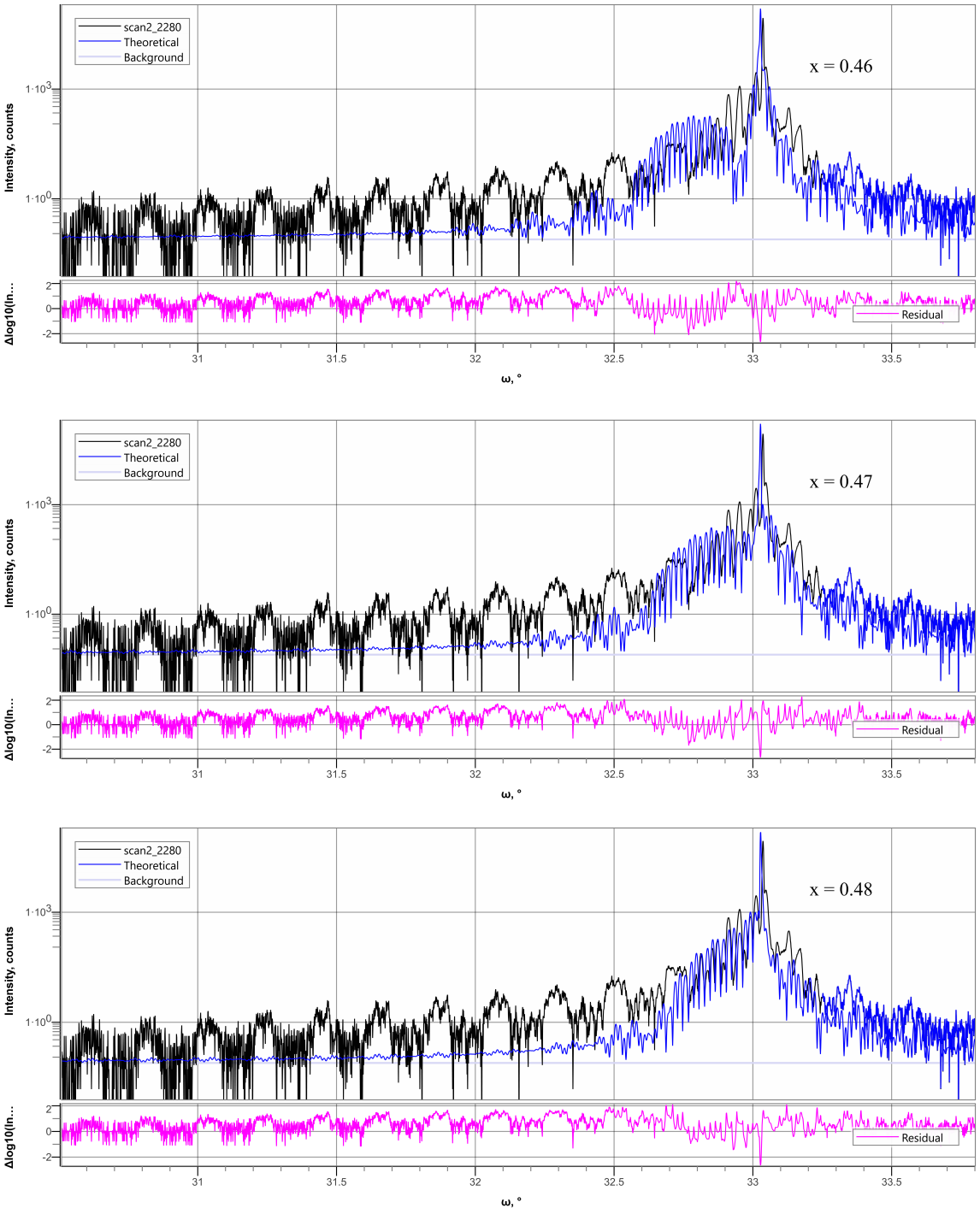

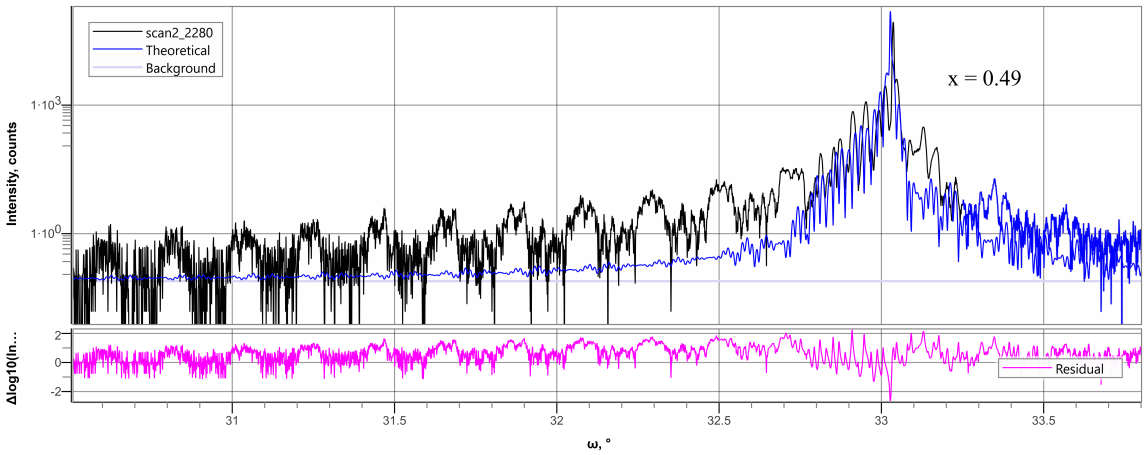
scan2_2280
Theoretical
Background
x = 0.49
Intensity, counts
Residual
ω, °

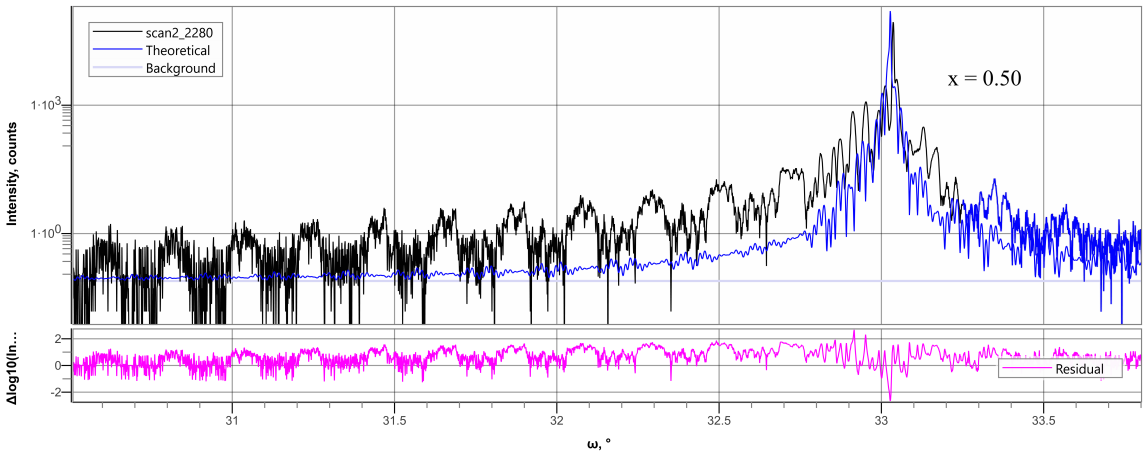
scan2_2280
Theoretical
Background
x = 0.50
Intensity, counts
Residual
ω, °

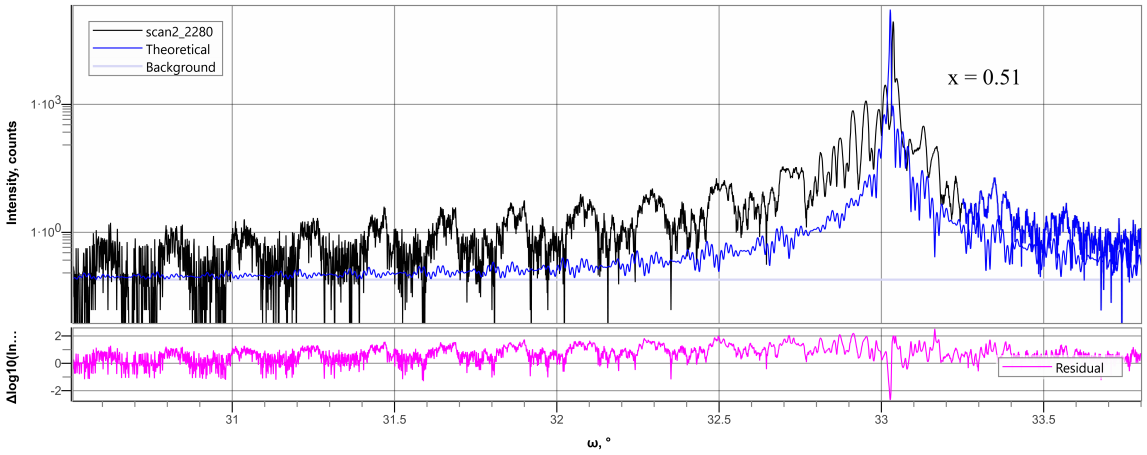
scan2_2280
Theoretical
Background
x = 0.51
Intensity, counts
Residual
ω, °

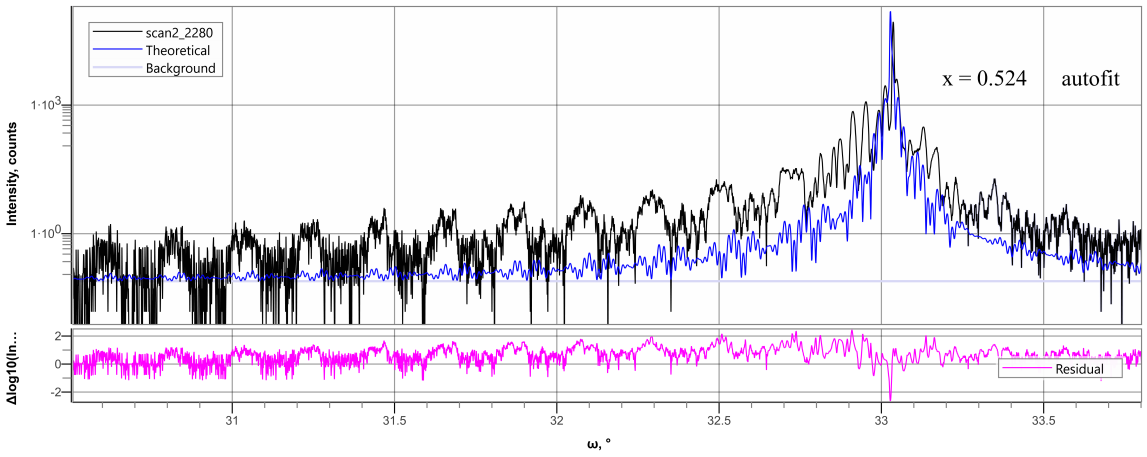
scan2_2280
Theoretical
Background
x = 0.524
autofit
Intensity, counts
1·10^3
1·10^0
Δlog10(In…
2
0
-2
Residual
31
31.5
32
32.5
33
33.5
ω, °

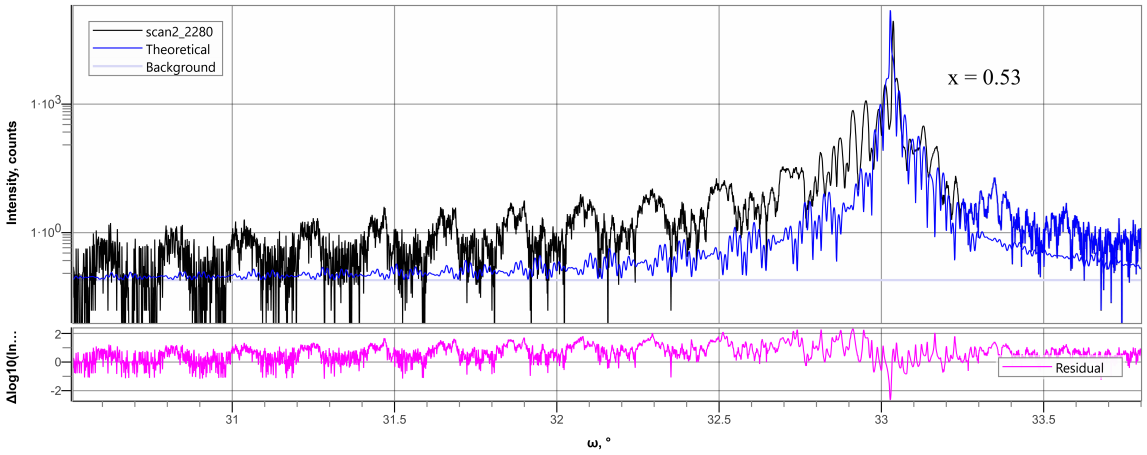
scan2_2280
Theoretical
Background
x = 0.53
Intensity, counts
1·10^3
1·10^0
Δlog10(In…
2
0
-2
Residual
31
31.5
32
32.5
33
33.5
ω, °

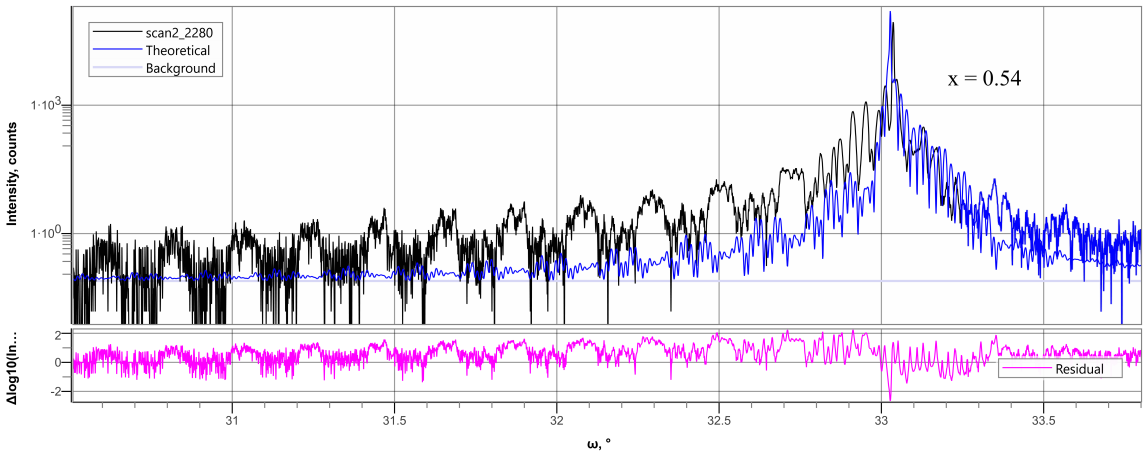
scan2_2280
Theoretical
Background
x = 0.54
Intensity, counts
1·10^3
1·10^0
Δlog10(In…
2
0
-2
Residual
31
31.5
32
32.5
33
33.5
ω, °

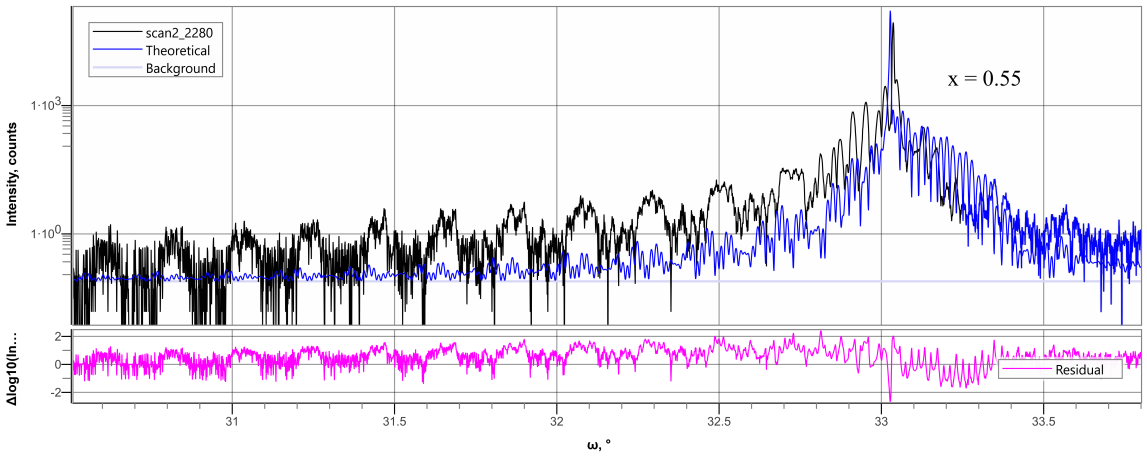
scan2_2280
Theoretical
Background
x = 0.55
Intensity, counts
1·10^3
1·10^0
Δlog10(In…
2
0
-2
Residual
31
31.5
32
32.5
33
33.5
ω, °

Appendix 3: Finite Spherical Well

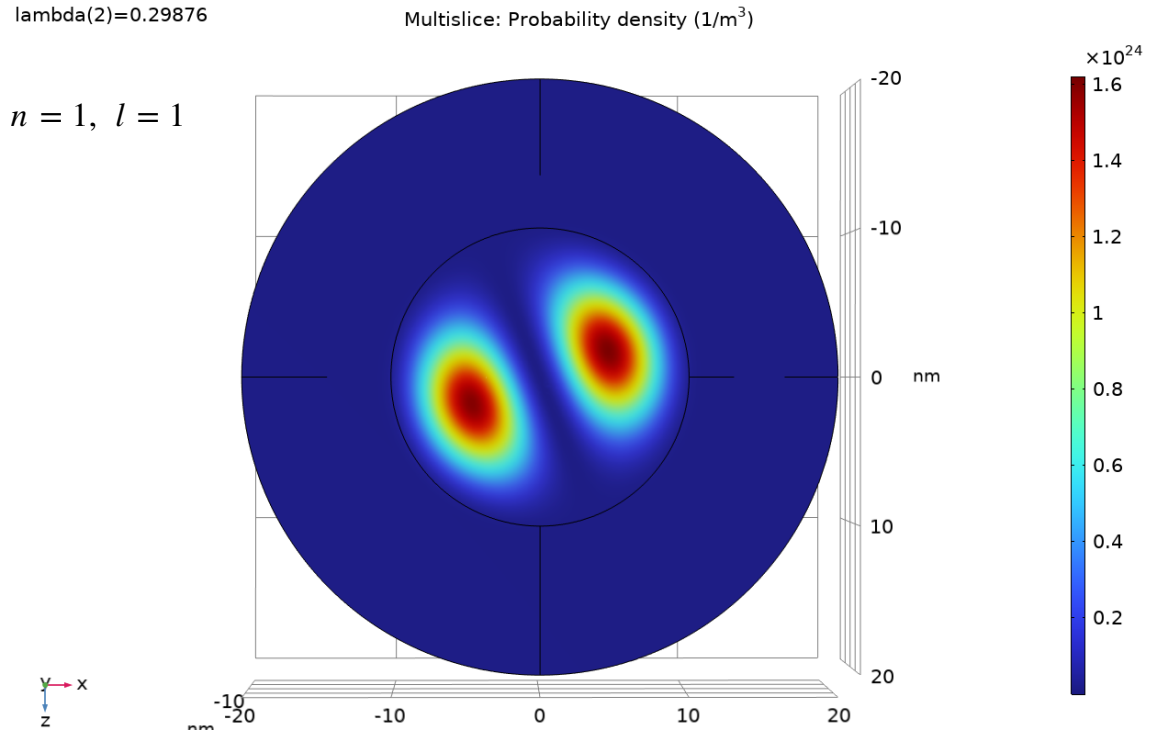

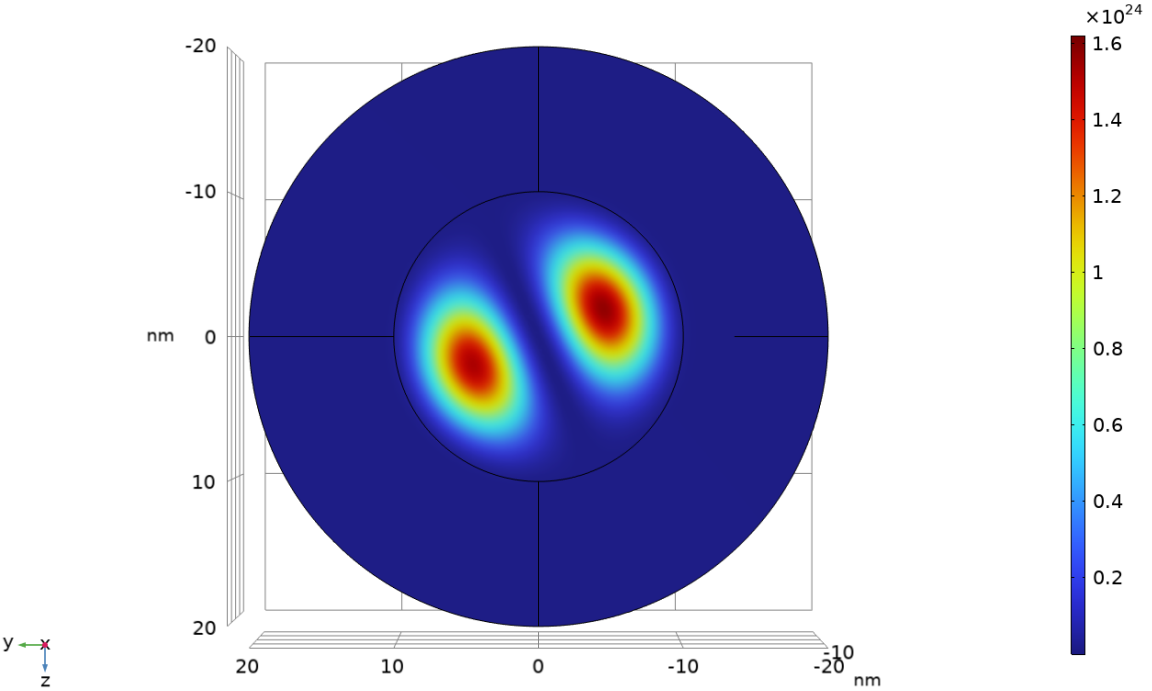

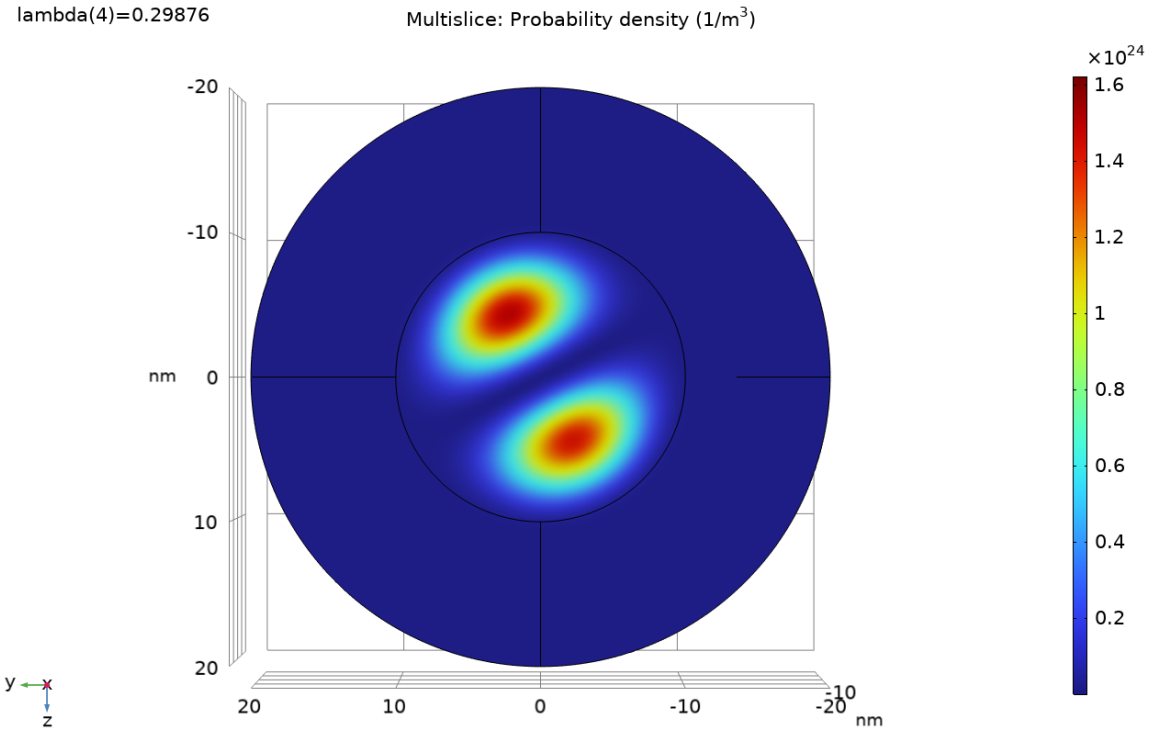
lambda(4)=0.29876
Multislice: Probability density (1/m^3)
×10^24
1.6
1.4
1.2
1
0.8
0.6
0.4
0.2
-20
-10
0
10
20
nm
20
10
0
-10
-20
nm
y
x
z

$n = 1,\ l = 2$

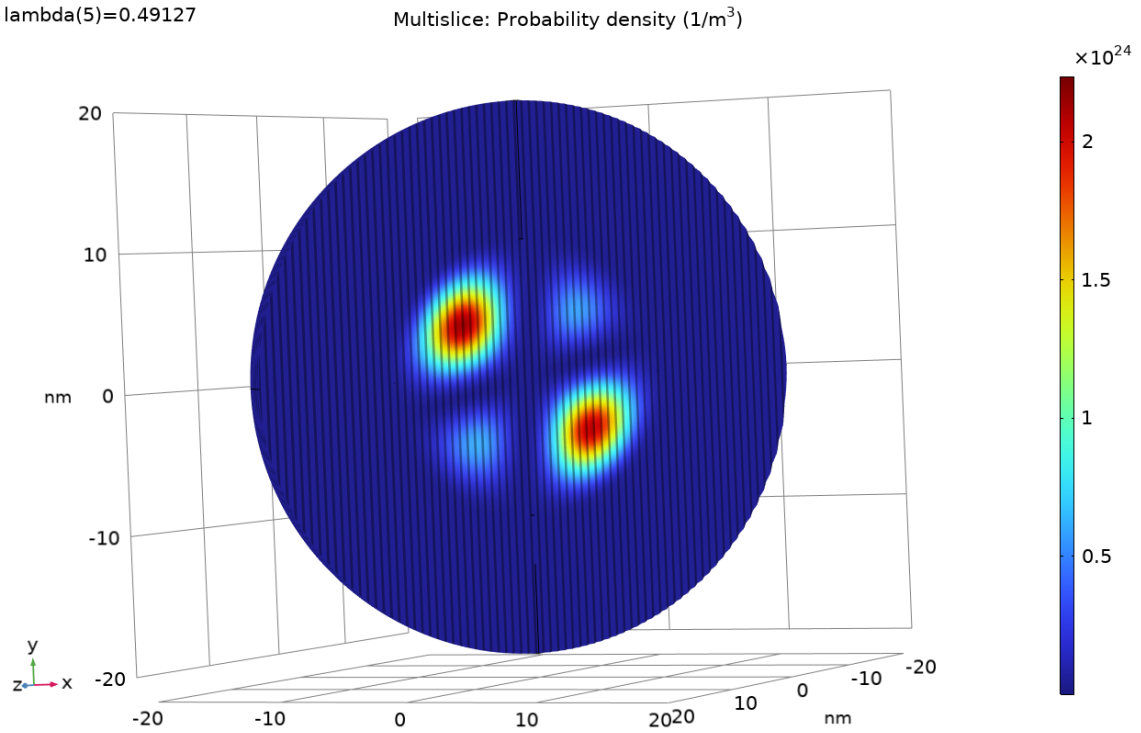
lambda(5)=0.49127
Multislice: Probability density (1/m3)
×10^24
2
1.5
1
0.5
20
10
nm 0
-10
-20
y
z
x
-20
-10
0
10
20
nm

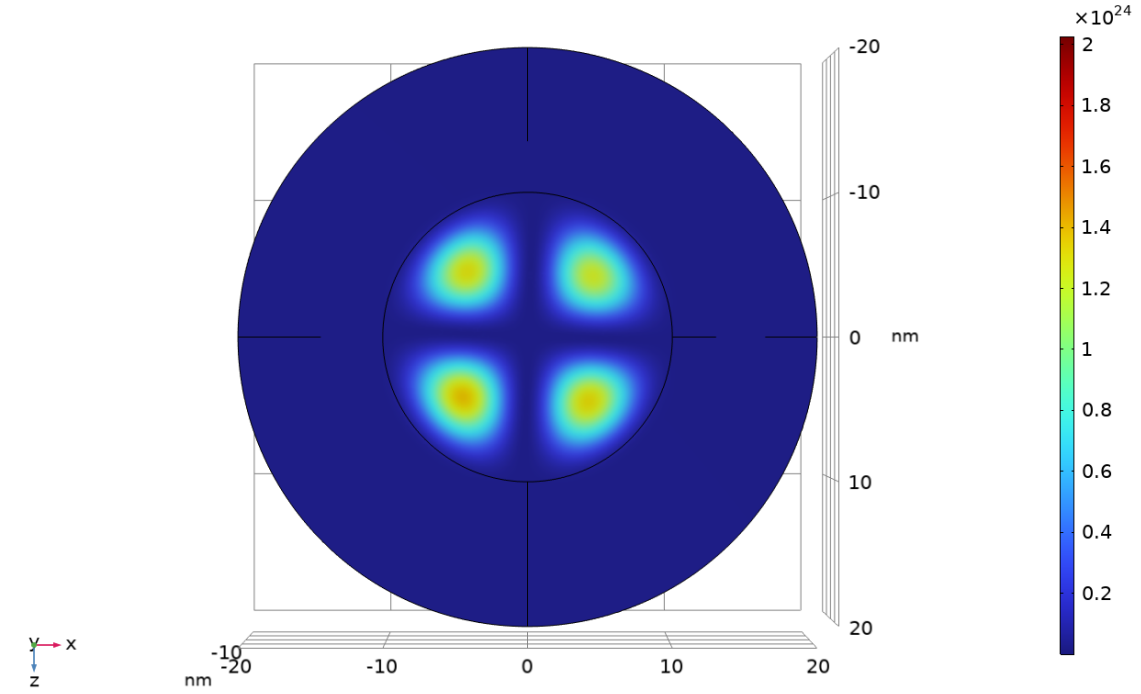
lambda(6)=0.49127
Multislice: Probability density (1/m3)
×10^24
2
1.8
1.6
1.4
1.2
1
0.8
0.6
0.4
0.2
-20
-10
0 nm
10
20
y
x
z
-10
-20
-10
0
10
20
nm

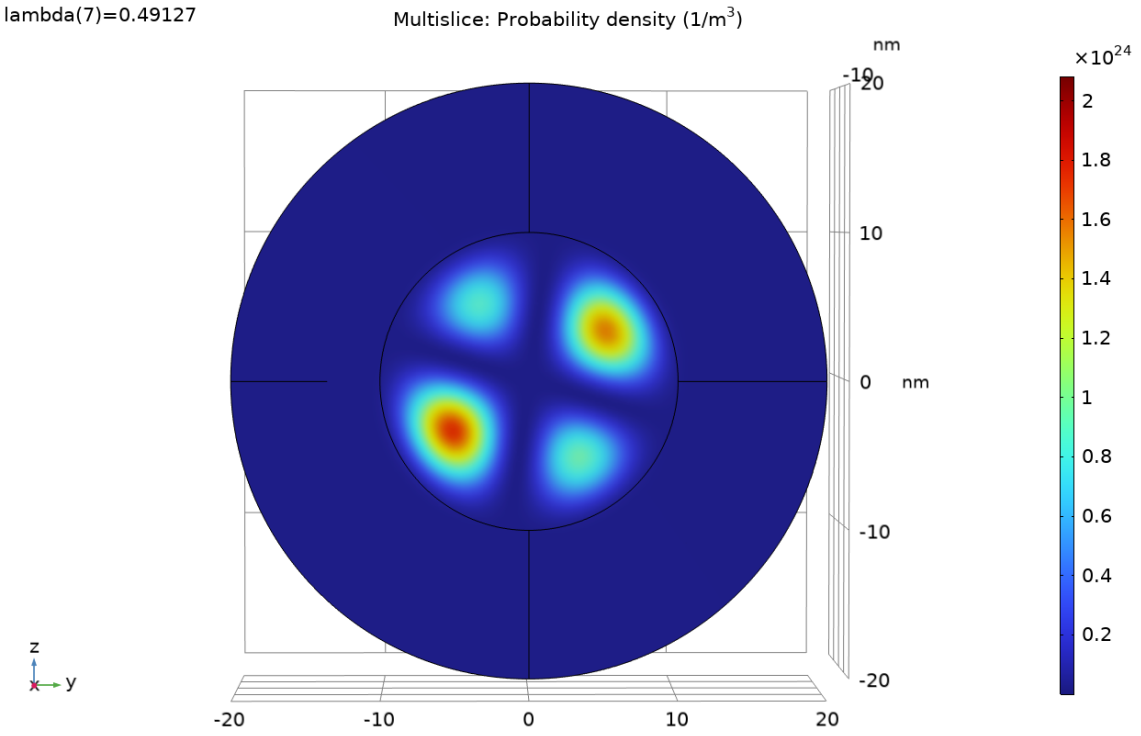
lambda(7)=0.49127
Multislice: Probability density (1/m3)
nm
-10
20
10
0
nm
-10
-20
-20
-10
0
10
20
z
y
×10^24
2
1.8
1.6
1.4
1.2
1
0.8
0.6
0.4
0.2

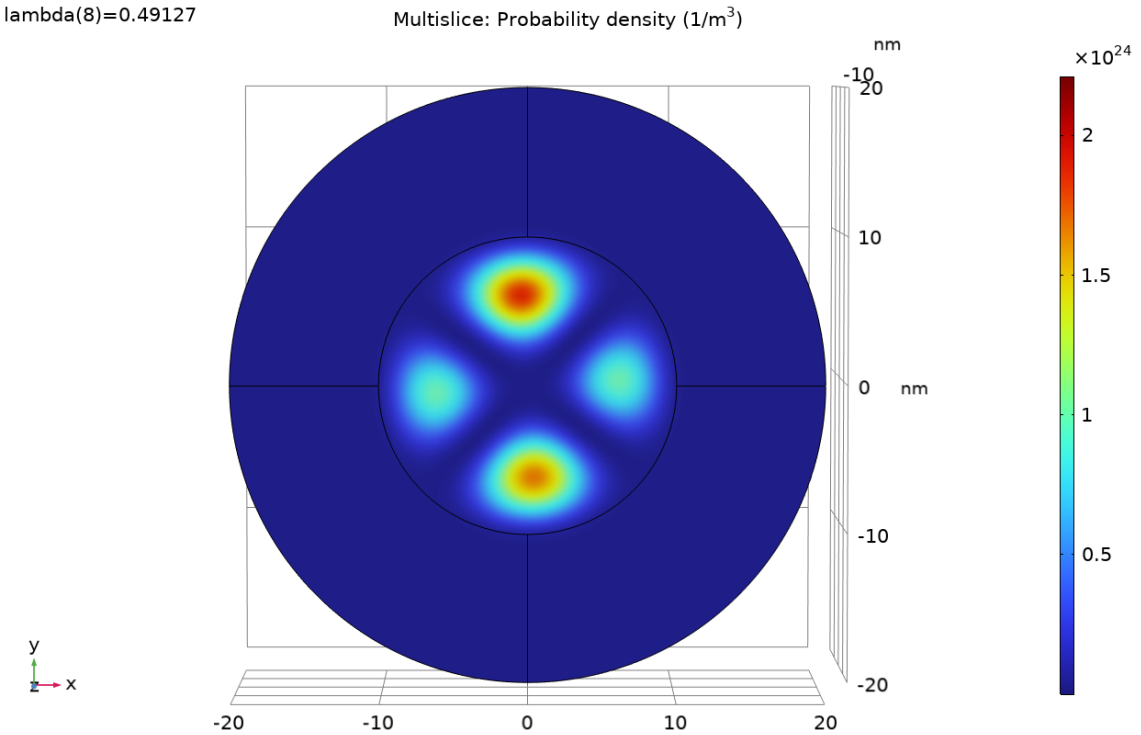
lambda(8)=0.49127
Multislice: Probability density (1/m3)
nm
-10
20
10
0
nm
-10
-20
-20
-10
0
10
20
y
x
×10^24
2
1.5
1
0.5

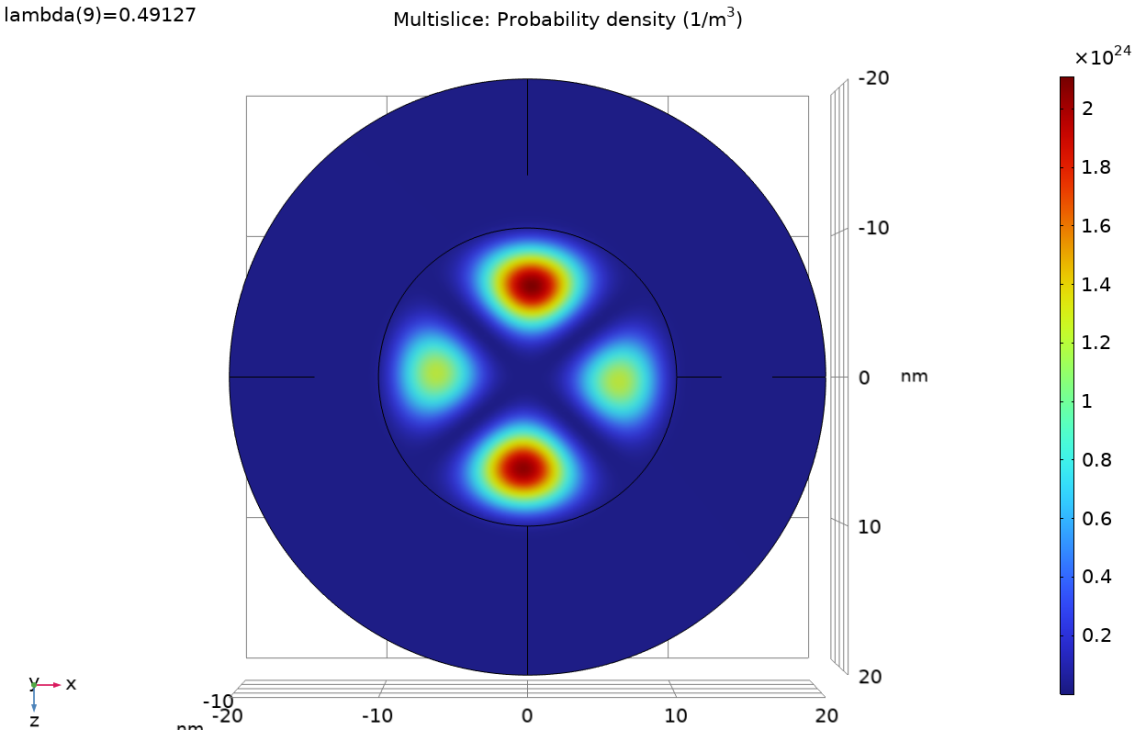
lambda(9)=0.49127
Multislice: Probability density (1/m^3)
×10^24
2
1.8
1.6
1.4
1.2
1
0.8
0.6
0.4
0.2
-20
-10
0
10
20
nm
y
x
z

$n = 2,\ l = 0$

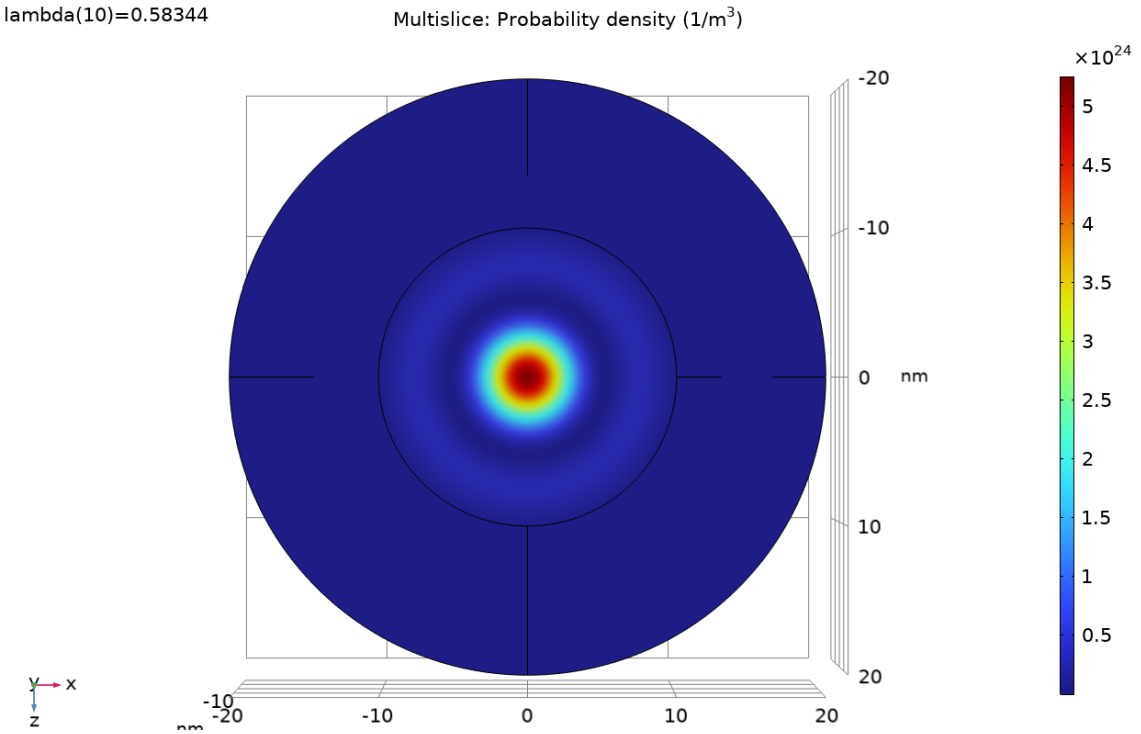
lambda(10)=0.58344
Multislice: Probability density (1/m3)
×10^24
5
4.5
4
3.5
3
2.5
2
1.5
1
0.5
-20
-10
0
10
20
nm
y
x
z

$n = 1,\ l = 3$

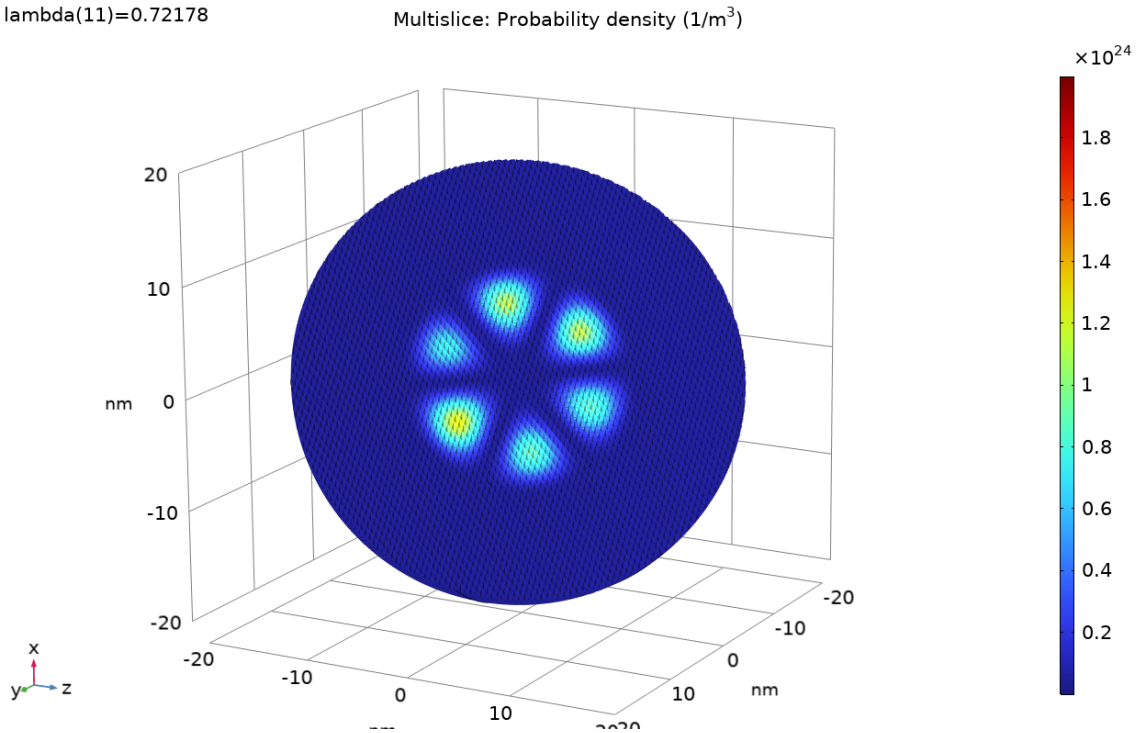
lambda(11)=0.72178
Multislice: Probability density (1/m^3)
×10^24
1.8
1.6
1.4
1.2
1
0.8
0.6
0.4
0.2
20
10
0
-10
-20
nm
x
y
z

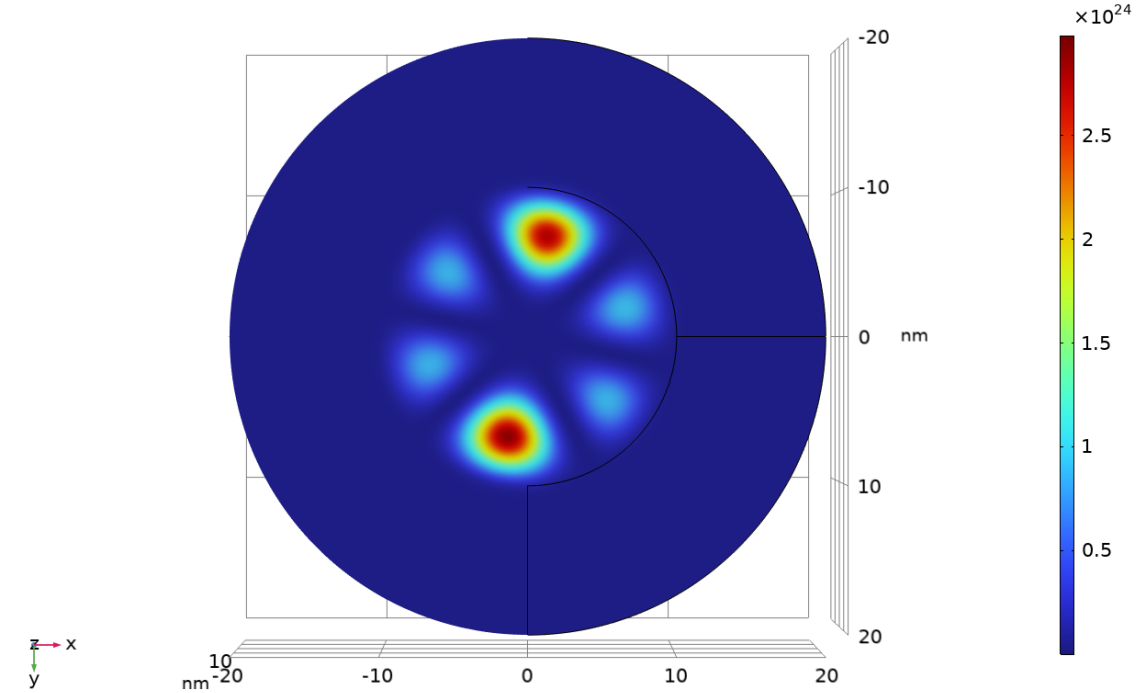
lambda(12)=0.72178
Multislice: Probability density (1/m^3)
×10^24
2.5
2
1.5
1
0.5
-20
-10
0
10
20
nm
z
x
y

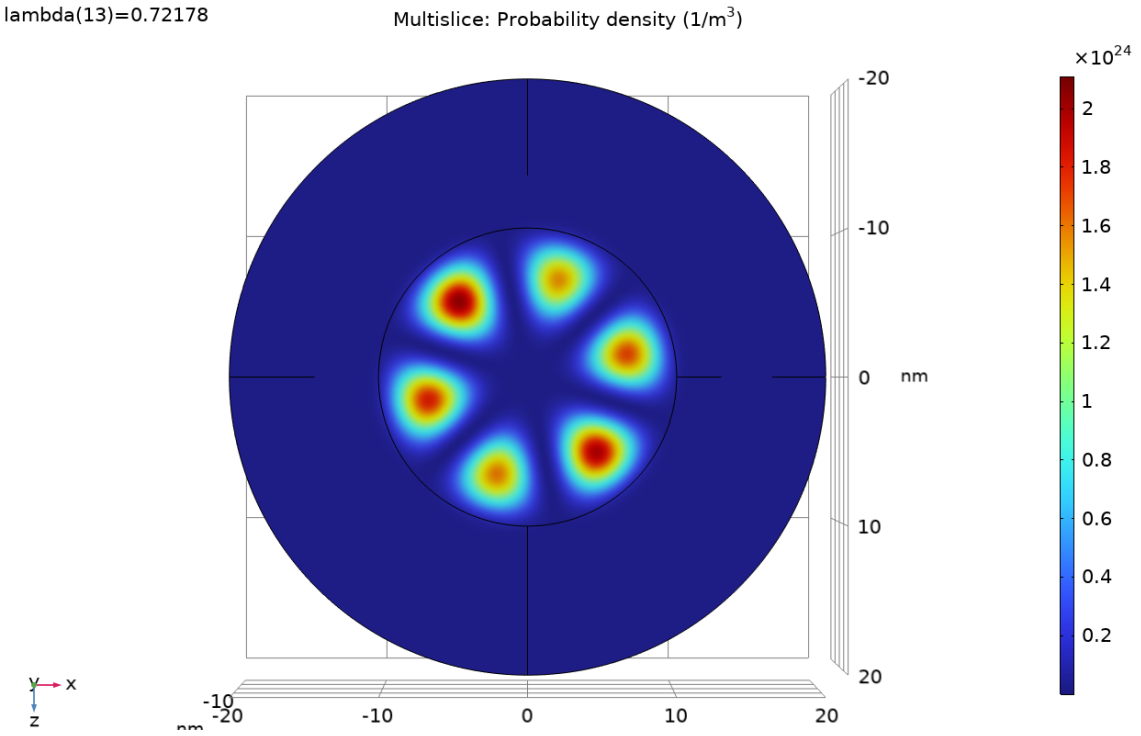
lambda(13)=0.72178
Multislice: Probability density (1/m3)
×10^24
2
1.8
1.6
1.4
1.2
1
0.8
0.6
0.4
0.2
-20
-10
0
10
20
nm
y
x
z

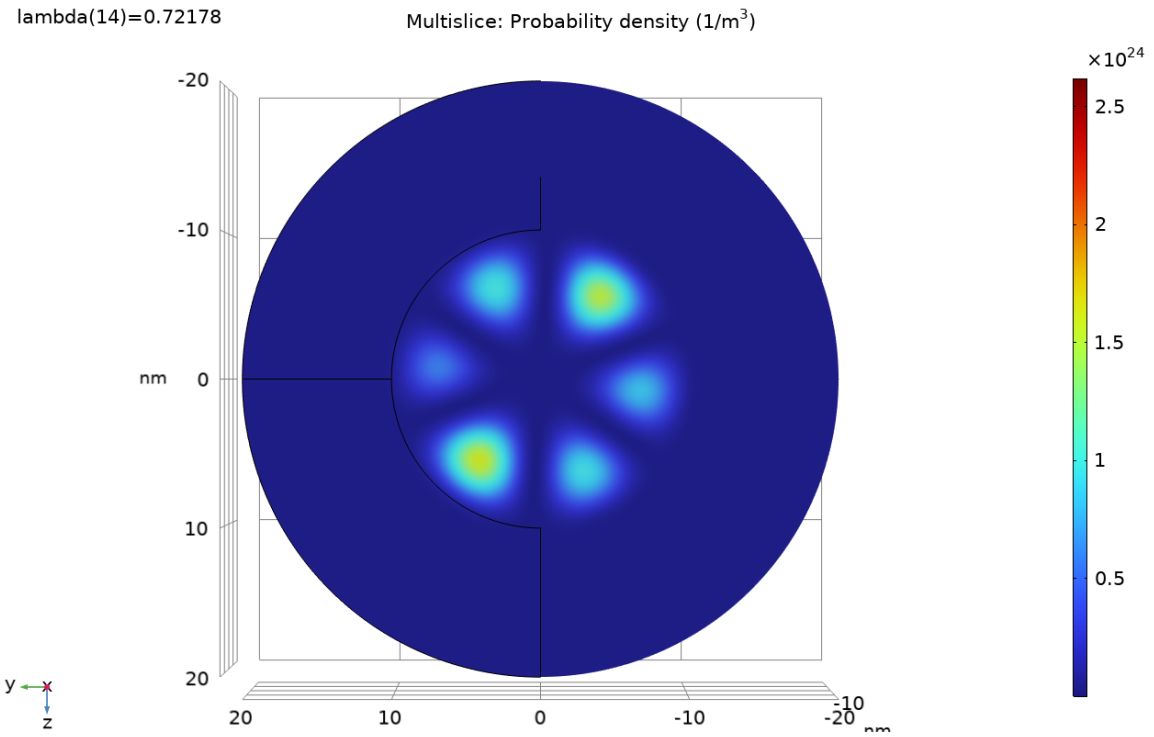
lambda(14)=0.72178
Multislice: Probability density (1/m3)
×10^24
2.5
2
1.5
1
0.5
-20
-10
0
10
20
nm
y
x
z

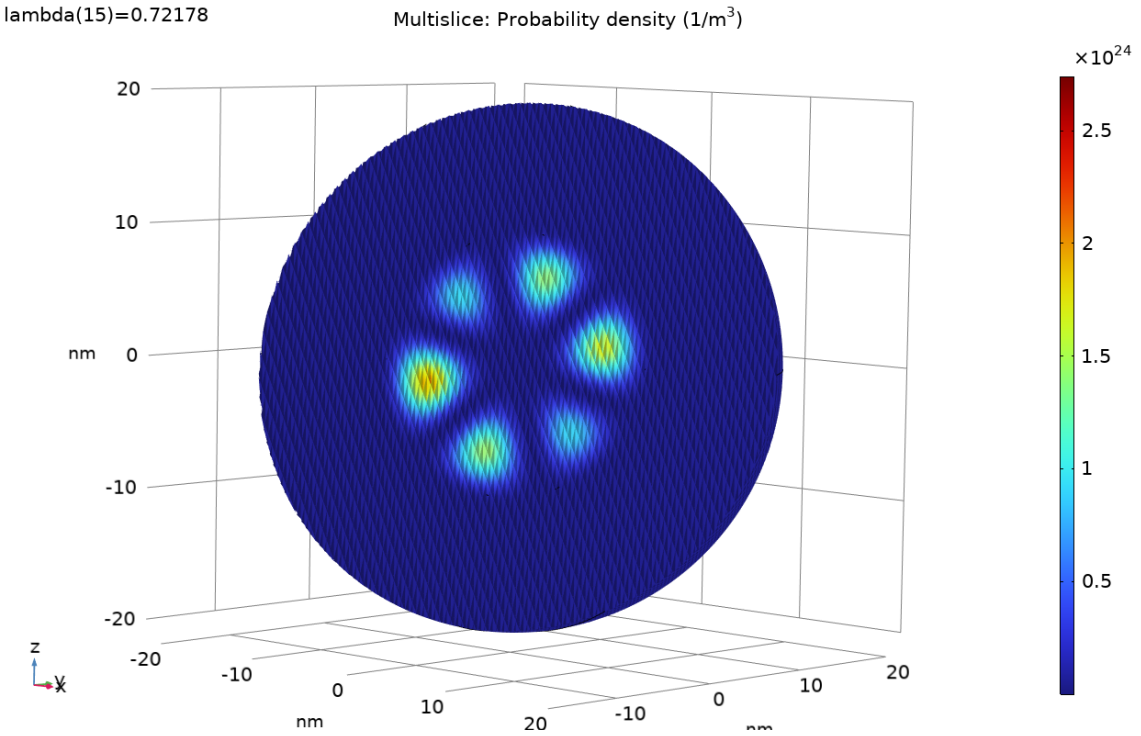
lambda(15)=0.72178
Multislice: Probability density (1/m3)
×10^24
2.5
2
1.5
1
0.5
20
10
0
-10
-20
nm
z
y
x

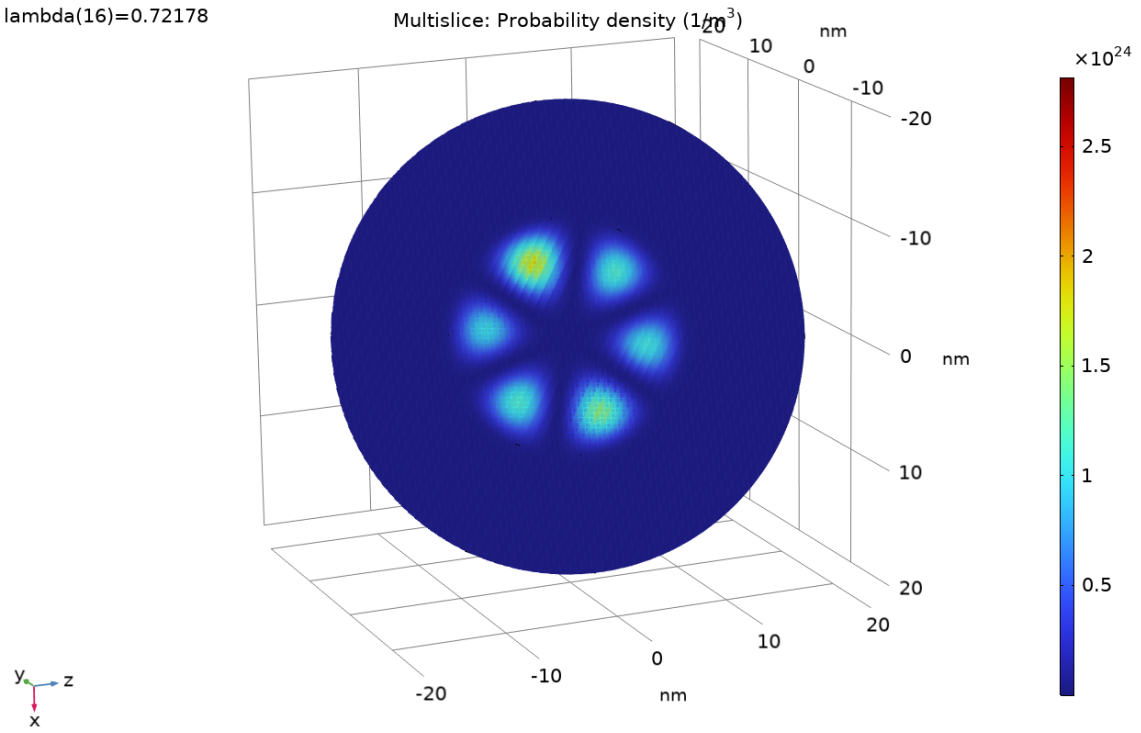
lambda(16)=0.72178
Multislice: Probability density (1/m3)
×10^24
2.5
2
1.5
1
0.5
20
10
0
-10
-20
nm
y
z
x

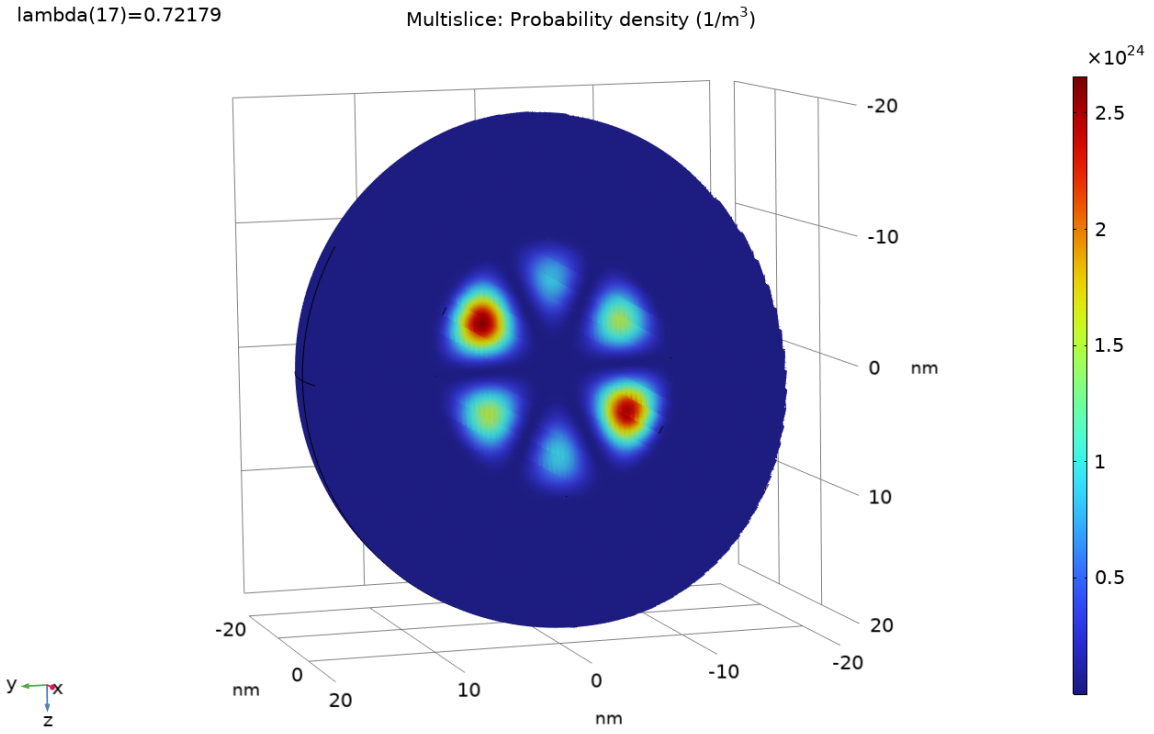
lambda(17)=0.72179
Multislice: Probability density (1/m^3)
×10^24
2.5
2
1.5
1
0.5
-20
-10
0
nm
10
20
-20
0
20
nm
10
0
nm
-10
-20
y
x
z

Appendix 4: Potential Energy (Middle QD Layer - 0.2 nm Slice)

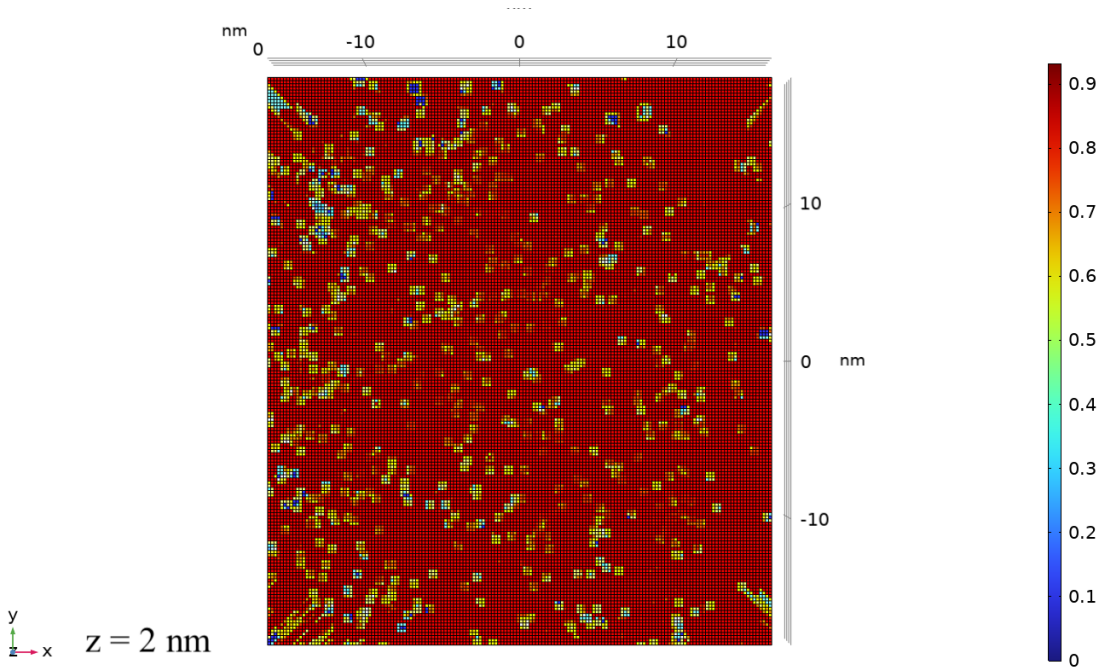

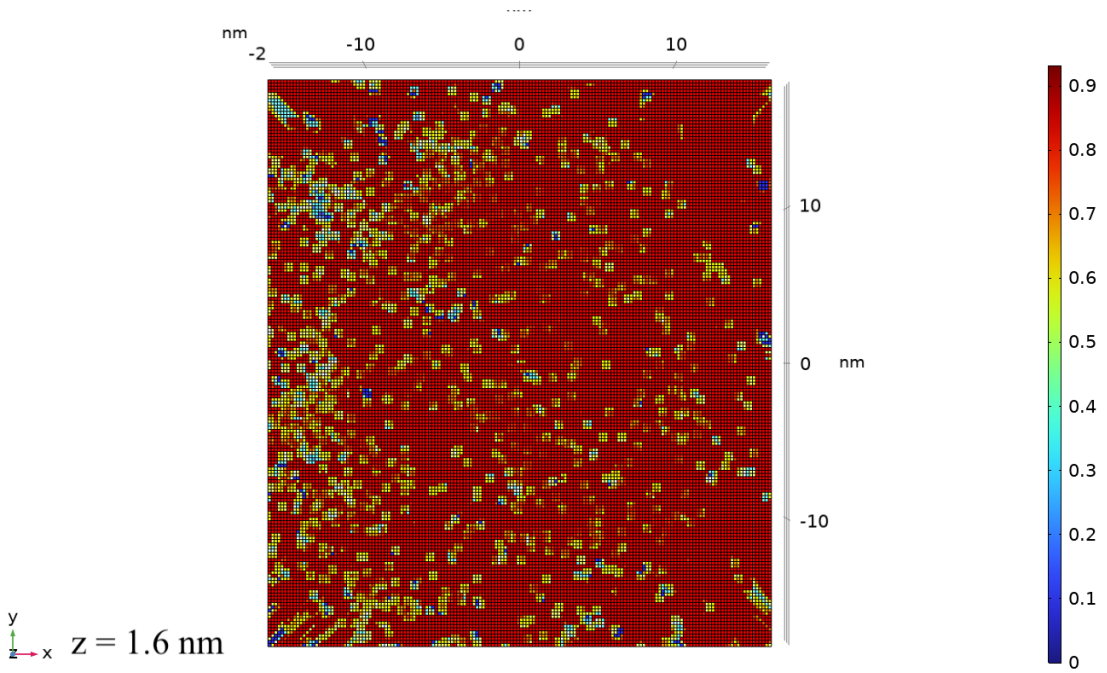

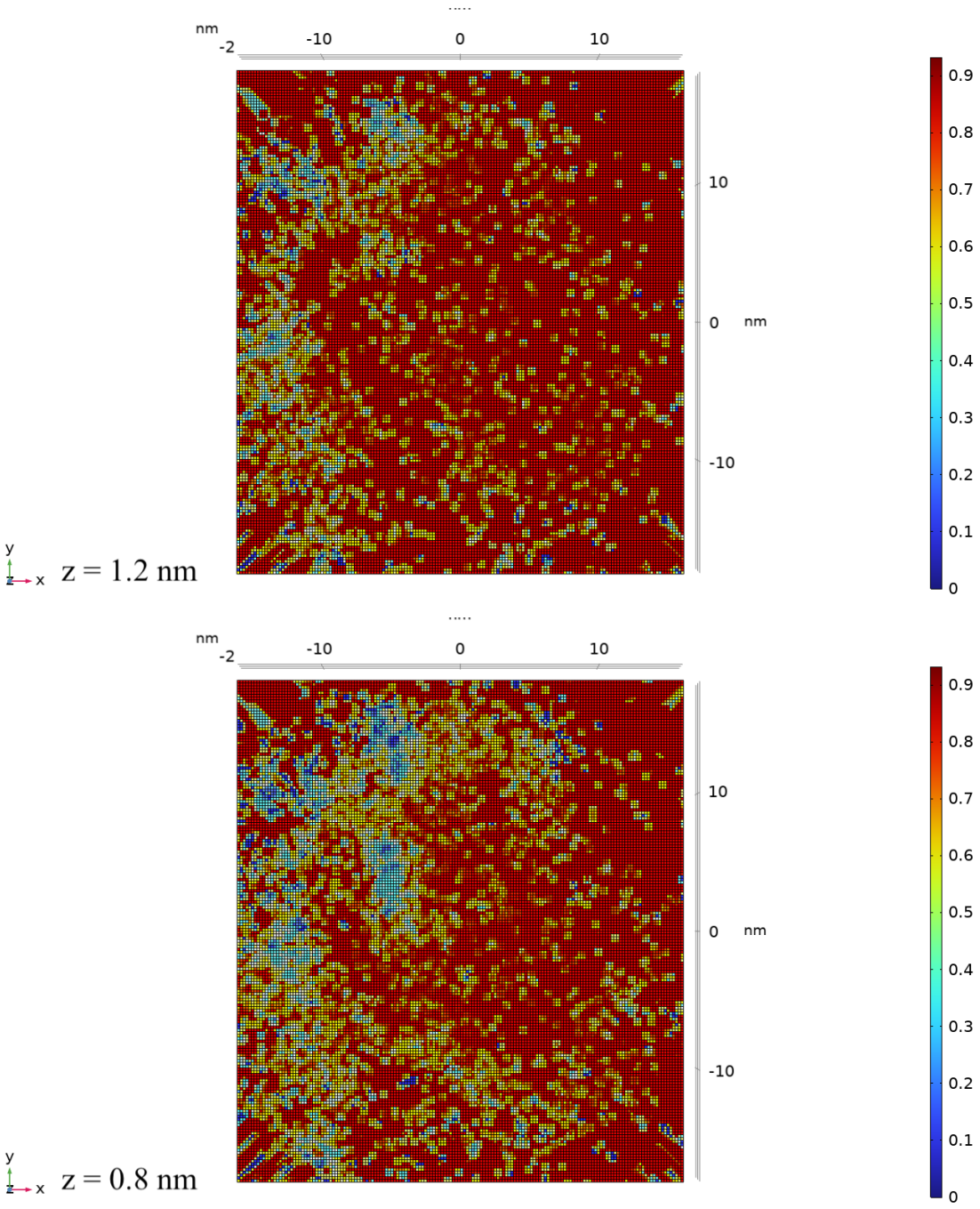
nm
-2
-10
0
10
10
0
nm
-10
0.9
0.8
0.7
0.6
0.5
0.4
0.3
0.2
0.1
0
y
x
z = 1.2 nm
nm
-2
-10
0
10
10
0
nm
-10
0.9
0.8
0.7
0.6
0.5
0.4
0.3
0.2
0.1
0
y
x
z = 0.8 nm

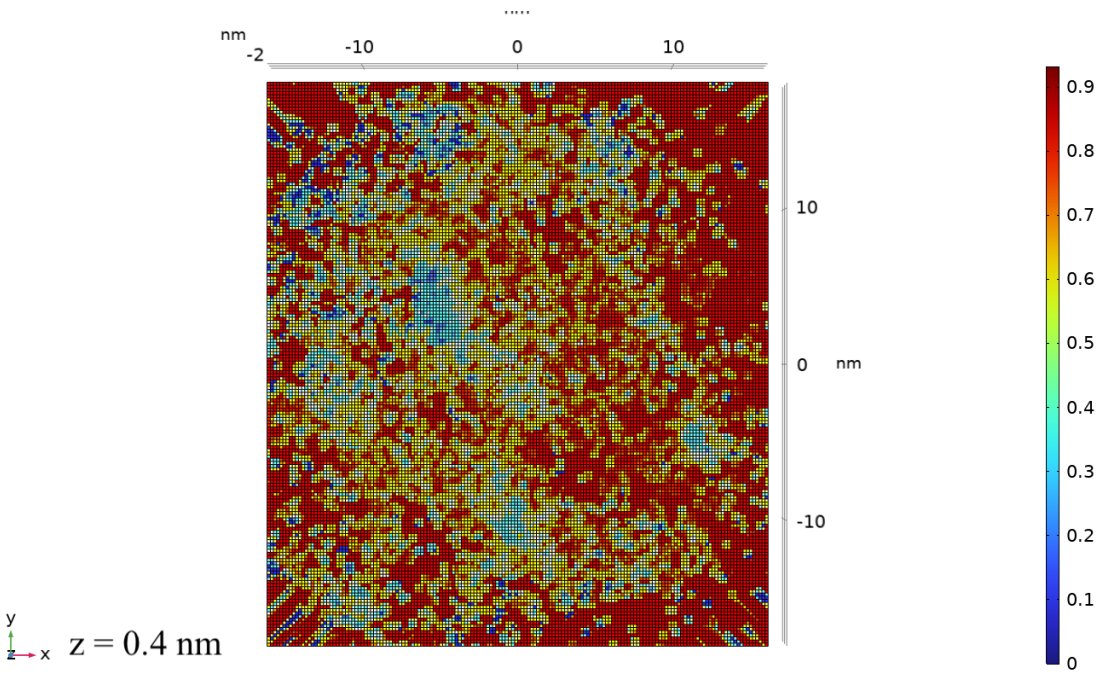
nm
-2
-10
0
10
10
0
nm
-10
0.9
0.8
0.7
0.6
0.5
0.4
0.3
0.2
0.1
0
y
z
x
z = 0.4 nm

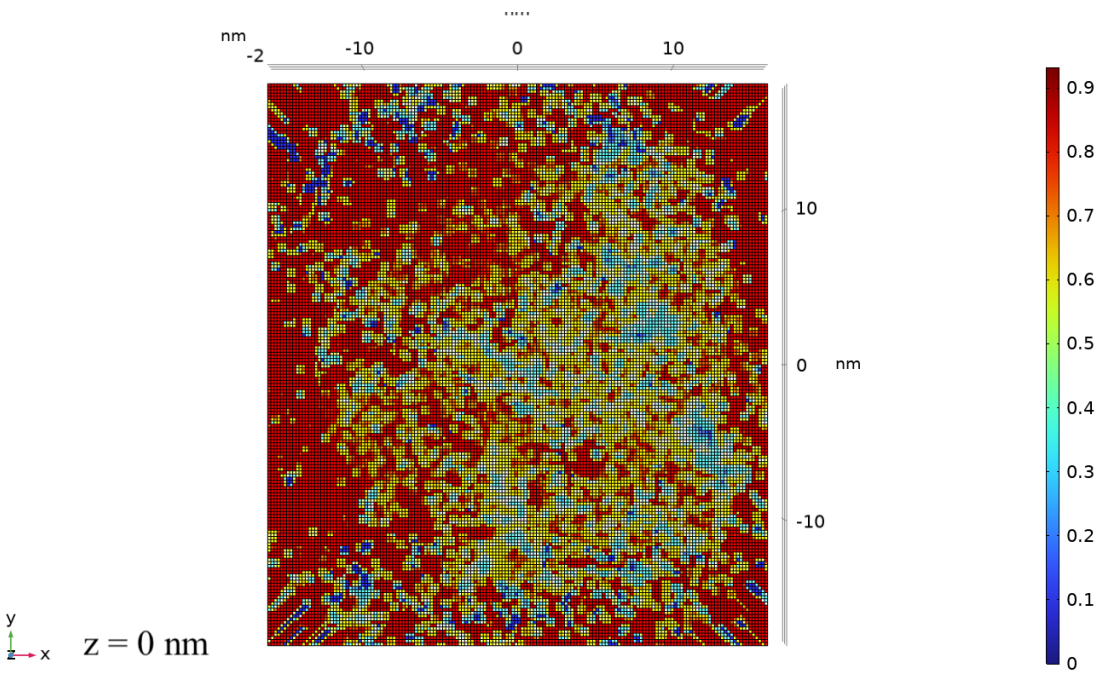
nm
-2
-10
0
10
10
0
nm
-10
0.9
0.8
0.7
0.6
0.5
0.4
0.3
0.2
0.1
0
y
z
x
z = 0 nm

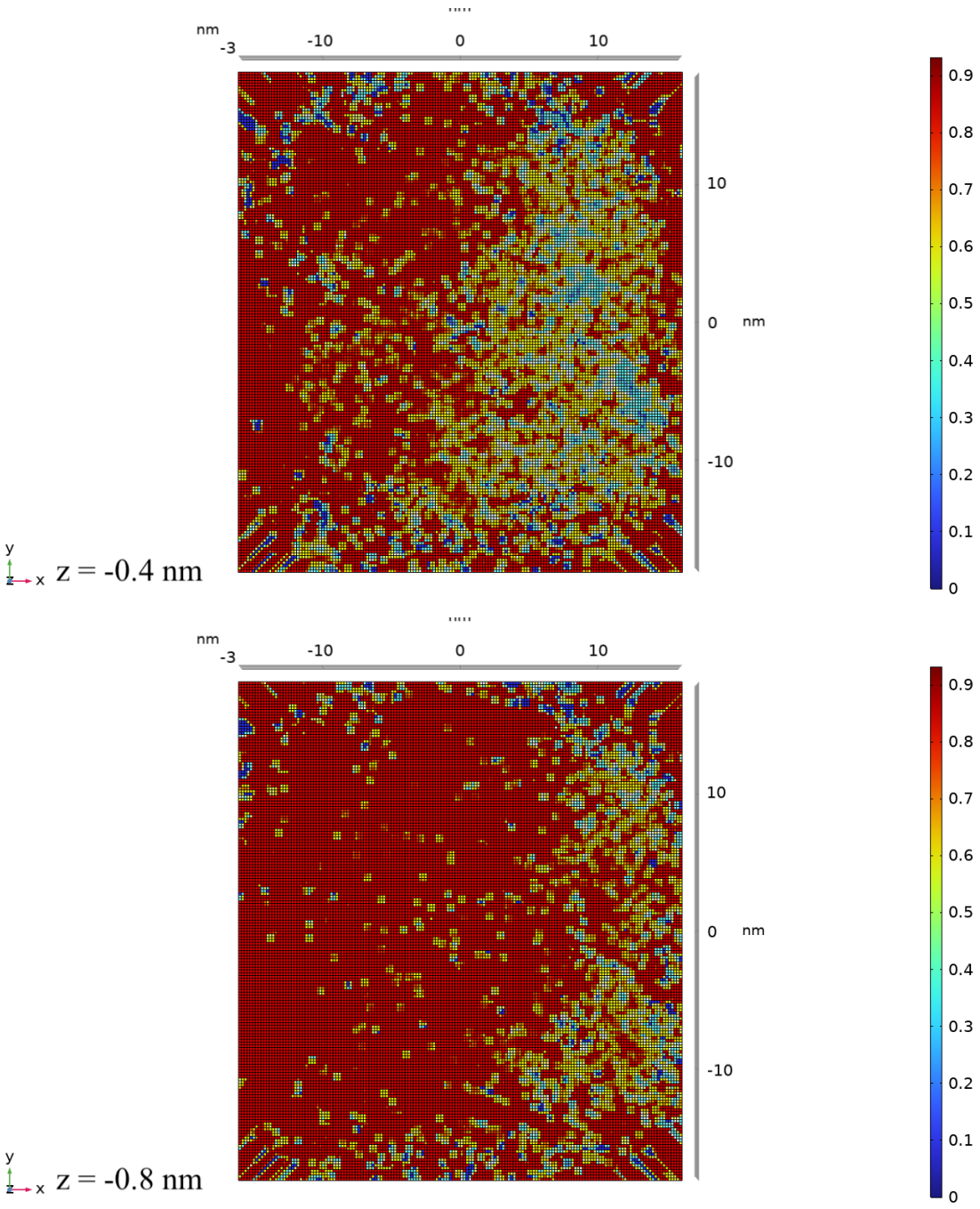
nm
-3
-10
0
10
10
0
nm
-10
0.9
0.8
0.7
0.6
0.5
0.4
0.3
0.2
0.1
0
y
x
z = -0.4 nm
nm
-3
-10
0
10
10
0
nm
-10
0.9
0.8
0.7
0.6
0.5
0.4
0.3
0.2
0.1
0
y
x
z = -0.8 nm

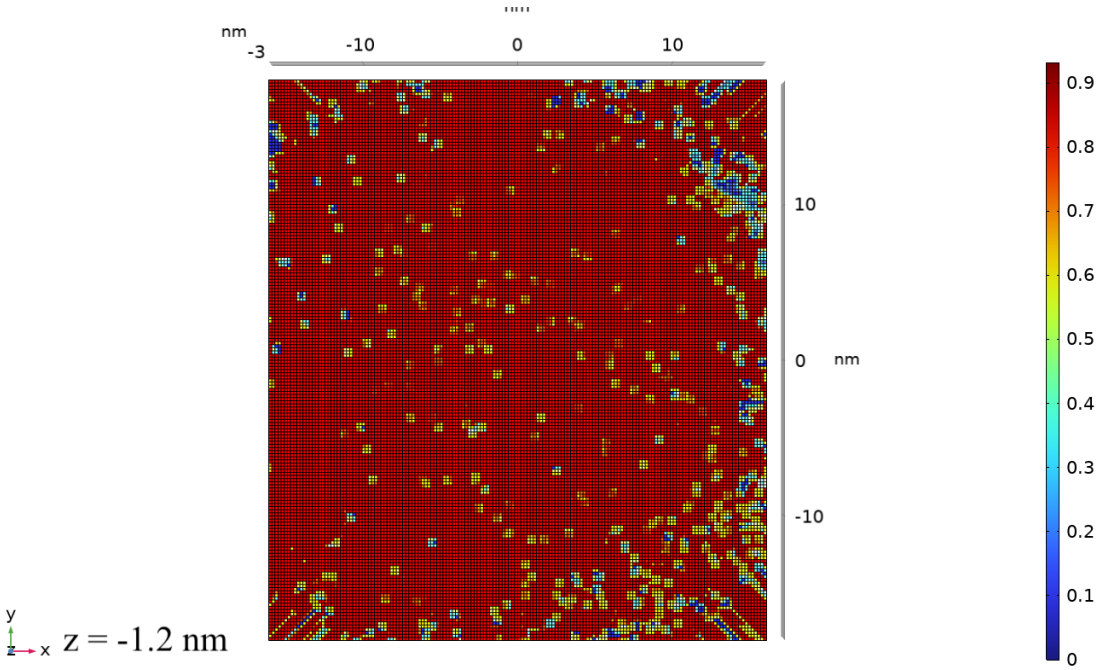
nm
-3
-10
0
10
10
0
nm
-10
0.9
0.8
0.7
0.6
0.5
0.4
0.3
0.2
0.1
0
y
x
z = -1.2 nm

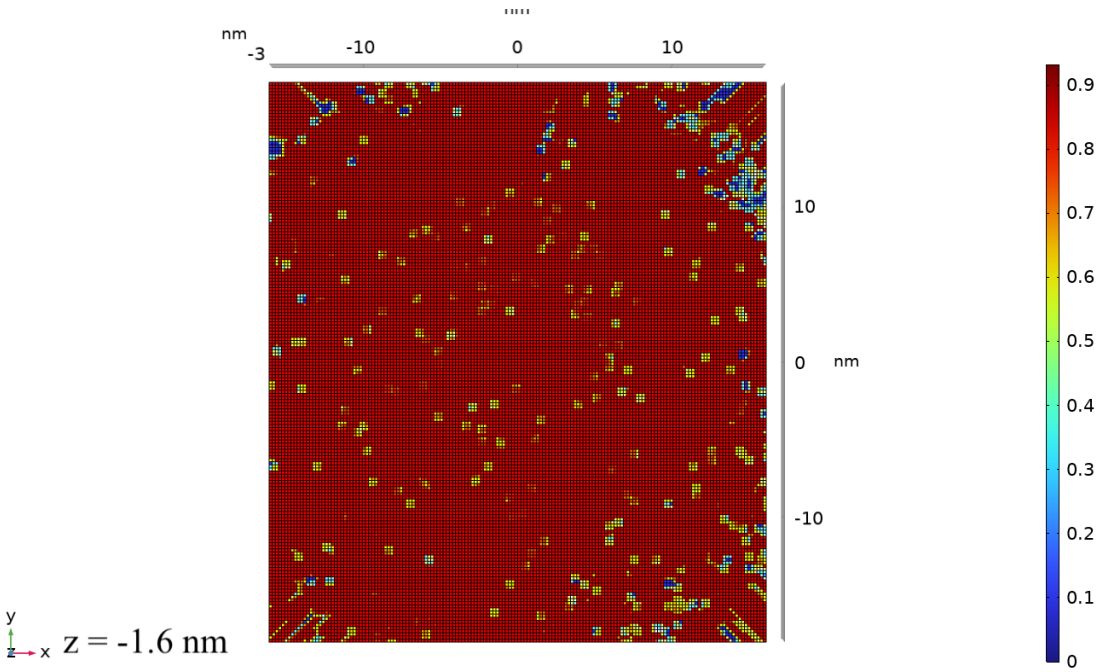
nm
-3
-10
0
10
10
0
nm
-10
0.9
0.8
0.7
0.6
0.5
0.4
0.3
0.2
0.1
0
y
x
z = -1.6 nm

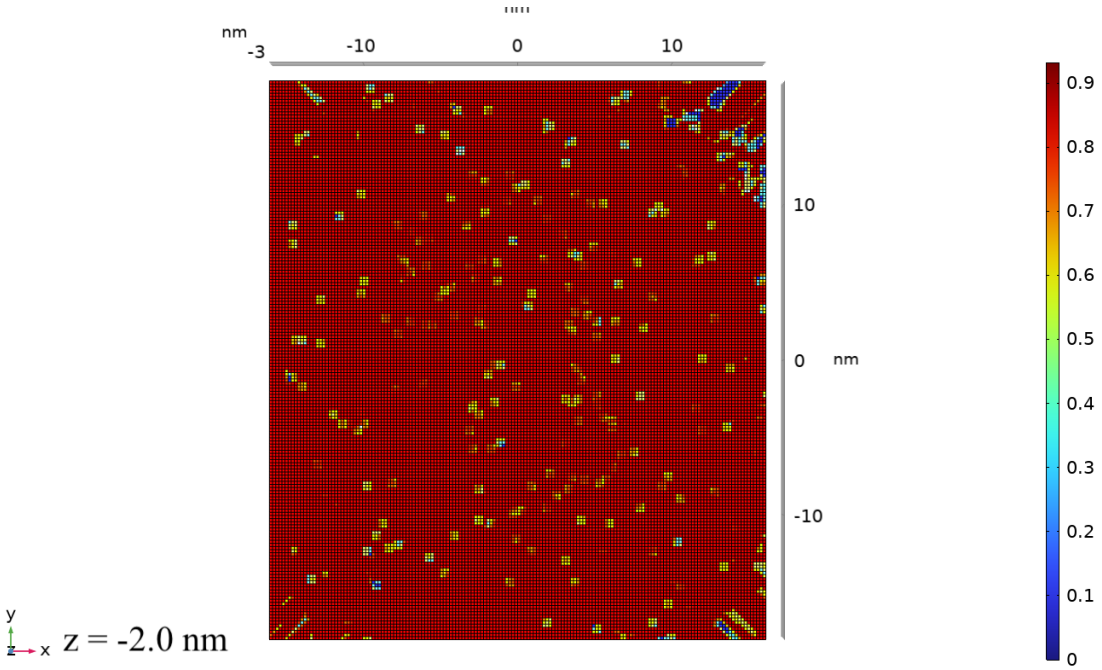
nm
-3
-10
0
10
10
0
nm
-10
0.9
0.8
0.7
0.6
0.5
0.4
0.3
0.2
0.1
0
y
x
z = -2.0 nm